INFORMATION TO USERS

The most advanced technology has been used to photograph and reproduce this manuscript from the microfilm master. UMI films the text directly from the original or copy submitted. Thus, some thesis and dissertation copies are in typewriter face, while others may be from any type of computer printer.

The quality of this reproduction is dependent upon the quality of the copy submitted. Broken or indistinct print, colored or poor quality illustrations and photographs, print bleedthrough, substandard margins, and improper alignment can adversely affect reproduction.

In the unlikely event that the author did not send UMI a complete manuscript and there are missing pages, these will be noted. Also, if unauthorized copyright material had to be removed, a note will indicate the deletion.

Oversize materials (e.g., maps, drawings, charts) are reproduced by sectioning the original, beginning at the upper left-hand corner and continuing from left to right in equal sections with small overlaps. Each original is also photographed in one exposure and is included in reduced form at the back of the book.

Photographs included in the original manuscript have been reproduced xerographically in this copy. Higher quality 6" x 9" black and white photographic prints are available for any photographs or illustrations appearing in this copy for an additional charge. Contact UMI directly to order.

UMI

University Microfilms International
A Bell & Howell Information Company
300 North Zeeb Road, Ann Arbor, MI 48106-1346 USA
313/761-4700 800/521-0600

Order Number 9118044

Normal mode decomposition of small-scale oceanic motions

Lien, Ren-Chieh, Ph.D.

University of Hawaii, 1990

U·M·I
300 N. Zeeb Rd.
Ann Arbor, MI 48106

NORMAL MODE DECOMPOSITION OF SMALL–SCALE OCEANIC MOTIONS

A DISSERTATION SUBMITTED TO THE GRADUATE DIVISION OF
THE UNIVERSITY OF HAWAII IN PARTIAL FULFILLMENT
OF THE REQUIREMENTS FOR THE DEGREE OF

DOCTOR OF PHILOSOPHY

IN OCEANOGRAPHY

December 1990

By

Ren–Chieh Lien

Dissertation Committee:

Peter Müller, Chairperson
Eric Firing
Roger B. Lukas
Dennis W. Moore
Bin Wang

Acknowledgements

I would like to express deep appreciation to all the members of my committee. In particular, I wish to thank Dr. Peter Müller for his excellent guidance and valuable advice in understanding the physics of oceanic motions and in the interpretation of oceanic measurements, and for his continued encouragement and support throughout the course of this work.

I would like to thank Dr. Roger Lukas for his help in data analysis and for providing valuable programs. Thanks also go to Dr. Eric Firing for stimulating discussions on the estimation of vertical displacement, to Dr. Dennis Moore and Dr. Bin Wang for valuable comments on the study of the geostrophic adjustment problem and monopole dynamics.

Furthermore, I wish to thank all my fellow graduate students for many stimulating discussions and ideas. Special thanks go to Niklas Schneider for all those daily chats and encouragement which provide the most stimulating research life. Constructive comments from Frank Bahr and Federico Graef–Ziehl in our Friday group meeting are appreciated. Also, I wish to thank Dr. Eric Kunze, Mark Prater and Eric Hirst (all at University of Washington, Seattle) for many constructive ideas. Finally, I would like to express my sincere gratitude to Crystal Miles , Nancy Koike, Diane Henderson, and Twyla Thomas for their helpful assistance.

Grateful thanks are also due to the Office of Naval Research, which supported the project under Contract N00014–87–K–0181.

Abstract

Small–scale oceanic motions are expected to contain both gravity waves and vortical motion. The vortical motion carries the perturbation potential vorticity of the system. Using eigenvectors of the linear equations of motion, the gravity mode and the vortical mode are defined. The vortical mode carries the linear perturbation potential vorticity and is horizontally nondivergent, whereas the gravity mode does not carry the linear perturbation potential vorticity. In an unforced, inviscid, linearized system, the gravity mode reduces to free linear gravity waves and the vortical mode to a steady geostrophic flow.

An attempt to separate oceanic measurements into the gravity and vortical modes can be conveniently made using fields of horizontal divergence HD, vortex stretching VS, and relative vorticity RV. Spectra of HD, VS, and RV are estimated using measurements of horizontal velocity and temperature from IWEX. Frequency spectral estimates of area–averaged horizontal divergence $\overline{HD}$ and relative vorticity $\overline{RV}$ represent the result of both attenuation and contamination horizontal wavenumber array response functions. The attenuation array response function describes the unresolvable nature of small–scale fluctuations of HD and RV, and the contamination array response function describes the contamination between HD and RV. These two potential problems inhibit the estimation of fluctuations of HD and RV separately.

Observed frequency spectra of $\overline{HD}$ are well represented by the GM–76 model (Cairns and Williams, 1976), whereas significant disagreements are found between spectral estimates of $\overline{RV}$ and the GM model at small horizontal scales. Frequency spectra of HD and RV of the GM model are very sensitive to the high wavenumber cutoff. Since the cutoff is not well determined to date, observed discrepancies do not conclusively imply the failure of linear internal wave theory.

strikingly well with the GM–76 spectrum model. This agreement suggests that fluctuations at vertical scales greater than 68 m (the smallest resolvable scale) are mainly the gravity mode component. Vertical wavenumber spectra of $\widehat{VS}$ and $\widehat{IR}$ also agree with previous observations by Gregg (1977) and by Gargett et al. (1981).

A general scheme to separate the relative vorticity and horizontal kinetic energy spectra into gravity and vortical modes is proposed. This requires horizontal wavenumber–frequency spectra of <u>uncontaminated</u> HD and RV which can be obtained by measuring horizontal velocity components along a closed contour, or with a horizontal space lag smaller than the scale of HD and RV.

Table of Contents

List of Tables

Table **Page**

List of Figures

Figure **Page**

Chapter 1

Introduction

Small–scale motions in the ocean are bounded by synoptic–scale quasigeostrophic eddies at large scales and by three–dimensional turbulence at small scales. Small–scale motions are often attributed to internal gravity waves whose typical horizontal scale ranges from hundreds of meters to tens of kilometers.

Most studies of small–scale oceanic motions have focused on internal gravity waves. However, it has been recognized that other processes also exist at small scales such as current finestructures, instabilities, and other motions. Their dynamics and kinematic structures are not well understood. Müller (1984) proposed that the current finestructure observed in measurements from Internal Wave Experiment (IWEX; Briscoe, 1975) is the small–scale vortical motion that is equivalent to the atmospheric mesoscale two–dimensional turbulence.

Conversely, observations of atmosphere mesoscale kinetic energy spectra have been interpreted as two–dimensional turbulence (Gage, 1979). However, it was proposed by VanZandt (1982) that mesoscale atmospheric motions can be explained by internal gravity waves as well. This was supported by the comparison between mesoscale spectra with a modified oceanic internal gravity wave model spectrum established by Garrett and Munk (1972). Apparently, the dynamics of atmosphere mesoscale motions are still not well understood.

In a linear system of incompressible, Boussinesq fluid on an f–plane in the ocean, both the free gravity wave and the steady geostrophic flow are supported. A major distinction between them is that the geostrophic flow carries the linear perturbation potential vorticity (the sum of the vertical component of relative vorticity and vortex stretching), whereas the linear gravity wave does not. Since the oceanic small–scale motion can be appropriately described by an incompressible, Boussinesq fluid on an f–plane, conceptually small–scale oceanic motions must be expected to contain two types of motions. The gravity wave propagates and does not carry perturbation potential vorticity, and the vortical motion is stagnant and carries the perturbation potential vorticity.

The existence of vortical motions at small scales can be recognized from the oceanic enstrophy cascade as well. One of the main sources of enstrophy in the ocean is the atmospheric input at large scales. The enstrophy can be dissipated at the turbulence scale only. If enstrophy cannot transfer directly from large scales to turbulence scales, vortical motions must exist at small scales and play the central role of the enstrophy cascade.

Evidence of the coexistence of internal gravity waves and vortical motions have been recently discovered in laboratory experiments, oceanic and atmospheric observations, and numerical model studies. Towing objects through a stratified fluid, Lin and Pao (1979) found that three–dimensional turbulence behind the object collapsed into two–dimensional pancake–vorticies and propagating internal gravity waves. The pancake–vortex carries the potential vorticity in the wake. McWilliams (1985) reviewed observations of submesoscale coherent vorticies (SCV) in the ocean. The vertical thickness of SCV found in the thermocline and subthermocline ranges from 500 m to 1 km. The horizontal scales of the SCV varies from 12 to 15 km, an order of magnitude smaller than that of energetic eddies in the ocean. In three–dimensional numerical studies of stratified turbulence, Riley et al. (1981), Staquet and Riley (1989a and 1989b) also found the coexistence of quasi–horizontal two–dimensional turbulence and internal gravity waves. In their attempt to understand the complete wavenumber–frequency structure, Müller et al. (1978) found coherence and energy disparities in IWEX measurements which can not be explained by internal gravity waves alone. Later, Müller (1984) proposed that observed disparities in IWEX measurements are attributable to the existence of small–scale vortical motions. Recently, an attempt to estimate the small–scale perturbation potential vorticity was made by Müller et al. (1988) using measurements from IWEX to understand the time and space scales of small–scale vortical motions.

Since observed fluctuations at small scales are expected to consist of both gravity waves and vorticies (the vortical motion), a clear distinction between them is required to understand small–scale motions better. Furthermore, the decomposition of fluctuations into gravity wave and vortical components is needed. Attempts to decompose vortical motions and gravity waves have been made by many researchers. To a limit of zero Froude number, Riley et al. (1981) and Lilly (1983) proposed to decompose the velocity field ($\underline{u}$) into vorticies and propagating waves as

$$\underline{u} = \nabla \times \psi \underline{e}_z + \nabla \phi + w \underline{e}_z \tag{1.1}$$

where ψ is the stream function corresponding to vortex motions, and the velocity potential ϕ and vertical velocity w are associated with the wave component. $\underline{e}_z$ is the unit vector in the upward direction. The wave component has no vertical component of relative vorticity and is horizontally divergent, whereas the vortex component has a nonvanishing vertical component of relative vorticity and is horizontally nondivergent.

However, the above approach breaks down for a finite Froude number as pointed out by Staquet and Riley (1989a). They suggested another generalized decomposition, based on the Ertel's potential vorticity, which decomposes the velocity field into the potential vorticity mode and the gravity wave mode in a nonrotating system. Two sets of diagnostic relations for three–dimensional velocity components of both modes were established as

$$\left.\begin{aligned} \frac{\underline{\nabla} \times \underline{u}^{(w)}}{\rho_0} \cdot \underline{\nabla}\rho = 0 \\ \underline{u}^{(w)} \cdot \underline{\nabla}\rho = \underline{u} \cdot \underline{\nabla}\rho \\ \underline{\nabla} \cdot \underline{u}^{(w)} = 0 \end{aligned}\right\} \tag{1.2}$$

$$\left.\begin{aligned} \frac{\underline{\nabla} \times \underline{u}^{(\pi)}}{\rho_0} \cdot \underline{\nabla}\rho = \pi \\ \underline{u}^{(\pi)} \cdot \underline{\nabla}\rho = 0 \\ \underline{\nabla} \cdot \underline{u}^{(\pi)} = 0 \end{aligned}\right\}, \tag{1.3}$$

where $\underline{u}^{(\pi)}$ and $\underline{u}^{(w)}$ are velocity fields of the potential vorticity mode and gravity wave mode components, and π the Ertel's potential vorticity in a nonrotating frame. The potential vorticity mode carries Ertel's potential vorticity and the gravity wave mode does not. The relative vorticity vector of the gravity wave field lies on the isopycnal surface. An intuitive assumption was made that the potential vorticity mode does not advect the isopycnal surface to prevent the generation of internal waves. Therefore, the velocity vector of the potential vorticity mode lies exactly on the isopycnal surface. The incompressibility condition was assumed for both modes. An application of the above approach was made in the numerical study by Staquet and Riley (1989b). The potential vorticity mode was found to be much more energetic in the later stage after the collapse of three–dimensional turbulence in a stratified fluid. The above scheme is able to decompose the velocity field, but not the density field. Therefore, the total energy of the system is not decomposed into the potential vorticity mode and gravity wave mode components. If one attempts to decompose the density field as well, using Staquet and Riley's approach, the potential vorticity will be contributed from both the gravity wave mode and the potential vorticity mode. This is an intrinsic obstacle in decomposing the vortical motion and gravity wave since their distinction is based on a nonlinear quantity – Ertel's potential vorticity.

A suitable decomposition scheme still remains to be developed. In this study, a decomposition scheme using the normal mode representation of small–scale motions proposed by Müller (1984) will be used. Two gravity modes and one vortical mode are defined using eigenvectors of the linearized small–scale motion. The linear eigenvector represents the polarization relation of each corresponding eigenmode. Accordingly, the vortical mode is characterized by carrying the linear perturbation potential vorticity and being horizontally nondivergent. The internal gravity mode does not carry linear perturbation potential vorticity and propagates. The advantage of the normal mode decomposition is that it diagonalizes the total energy and the linear perturbation potential vorticity into the gravity and vortical modes. Therefore, the total energy of eigenmode components can be determined. Note that the application of the normal mode representation has long been used in the study of oceanic motions such as that of Hasselmann (1970).

In a linear system, the normal mode decomposition can exactly separate two distinct motions that are identical to eigenmodes. Reviewing the familiar geostrophic adjustment problem, the competition of the gravity and vortical modes depending on the disturbance scale can be easily understood using the normal mode decomposition. However, the efficiency of the application to the nonlinear system depends on the nonlinearity of the system. Applying the normal mode decomposition to a monopole, which is a pure nonlinear vortical motion, results in the total energy ratio of the gravity and vortical modes depending on the Rossby and Burger numbers. For small Rossby and Burger numbers, the gravity mode is much weaker than the vortical mode.

Using the normal mode decomposition to separate the gravity and vortical modes requires substantial wavenumber information of velocity and vertical displacement fields. The analysis can be made conveniently using fields of horizontal divergence (HD), relative vorticity (RV), and vortex stretching (VS). Since the vortical mode is horizontally nondivergent, fluctuations of HD are completely due to the gravity mode. Accordingly, RV of the gravity mode can be obtained using the polarization relation of the gravity mode. Its vortical mode component can be obtained as the residual of the total relative vorticity from the gravity mode component. The horizontal kinetic energy spectrum can also be separated into the gravity and vortical modes using horizontal wavenumber–frequency spectra of HD and RV.

Spectra of HD, RV, and VS are estimated using measurements of horizontal velocity and temperature from IWEX. Unfortunately, frequency spectral estimates of HD and RV are subjected to scale resolution and contamination problems. Detailed discussion of these problems are represented by lowpass attenuation and bandpass contamination array response functions. The lowpass array response function is due to the finite separation between current sensors, whereas the bandpass array response function originates from the discrete sampling of velocity measurements in the space. Frequency spectral estimates of HD are well represented by the GM spectrum at all depths. Frequency spectral estimates of RV also agree with the GM spectrum except at the shallowest depth where small–scale fluctuations are resolved. Due to the scale resolution and contamination problems of spectral estimates of HD and RV, the normal mode decomposition cannot be carried out. Frequency spectral estimates of

VS and IR (inverse Richardson number) are obtained and they are well represented by the GM model.

The linear eigenmode representation will be described in the next chapter. The detailed algebra and two illustrative applications of the linear eigenmode representation will be discussed. Data analysis of IWEX will be discussed in chapter 3. Spectral analysis of HD, RV, VS, and IR will be discussed in detail. Also, the normal mode decomposition of the relative vorticity and the horizontal kinetic energy spectra is discussed, although it cannot be made using IWEX measurements. In the final chapter, summaries of this study will be presented together with proposed future works.

Chapter 2

Linear Eigenmode Representation of Small–Scale Oceanic Motions

Small–scale motions can be appropriately described by the dynamic system of an incompressible, Boussinesq fluid on an f–plane. This system contains gravity waves and geostrophic flows. Traditionally, the gravity wave motion is described by a second order differential equation of vertical velocity. The geostrophic flow is described by the potential vorticity conservation equation. Neither the vertical velocity equation nor the potential vorticity equation alone can determine the small-scale motion completely.

In this chapter, a linear eigenmode representation of small–scale motions will be discussed. Two gravity modes and one vortical mode are defined using eigenvectors of the linear system. Eigenmodes have distinctive kinematic structures and dynamics described by corresponding eigenvectors and eigenvalues. Since three eigenvectors form a complete basis, small-scale motions must be expected to contain both gravity and vortical modes. To the limit of the linear system, the gravity mode is the linear internal gravity wave and the vortical mode is the familiar steady geostrophic flow.

The linear eigenmode representation will be discussed in the next section. Its application to a linear system and a nonlinear system will be illustrated. First, the eigenmode representation will be applied on a geostrophic adjustment problem. Disturbances of the flow field or surface displacement in the system are decomposed into gravity and vortical components. The gravity mode propagates and carries energy away, whereas the vortical mode does not propagate. The second example is a prototype nonlinear vortical motion described by the monopole dynamics. The monopole is linearly decomposed into the gravity and vortical components. The energy ratio of these two modes depends on the Rossby number and the Burger number. The gravity mode component is negligibly small compared with the vortical mode at small Rossby and Burger numbers.

2.1 Small–Scale Oceanic Motions

Small–scale oceanic motions can be appropriately described by the system of incompressible, Boussinesq fluid on an f–plane. A linearly–stratified, unbounded ocean will be considered. The dynamic equations of small–scale oceanic motions are given as:

$$\left.\begin{array}{rcl} \partial_t u - fv + \dfrac{1}{\rho_0}\partial_x p & = & S_1 \\ \partial_t v + fu + \dfrac{1}{\rho_0}\partial_y p & = & S_2 \\ \partial_t w + N^2\eta + \dfrac{1}{\rho_0}\partial_z p & = & S_3 \\ \partial_t \eta - w & = & S_4 \\ \partial_x u + \partial_y v + \partial_z w & = & 0 \end{array}\right\} . \tag{2.1}$$

Here, u, v, and w are east, north, and upward velocity components, p the perturbation pressure, ρ_0 the Boussinesq density, f the Coriolis parameter, and N the Brunt–Väisälä frequency. A linear relation between the vertical displacement η and the perturbation density ρ has been assumed as $\rho = \frac{\rho_0}{g} N^2 \eta$. Nonlinear interactions, dissipation, diffusion, and external forcing are implicitly embedded in source terms S_1, S_2, S_3, and S_4.

A Fourier expansion of the field variable $\Phi(\underline{x}, t)$ into its wavenumber space can be expressed as

$$\Phi(\underline{x}, t) = \int\int\int_{-\infty}^{\infty} d^3\underline{k}\, \widehat{\Phi}(\underline{k}, t) e^{-i\underline{k}\cdot\underline{x}}. \tag{2.2}$$

Here Φ represents any field variable of u, v, w, p, and η . The wavenumber vector and the position vector are $\underline{k} = (k_x, k_y, k_z)$ and $\underline{x} = (x, y, z)$, respectively. The Fourier coefficient $\widehat{\Phi}(\underline{k}, t)$ is defined by the Fourier transformation

$$\widehat{\Phi}(\underline{k}, t) = \frac{1}{(2\pi)^3} \int\int\int_{-\infty}^{\infty} d^3\underline{x}\, \Phi(\underline{x}, t) e^{i\underline{k}\cdot\underline{x}}. \tag{2.3}$$

At any give wavenumber vector, the dynamics of small-scale motions is described as

$$\left.\begin{aligned}
\partial_t \widehat{u} - f\widehat{v} - \frac{ik_x}{\rho_0}\widehat{p} &= \widehat{S}_1 \\
\partial_t \widehat{v} + f\widehat{u} - \frac{ik_y}{\rho_0}\widehat{p} &= \widehat{S}_2 \\
\partial_t \widehat{w} + N^2\widehat{\eta} - \frac{ik_z}{\rho_0}\widehat{p} &= \widehat{S}_3 \\
\partial_t \widehat{\eta} - \widehat{w} &= \widehat{S}_4 \\
k_x\widehat{u} + k_y\widehat{v} + k_z\widehat{w} &= 0
\end{aligned}\right\} \tag{2.4}$$

where the overhat ^ denotes corresponding Fourier coefficients.

There are three prognostic variables and two diagnostic variables in the system. Traditionally, $\widehat{u}$, $\widehat{v}$, and $\widehat{\eta}$ are chosen as prognostic variables. Diagnostic variables $\widehat{w}$ and $\widehat{p}$ can be obtained from the continuity equation and the divergence of momentum equations, i.e.,

$$\widehat{w} = \frac{1}{k_z} \{-k_x \widehat{u} - k_y \widehat{v}\} \tag{2.5}$$

$$\widehat{p} = \frac{i\rho_0}{K^2} \left\{ f(k_x \widehat{v} - k_y \widehat{u}) - N^2 k_z \widehat{\eta} + k_x \widehat{S}_1 + k_y \widehat{S}_2 + k_z \widehat{S}_3 \right\}. \tag{2.6}$$

Diagnostic variables are not dynamically important since they can be obtained at each instant in time through their diagnostic relations with prognostic variables. In fact, the dynamics of the system is entirely determined by three prognostic variables which form the state vector of the system.

The choice of a set of prognostic variables of the system depends on the specific purpose. In principle, three independent prognostic variables are required to completely describe the state of the small-scale system. For an experimentalist, appropriate prognostic variables could be u, v, and η since they can be measured directly. For a data analyst, the most suitable prognostic variables might be two rotary velocity components and η since internal waves have distinct characteristics which can be clearly described by rotary velocity spectra. For a theoretician, HD, RV, and VS are convenient prognostic variables to use. Details of the eigenmode representation of small-scale motions using various forms of the state vector will be discussed separately.

First, (u, v, η) is chosen as the state vector. The dynamic equations of small-scale motions can be expressed in a compact form as

$$\partial_t\, \underline{\widehat{\Phi}}(\underline{k},t) \;+\; \mathbf{M}(\underline{k})\, \underline{\widehat{\Phi}}(\underline{k},t) = \underline{Q}(\underline{k},t) \tag{2.7}$$

$$\underline{\widehat{\Phi}} = \begin{pmatrix} \widehat{u} \\ \widehat{v} \\ \widehat{\eta} \end{pmatrix} \tag{2.8}$$

$$\mathbf{M}(\underline{k}) = -\frac{f}{K^2} \begin{pmatrix} k_x k_y & (k_y^2 + k_z^2) & \frac{N^2}{f} k_x k_z \\ -(k_x^2 + k_z^2) & -k_x k_y & \frac{N^2}{f} k_y k_z \\ -\frac{k_x K^2}{f k_z} & -\frac{k_y K^2}{f k_z} & 0 \end{pmatrix} \tag{2.9}$$

$$\underline{Q}(\underline{k},t) = \frac{1}{K^2} \begin{pmatrix} (k_y^2 + k_z^2)\widehat{S}_1 - k_x k_y \widehat{S}_2 - k_x k_z \widehat{S}_3 \\ -k_x k_y \widehat{S}_1 + (k_x^2 + k_z^2)\widehat{S}_2 - k_y k_z \widehat{S}_3 \\ K^2 \widehat{S}_4 \end{pmatrix}, \tag{2.10}$$

where K is the magnitude of the wavenumber vector. The source vector $\underline{Q}$ is important for studying responses of the system to atmospheric forcings, diffusion, dissipation, etc . The state matrix **M** determines the kinematic structure and dynamics of the system. Since the state matrix is not in a diagonal form, the three prognostic variables are coupled dynamically.

Using eigenvectors of the linearized system as the new basis, prognostic variables can be projected into eigenmode amplitudes. Dynamic evolutions of eigenmode amplitudes are decoupled in a linear, unforced, and inviscid system. The kinematic structures as well as the dynamics of eigenmodes are clearly determined.

Three eigenvalues $\sigma^s(\underline{k})$ and corresponding eigenvectors $\underline{\widehat{\phi}}^s(\underline{k})$ satisfying $\mathrm{M}(\underline{k})\,\underline{\widehat{\phi}}^s(\underline{k}) = -i\sigma^s(\underline{k})\,\underline{\widehat{\phi}}^s(\underline{k})$ are obtained as

$$\sigma^s(\underline{k}) = s\sqrt{\frac{N^2\alpha^2 + f^2k_z^2}{K^2}} = s\sigma(\underline{k}), \qquad s = 0,\ +,- \tag{2.11}$$

$$\underline{\widehat{\phi}}^0(\underline{k}) = \frac{iN}{\sigma K}\begin{pmatrix} k_y \\ -k_x \\ \frac{f}{N^2}k_z \end{pmatrix} \tag{2.12}$$

$$\underline{\widehat{\phi}}^{\pm}(\underline{k}) = \frac{k_z}{\sqrt{2}\sigma\alpha K}\begin{pmatrix} \mp\sigma k_x + ifk_y \\ \mp\sigma k_y - ifk_x \\ -i\frac{\alpha^2}{k_z} \end{pmatrix}. \tag{2.13}$$

Here α is the magnitude of the horizontal wavenumber vector. Using eigenvectors as the new basis, the state vector is decomposed into three eigenmode components of each wavenumber at any time instant, i.e.,

$$\underline{\widehat{\Phi}}(\underline{k},t) = \sum_{s=0,\pm} \widehat{a}^s(\underline{k},t)\underline{\widehat{\phi}}^s(\underline{k}), \tag{2.14}$$

where $\widehat{a}^s$ is the amplitude of the eigenmode s. Similarly, eigenmode amplitudes can be expressed in terms of the state vector as

$$\widehat{a}^s(\underline{k}, t) = \sum_i \widehat{\Phi}_i(\underline{k}, t)\ \widehat{\phi}_i^{s\dagger}(\underline{k}), \tag{2.15}$$

where the adjoint eigenvector $\underline{\widehat{\phi}}^{s\dagger}(\underline{k})$ is given by

$$\underline{\widehat{\phi}}^{0\dagger}(\underline{k}) = \frac{iN}{\sigma K} \begin{pmatrix} -k_y \\ k_x \\ -fk_z \end{pmatrix} \tag{2.16}$$

$$\underline{\widehat{\phi}}^{\pm\dagger}(\underline{k}) = \frac{k_z}{\sqrt{2}\sigma\alpha K} \begin{pmatrix} \mp\sigma k_x \dfrac{K^2}{k_z^2} - ifk_y \\ \mp\sigma k_y \dfrac{K^2}{k_z^2} + ifk_x \\ i\dfrac{N^2}{k_z}\alpha^2 \end{pmatrix}. \tag{2.17}$$

The completeness and orthogonality conditions between eigenvectors and their adjoints are justified since

$$\sum_i \widehat{\phi}_i^s \widehat{\phi}_i^{s'\dagger} = \delta_{ss'} \tag{2.18}$$

$$\sum_s \widehat{\phi}_i^s \widehat{\phi}_j^{s\dagger} = \delta_{ij}. \tag{2.19}$$

Therefore, eigenvectors form a complete basis. It is worthwhile mentioning that using the linear eigenmode representation the total energy (including both kinetic and potential energy) is diagonalized into three eigenmode components at each instant in time, i.e.,

$$\frac{1}{2}\langle \hat{u}\hat{u}^* + \hat{v}\hat{v}^* + \hat{w}\hat{w}^* + N^2\hat{\eta}\hat{\eta}^* \rangle = \frac{1}{2}\sum_{s=0,\pm}\langle \hat{a}^s\hat{a}^{s*} \rangle. \tag{2.20}$$

Here, the angle brackets denote the ensemble average and the asterisk the complex conjugate.

Eigenvectors describe relative amplitudes and phases among state variables of eigenmodes. They are also termed the polarization relations. The kinematic structures of eigenmodes are determined through polarization relations. Note that although polarization relations change with various forms of state vectors, eigenvalues will remain the same since they depend on the the underlying dynamics only.

The most distinctive feature between eigenmodes of small-scale motions is revealed by the linear perturbation potential vorticity (= RV - VS). In the wavenumber domain, it is expressed as

$$\hat{\pi} = ik_x\hat{v} - ik_y\hat{u} - fik_z\hat{\eta} = \sqrt{\alpha^2 + \frac{f^2}{N^2}k_z^2}\,\hat{a}^0. \tag{2.21}$$

The linear perturbation potential vorticity in the system is solely carried by the eigenmode $s = 0$, which is therefore called the vortical mode . It is a horizontally nondivergent stagnant motion as described by its eigenvector. The $s = \pm 1$ mode does not carry linear perturbation potential vorticity and is termed the gravity mode since it has the same kinematic structure as linear internal gravity waves. Therefore, the system of small-scale motions must contain both the vortical and gravity modes of motion.

Furthermore, if Fourier expansion in the frequency domain is performed, the state vector $\underline{\Phi}$ can be represented as

$$\underline{\Phi}(\underline{x},t) = \int_{-\infty}^{\infty} d\omega \int\int\int_{-\infty}^{\infty} d^3\underline{k} \sum_{s=0,\pm} \left\{ \underline{\widehat{\phi}}^{s}(\underline{k}) \widetilde{a}^{s}(\underline{k},\omega) e^{-i(\underline{k}\cdot\underline{x}-\omega t)} \right\}, \tag{2.22}$$

where $\widetilde{a}^s(\underline{k},\omega)$ is the frequency Fourier coefficient of $\widehat{a}^s(\underline{k},t)$. The reality condition requires wavenumber–frequency Fourier coefficients of state variables to satisfy $\underline{\widetilde{\Phi}}(-\underline{k},-\omega) = \underline{\widetilde{\Phi}^*}(\underline{k},\omega)$.

The dynamic evolution of eigenmodes can be obtained by applying the linear eigenmode representation of prognostic variables (eq. 2.14) onto the prognostic equations (eq. 2.7), i.e.,

$$\partial_t \widehat{a}^s(\underline{k},t) - i\sigma^s(\underline{k})\, \widehat{a}^s(\underline{k},t) = \underline{\widehat{\phi}}^{s\dagger}(\underline{k})\, \underline{Q}(\underline{k},t). \tag{2.23}$$

Effects of diffusion, dissipation, nonlinear interaction, and external forcing on the dynamic evolution of eigenmodes could be easily studied by specifying the source vector explicitly. If these effects are neglected, the dynamic equations of the eigenmodes become homogeneous and the three eigenmodes are decoupled. In this case, eigenvalues $\sigma^s(\underline{k})$ correspond to intrinsic frequencies of eigenmodes and the relation of $\sigma^s(\underline{k})$ in eq. (2.11) describes the dispersion relation of the eigenmode. The <u>linear</u> vortical mode reduces to steady geostrophic flow, and the <u>linear</u> gravity mode to the linear internal gravity wave. The state vector in an unforced, inviscid, linear system becomes

$$\underline{\Phi}(\underline{x},t) = \int\int\int_{-\infty}^{\infty} d^3\underline{k} \cdot \sum_{s=0,\pm} \left\{ \underline{\widehat{\phi}}^{s}(\underline{k}) \widetilde{b}^{s}(\underline{k}) e^{i(\underline{k}\cdot\underline{x}-s\sigma t)} \right\}. \tag{2.24}$$

Eigenmode amplitudes vanish except on their corresponding dispersion surface, i.e. $\widetilde{a}^s(\underline{k},\omega) = \widetilde{b}^s(\underline{k})\delta(\omega - s\sigma)$.

We have discussed the linear eigenmode representation of the state vector (u,v,η). As mentioned earlier, other forms of the state vector could be more suitable for other applications. On analyzing oceanic velocity measurements, it is sometimes helpful to use the rotary velocity vector. One familiar example is the internal gravity wave which has a preferred clockwise rotation of its horizontal velocity vector. Therefore, we will consider a new state vector, termed the rotary state vector, consisting of two rotary velocity components and the WKB-scaled vertical displacement $N\eta$ which is proportional to the square root of the available potential energy, i.e.,

$$\underline{\Gamma}(\underline{x},t) = \begin{pmatrix} \Gamma_+(\underline{x},t) \\ \Gamma_-(\underline{x},t) \\ \Gamma_0(\underline{x},t) \end{pmatrix} = \frac{1}{\sqrt{2}} \begin{pmatrix} u(\underline{x},t) + iv(\underline{x},t) \\ u(\underline{x},t) - iv(\underline{x},t) \\ \sqrt{2}N\eta(\underline{x},t) \end{pmatrix} . \tag{2.25}$$

Here Γ_+ and Γ_- are counterclockwise and clockwise velocity components. Note that the interpretation of counterclockwise and clockwise rotation of horizontal velocity vector is true only if the positive frequency is considered. The interpretation should be opposite for negative frequencies. All three components of the state vector have the dimension of velocity. The use of the rotary state vector can avoid potential errors in the orientation of the coordinate system during experiments.

The transformation between the rotary state vector and the eigenmode amplitude vector is given by

$$\tilde{\underline{\Gamma}}(\underline{k},\omega) = \sum_{s=0,\pm} \tilde{a}^s(\underline{k},\omega)\hat{\underline{\gamma}}^s(\underline{k}) \tag{2.26}$$

$$\tilde{a}^s(\underline{k},\omega) = \sum_{\mu=0,\pm} \tilde{\Gamma}_\mu(\underline{k},\omega)\, \hat{\gamma}^{s\dagger}_\mu(\underline{k}). \tag{2.27}$$

The transformation vector $\hat{\underline{\gamma}}^s(\underline{k})$ is the eigenvector of the rotary state vector and $\hat{\underline{\gamma}}^{s\dagger}(\underline{k})$ is its adjoint. They can be obtained easily through the relation between the Cartesian and rotary state vectors, and by the use of eigenvectors of the Cartesian state vector, i.e.,

$$\hat{\underline{\gamma}}^{0}(\alpha,\varphi,\nu,\sigma)=\frac{N}{\sqrt{2}\sigma g(\sigma)h(\sigma)}\begin{pmatrix} e^{i\varphi}\\ \\ -e^{-i\varphi}\\ \\ i\sqrt{2}\frac{f}{N}\nu g(\sigma)\end{pmatrix} \tag{2.28}$$

$$\hat{\underline{\gamma}}^{\pm}(\alpha,\varphi,\nu,\sigma)=\frac{\nu f}{2\sigma h(\sigma)}\begin{pmatrix} (\mp\frac{\sigma}{f}+1)e^{i\varphi}\\ \\ (\mp\frac{\sigma}{f}-1)e^{-i\varphi}\\ \\ -\sqrt{2}i\nu\frac{N}{f}g^{-1}(\sigma)\end{pmatrix} \tag{2.29}$$

$$\hat{\underline{\gamma}}^{0\dagger}(\alpha,\varphi,\nu,\sigma)=\frac{N}{\sqrt{2}\sigma g(\sigma)h(\sigma)}\begin{pmatrix} e^{-i\varphi}\\ \\ -e^{i\varphi}\\ \\ -i\sqrt{2}\frac{f}{N}\nu g(\sigma)\end{pmatrix} \tag{2.30}$$

$$\hat{\underline{\gamma}}^{\pm\dagger}(\alpha,\varphi,\nu,\sigma)=\frac{\nu f}{2\sigma h(\sigma)}\begin{pmatrix} \left[\mp\frac{\sigma}{f}h^{2}(\sigma)+1\right]e^{-i\varphi}\\ \\ \left[\mp\frac{\sigma}{f}h^{2}(\sigma)-1\right]e^{i\varphi}\\ \\ \sqrt{2}i\nu\frac{N}{f}g^{-1}(\sigma)\end{pmatrix}. \tag{2.31}$$

Here $\varphi = tan^{-1}(\frac{k_y}{k_x})$ is the orientation of the horizontal wavenumber vector counting counterclockwise from the east. $g(\sigma) = \sqrt{\frac{N^2 - \sigma^2}{\sigma^2 - f^2}} = \frac{|k_z|}{\alpha}$ is the inverse of the aspect ratio, $\nu = sgn(k_z)$ the sign of the vertical wavenumber, and $h(\sigma) = 1 + g^{-2}(\sigma)$. In this representation, the horizontal wavenumber vector is represented as $(k_x, k_y) = (\alpha cos\varphi, \alpha sin\varphi)$, and the vertical wavenumber $k_z = \nu g(\sigma)\alpha$.

There are some distinct features of eigenmodes revealed by their eigenvectors. The vortical mode has equal partition of rotary velocity energy, whereas the gravity mode has the energy ratio between two rotary velocity components depending on the aspect ratio. For the linear gravity mode, the aspect ratio is a function of the frequency only through its dispersion relation.

Using previously discussed state vectors to project eigenmode amplitudes requires substantial wavenumber information which is not available for most oceanic measurements. Alternatively, another state vector is proposed as

$$\underline{\Psi}(\underline{x}, t) = \begin{pmatrix} \Psi_1(\underline{x}, t) \\ \Psi_2(\underline{x}, t) \\ \Psi_3(\underline{x}, t) \end{pmatrix} = \begin{pmatrix} HD(\underline{x}, t) \\ RV(\underline{x}, t) \\ VS(\underline{x}, t) \end{pmatrix} = \begin{pmatrix} \partial_x u + \partial_y v \\ \partial_x v - \partial_y u \\ f\partial_z \eta \end{pmatrix}. \qquad (2.32)$$

All components of this state vector have the dimension of the vorticity. They are the horizontal divergence, vertical component of relative vorticity, and vortex stretching. Corresponding eigenvectors are found as

$$\underline{\hat{\psi}}^0(\underline{k}) = \frac{N\alpha^2}{\sigma K} \begin{pmatrix} 0 \\ 1 \\ -\frac{f^2 k_z^2}{N^2 \alpha^2} \end{pmatrix} \qquad (2.33)$$

$$\underline{\hat{\psi}}^{\pm}(\underline{k}) = \frac{k_z \alpha f}{\sqrt{2}\sigma K} \begin{pmatrix} \mp i\frac{\sigma}{f} \\ 1 \\ 1 \end{pmatrix} \tag{2.34}$$

$$\underline{\hat{\psi}}^{0\dagger}(\underline{k}) = \frac{N}{\sqrt{2}\sigma K} \begin{pmatrix} 0 \\ 1 \\ -1 \end{pmatrix} \tag{2.35}$$

$$\underline{\hat{\psi}}^{\pm\dagger}(\underline{k}) = \frac{f g(\sigma)}{2\sigma K} \begin{pmatrix} \pm i\frac{\sigma}{f} h(\sigma) \\ 1 \\ \frac{N^2}{f^2} g^{-2}(\sigma) \end{pmatrix} . \tag{2.36}$$

Examining polarizations of the gravity and vortical modes (eqs. 2.33 and 2.34), their important kinematic structures are revealed. The vortical mode is horizontally nondivergent and carries linear perturbation potential vorticity. The ratio between its relative vorticity and vortex stretching is $\frac{-N^2\alpha^2}{f^2 k_z^2}$. Conversely, the gravity mode is horizontally divergent, and does not carry linear perturbation potential vorticity for its relative vorticity cancels with vortex stretching. Since the eigenvalue σ is the intrinsic frequency of the linear gravity mode, the frequency spectral ratio between horizontal divergence and relative vorticity must be $\frac{\omega^2}{f^2}$ and their phase spectrum should be 90° out of phase.

A slightly different state vector has been proposed by Olbers (1988), defined as

$$\underline{\Lambda}(\underline{x}, t) = \begin{pmatrix} \partial_x u + \partial_y v \\ \\ \partial_x v - \partial_y u \\ \\ \frac{1}{\rho_0 f}(\partial_x \partial_x + \partial_y \partial_y) p \end{pmatrix}. \tag{2.37}$$

Eigenvectors and their adjoints are found as

$$\hat{\underline{\Lambda}}^0(\underline{k}) = \frac{N\alpha^2}{\sigma K} \begin{pmatrix} 0 \\ \\ 1 \\ \\ 1 \end{pmatrix} \tag{2.38}$$

$$\hat{\underline{\Lambda}}^{\pm}(\underline{k}) = \frac{k_z \alpha f}{\sqrt{2}\sigma K} \begin{pmatrix} \mp i \frac{\sigma}{f} \\ \\ 1 \\ \\ 1 - \frac{\sigma^2}{f^2} \end{pmatrix} \tag{2.39}$$

$$\hat{\underline{\Lambda}}^{0\dagger}(\underline{k}) = \frac{K f^2}{N\alpha^2 \sigma} \begin{pmatrix} 0 \\ \\ \frac{\sigma^2}{f^2} - 1 \\ \\ 1 \end{pmatrix} \tag{2.40}$$

$$\hat{\underline{\lambda}}^{\pm\dagger}(\underline{k}) = \frac{Kf}{\sqrt{2}\sigma k_z \alpha}\begin{pmatrix} \pm i\frac{\sigma}{f} \\ 1 \\ -1 \end{pmatrix}. \tag{2.41}$$

This state vector will be used in the section 2.3 of the application of linear eigenmode decomposition onto a prototype nonlinear vortical motion, the monopole.

The purpose of the linear eigenmode representation is to decompose small-scale motions into gravity waves and vortical motions. The main distinction between the gravity wave and the vortical motion is based on the perturbation potential vorticity which includes both the linear and the nonlinear components, whereas the distinction between the gravity mode and the vortical mode is based on the linear perturbation potential vorticity alone. Apparently, for linear, unforced small-scale motions, the linear eigenmode representation can precisely determine the gravity wave and vortical motion components since only the linear perturbation potential vorticity exists. This fact will be illustrated in the next section. For nonlinear small scale motions, an exact linear decomposition into gravity waves and vortical motions is intrinsically impossible. An example of a nonlinear vortical motion will be illustrated in section 2.3 where the effectiveness of the linear eigenmode representation depends on the Rossby and Burger numbers.

2.2 Geostrophic Adjustment Problem

In this section, the familiar geostrophic adjustment problem will be studied applying the linear eigenmode representation. The primary purpose is to justify that the linear eigenmode representation can separate the gravity wave and the vortical motion unambiguously in the linear system.

The geostrophic adjustment problem was first studied by Rossby (1937, 1938) who examined the competitive gravitational and Coriolis forces in response to disturbances in a small-scale system. His work has been extended by other researchers such as Cahn (1945), Gill (1976, 1982), and Middleton (1987). Despite different approaches and initial conditions, the disturbed field eventually approaches a steady state of the geostrophic balance after gravity waves carry away a fraction of energy from the adjusted region.

Specifying a step function of sea surface displacement, Gill (1976, 1982) studied the steady state and transient solution separately. The initial system contains the potential energy only. In the final state, the kinetic energy is only one third of the loss of the initial potential energy. The other two thirds is carried away by gravity waves. In a recent study, Middleton (1987) proved that the ratio of the kinetic energy in the final state and the loss of the initial potential energy depends on the horizontal scale of the initial disturbance relative to the Rossby radius of deformation.

Based on the linear eigenmode representation, disturbances in the system are regarded as a linear superposition of gravity and vortical components. The total energy and the perturbation potential vorticity of the system are decomposed into its gravity and vortical components as mentioned earlier. Both gravity waves and geostrophic flows conserve their total energy while conversion between the potential and kinetic energy of each eigenmode may occur.

A linear system of Boussinesq, incompressible, inviscid shallow water equations in a barotropic ocean on an f–plane are considered. A constant depth, H, of the ocean is assumed. Dynamic equations are described as

$$\partial_t u - fv = -g\partial_x \xi \tag{2.42}$$

$$\partial_t v + fu = -g\partial_y \xi \tag{2.43}$$

$$\partial_t \xi + H(\partial_x u + \partial_y v) = 0. \tag{2.44}$$

Here, ξ is the surface displacement. Three prognostic variables in the system are u, v, and ξ. The dynamic equations in the Fourier wavenumber space can be written as

$$\partial_t \begin{pmatrix} \widehat{u} \\ \widehat{v} \\ \widehat{\xi} \end{pmatrix} + \begin{pmatrix} 0 & -f & -igk_x \\ f & 0 & -igk_y \\ -ik_xH & -ik_yH & 0 \end{pmatrix} \begin{pmatrix} \widehat{u} \\ \widehat{v} \\ \widehat{\xi} \end{pmatrix} = \begin{pmatrix} 0 \\ 0 \\ 0 \end{pmatrix}. \tag{2.45}$$

This system is linear and homogeneous. Since the state matrix is not in a diagonal form, three prognostic variables are coupled dynamically. Eigenvalues σ^s and eigenvectors $\underline{\widehat{\phi}}^s$ of the state matrix are

$$\sigma^s(\underline{k}) = s\sqrt{f^2 + gH\alpha^2} = s\sigma(\underline{k}), \qquad s = 0, +, - \tag{2.46}$$

$$\underline{\widehat{\phi}}^0(\underline{k}) = \frac{\sqrt{gH}}{\sigma} \begin{pmatrix} k_y \\ -k_x \\ -i\dfrac{f}{g} \end{pmatrix} \tag{2.47}$$

$$\hat{\underline{\phi}}^{\pm}(\underline{k}) = \frac{1}{\sqrt{2}\sigma\alpha}\begin{pmatrix} \mp\sigma k_x + ifk_y \\ \mp\sigma k_y - ifk_x \\ -H\alpha^2 \end{pmatrix}. \tag{2.48}$$

Three eigenmodes are determined. The $s = 0$ is the vortical mode, and $s = \pm$ two gravity modes. Adjoint eigenvectors can also be obtained as

$$\hat{\underline{\phi}}^{0\dagger} = \frac{\sqrt{gH}}{\sigma}\begin{pmatrix} k_y \\ -k_x \\ -i\frac{f}{H} \end{pmatrix} \tag{2.49}$$

$$\hat{\underline{\phi}}^{\pm\dagger} = \frac{1}{\sqrt{2}\sigma\alpha}\begin{pmatrix} -\sigma^{\pm}k_x - ifk_y \\ -\sigma^{\pm}k_y + ifk_x \\ -g\alpha^2 \end{pmatrix}. \tag{2.50}$$

Unique transformations among eigenmode amplitudes and prognostic variables are expressed as

$$\begin{pmatrix} \hat{a}^0(\underline{k},t) \\ \hat{a}^+(\underline{k},t) \\ \hat{a}^-(\underline{k},t) \end{pmatrix} = \begin{pmatrix} k_y\frac{\sqrt{gH}}{\sigma} & -k_x\frac{\sqrt{gH}}{\sigma} & i\frac{f}{H}\frac{\sqrt{gH}}{\sigma} \\ \frac{-\sigma k_x - ifk_y}{\sqrt{2}\sigma\alpha} & \frac{-\sigma k_y + ifk_x}{\sqrt{2}\sigma\alpha} & -\frac{g\alpha^2}{\sqrt{2}\sigma\alpha} \\ \frac{\sigma k_x - ifk_y}{\sqrt{2}\sigma\alpha} & \frac{\sigma k_y + ifk_x}{\sqrt{2}\sigma\alpha} & -\frac{g\alpha^2}{\sqrt{2}\sigma\alpha} \end{pmatrix} \begin{pmatrix} \hat{u}(\underline{k},t) \\ \hat{v}(\underline{k},t) \\ \hat{\xi}(\underline{k},t) \end{pmatrix} \tag{2.51}$$

$$\begin{pmatrix} \hat{u}(\underline{k},t) \\ \hat{v}(\underline{k},t) \\ \hat{\xi}(\underline{k},t) \end{pmatrix} = \begin{pmatrix} k_y\frac{\sqrt{gH}}{\sigma} & \frac{-\sigma k_x + ifk_y}{\sqrt{2}\sigma\alpha} & \frac{\sigma k_x + ifk_y}{\sqrt{2}\sigma\alpha} \\ -k_x\frac{\sqrt{gH}}{\sigma} & \frac{-\sigma k_y - ifk_x}{\sqrt{2}\sigma\alpha} & \frac{\sigma k_y - ifk_x}{\sqrt{2}\sigma\alpha} \\ -i\frac{f}{g}\frac{\sqrt{gH}}{\sigma} & -\frac{H\alpha^2}{\sqrt{2}\sigma\alpha} & -\frac{H\alpha^2}{\sqrt{2}\sigma\alpha} \end{pmatrix} \begin{pmatrix} \hat{a}^0(\underline{k},t) \\ \hat{a}^+(\underline{k},t) \\ \hat{a}^-(\underline{k},t) \end{pmatrix}. \tag{2.52}$$

The above decomposition assures that the total energy spectrum of the system is diagonalized into energy spectra of three eigenmodes, i.e.,

$$\frac{1}{2}\langle \hat{u}\hat{u}^* + \hat{v}\hat{v}^* + \frac{g}{H}\hat{\xi}\hat{\xi}^* \rangle = \frac{1}{2}\langle \hat{a}^0\hat{a}^{0*} + \hat{a}^+\hat{a}^{+*} + \hat{a}^-\hat{a}^{-*} \rangle. \tag{2.53}$$

Note a small aspect ratio $\delta = \frac{H}{L}$ has been assumed for the system of shallow water equations. Quantities of $O(\delta^2)$ or smaller have been neglected. The vertical kinetic energy is neglected since it is an order of δ^2 compared to the horizontal kinetic energy.

The linear perturbation potential vorticity in a barotropic ocean is defined as $\pi = \partial_x v - \partial_y u - f\frac{\xi}{H}$. At any given wave vector, the linear perturbation potential vorticity is solely carried by the vortical mode.

Prognostic equations of eigenmode amplitudes are described as

$$\partial_t \hat{a}^0(\underline{k},t) = 0 \tag{2.54}$$

$$\partial_t \hat{a}^{\pm}(\underline{k}, t) - i\sigma^{\pm}(\underline{k})\hat{a}^{\pm}(\underline{k}, t) = 0. \tag{2.55}$$

The vortical mode amplitude is steady, whereas the gravity mode propagates with its intrinsic frequency $\sigma^{\pm}(\underline{k})$. According to the reality condition of state variables, Fourier coefficients have to satisfy

$$\hat{u}(\underline{k}, t) = \hat{u}^*(-\underline{k}, t) \tag{2.56}$$

$$\hat{v}(\underline{k}, t) = \hat{v}^*(-\underline{k}, t) \tag{2.57}$$

$$\hat{\xi}(\underline{k}, t) = \hat{\xi}^*(-\underline{k}, t). \tag{2.58}$$

Similarly, the eigenmode amplitude of the gravity mode has to satisfy $\hat{a}^{+}(\underline{k}, t) = \hat{a}^{-*}(-\underline{k}, t)$.

Applying the concept of the linear eigenmode representation, the geostrophic adjustment problem can be easily attacked. Initial disturbances of surface displacement or velocity fields can be decomposed to amplitudes of the gravity and vortical modes using eq. 2.51. Therefore, the total energy of the gravity and vortical modes are determined. Furthermore, the potential and kinetic energy of the gravity and vortical modes are obtained using polarization relations of eigenmodes.

As a simple example, the initial disturbance of surface displacement $\hat{\xi}(\underline{k}, 0)$ is imposed on the system. Amplitudes of the gravity and vortical modes are determined as

$$\hat{a}^0(\underline{k}, 0) = \hat{a}^0(\underline{k}) = i\frac{f}{H}\frac{\sqrt{gH}}{\sigma}\hat{\xi}(\underline{k}, 0) \tag{2.59}$$

$$\widehat{a}^{\pm}(\underline{k},0) = -\frac{g\alpha}{\sqrt{2}\sigma}\widehat{\xi}(\underline{k},0). \tag{2.60}$$

Eigenmode amplitudes evolve in time according to their dynamics.

Assuming a statistically homogeneous field, wavenumber spectra of the total energy $E(\underline{k},t)$, potential energy $E_p(\underline{k},t)$, and kinetic energy $E_k(\underline{k},t)$ are defined as

$$E^s(\underline{k},t)\delta(\underline{k}-\underline{k}') = \frac{1}{2}\langle\widehat{a}^s(\underline{k},t)a^{s*}(\underline{k}',t)\rangle \tag{2.61}$$

$$E_p^s(\underline{k},t)\delta(\underline{k}-\underline{k}') = \frac{1}{2}\frac{g}{H}\langle\widehat{\xi}^s(\underline{k},t)\widehat{\xi}^{s*}(\underline{k}',t)\rangle \tag{2.62}$$

$$E_k^s(\underline{k},t)\delta(\underline{k}-\underline{k}') = \frac{1}{2}\langle\widehat{u}^s(\underline{k},t)\widehat{u}^{s*}(\underline{k}',t) + \widehat{v}^s(\underline{k},t)\widehat{v}^{s*}(\underline{k}',t)\rangle. \tag{2.63}$$

Total wavenumber energy spectra of the gravity and vortical modes at the initial time are obtained as

$$E^0(\underline{k},0) = E^0(\underline{k}) = \frac{1}{1+R^2\alpha^2}E_p(\underline{k},0) \tag{2.64}$$

$$E^g(\underline{k},0) = \sum_{\pm}E^{\pm}(\underline{k},0) = \frac{1}{1+R^{-2}\alpha^{-2}}E_p(\underline{k},0). \tag{2.65}$$

Here $R = \sqrt{\frac{gH}{f^2}}$ is the Rossby radius of deformation. E^g and E^0 are the total energy spectra of the gravity mode and of the vortical mode, respectively. $E_p(\underline{k},0)$ is the initial potential energy. Since there is no sink nor source of the energy in this system, the total energy of eigenmodes must be conserved. The partition of eigenmode energy depends on the scale of the initial disturbance relative to the Rossby radius of deformation (Figure 1). The vortical mode is dominant at scales greater than the Rossby radius of deformation, whereas the gravity mode is dominant at smaller scales. They are equi–partitioned at the Rossby radius of deformation.

At the final state, only the steady vortical mode is left after the gravity wave propagates away. The potential and kinetic energy components of the vortical mode are expressed as

$$E_k^0(\underline{k}) = \frac{\alpha^2 R^2}{(1+\alpha^2 R^2)^2} E_p(\underline{k}, 0) \tag{2.66}$$

$$E_p^0(\underline{k}) = \frac{1}{(1+\alpha^2 R^2)^2} E_p(\underline{k}, 0). \tag{2.67}$$

They are displayed in Figure 2. At the Rossby radius of deformation, the kinetic energy of the vortical mode reaches its maximum and the potential and kinetic energy components are identical. One third of the loss of the initial potential energy has been converted to the kinetic energy of the vortical mode, whereas the other two thirds must be carried away by gravity waves.

This example clearly illustrates that the geostrophic adjustment problem can be easily understood using the linear eigenmode representation. The main distinction between two types of motions in the system is the linear perturbation potential vorticity. This fact is fruitfully used. Any given initial disturbance of surface displacement or velocity field can be regarded as the linear superposition of the gravity and vortical components. Since the system is linear, the separation of these two types of motions is unambiguous and efficient using the linear eigenmode representation.

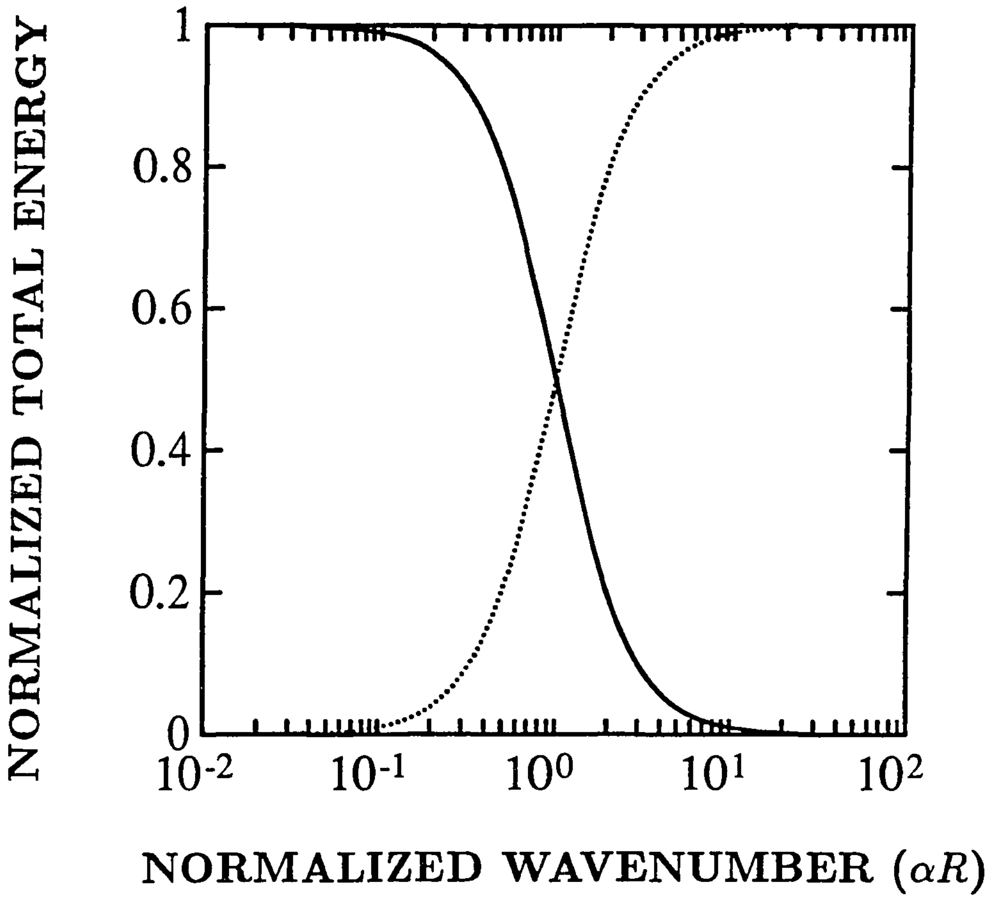

Figure 1: Total energy of the gravity and vortical modes normalized by the initial potential energy in the geostrophic adjustment problem. The solid line denotes the normalized energy of the vortical mode, and the dotted line of the gravity mode. The energy partition depends on the ratio between the perturbation scale and the Rossby radius of deformation $\sqrt{\frac{gH}{f^2}}$.

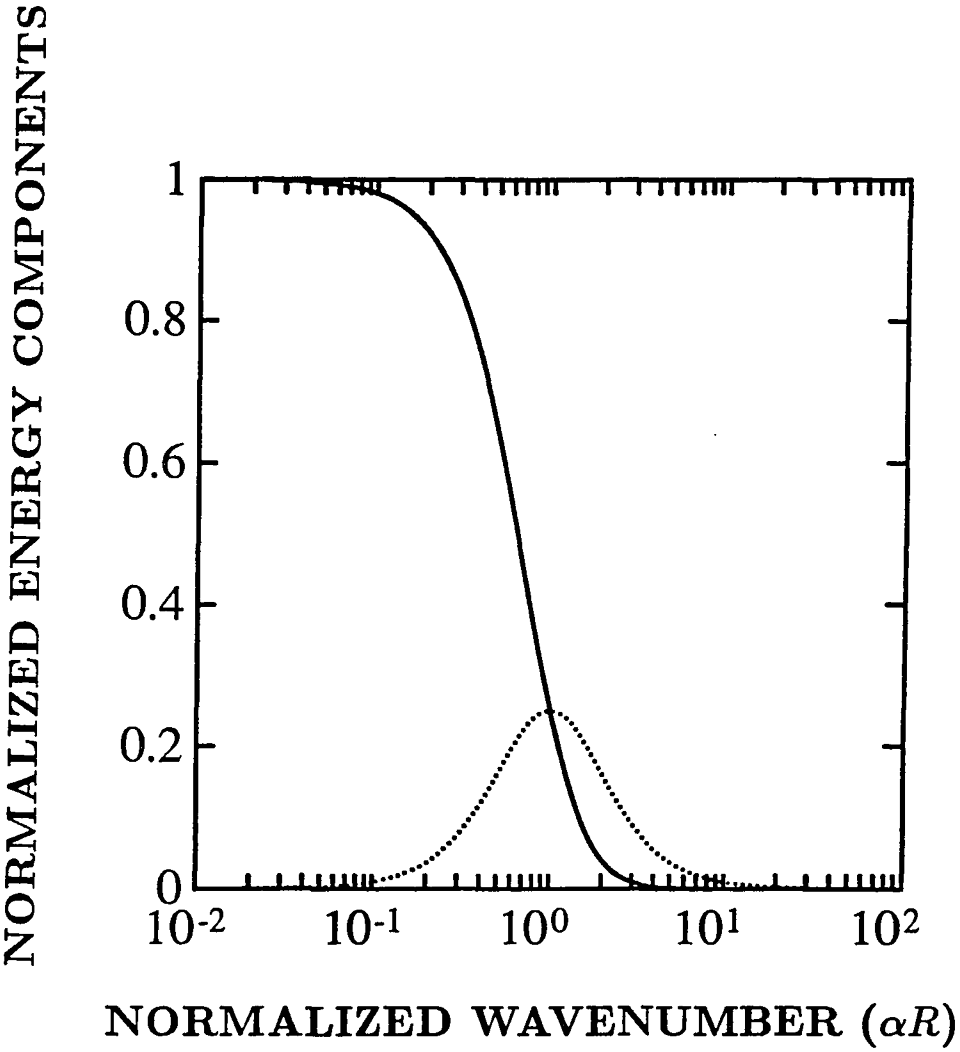

Figure 2: Potential and kinetic energy of the vortical mode normalized by the initial potential energy as a function of initial disturbance scale normalized by the Rossby radius of deformation. The solid line denotes the normalized kinetic energy of the vortical mode, and the dotted line is the normalized potential energy.

2.3 Monopole Motion

To illustrate the application of the linear eigenmode representation on a nonlinear system, a prototype of nonlinear vortical motions will be discussed. One simple example is the monopole motion. McWilliams (1985) suggested that oceanic submesoscale coherent vortices (SCV) are the monopole motion in a cyclostrophic balance, i.e.,

$$fu_\theta + \frac{u_\theta^2}{r} = \frac{1}{\rho_0}\partial_r p. \tag{2.68}$$

Here, u_θ is the azimuthal velocity, r the radial distance, and p the pressure. The relation between the velocity and pressure fields is determined by the above dynamic balance as

$$u_\theta = \frac{rf}{2}\left\{-1 + \sqrt{1 + \frac{4}{\rho_0 f^2 r}\partial_r p}\right\} \tag{2.69}$$

providing that the azimuthal velocity remains finite in the far field. If the azimuthal independence is assumed, the monopole is horizontally nondivergent.

Intuitively, SCV are vortical motions for their carrying the perturbation potential vorticity. The pressure field of SCV has a Gaussian distribution both in the vertical and horizontal (McWilliams, 1985). Two types of monopoles will be discussed for illustrations. The first type has a Gaussian pressure field with a maximum in its center and will be termed a hot monopole. The second type has a Gaussian pressure field with a minimum in its center and will be called a cold monopole. Pressure distributions of the hot and cold monopoles are specified as

$$p^{(I)} = P_0 e^{-(\frac{r^2}{L_0^2} + \frac{z^2}{H_0^2})} \tag{2.70}$$

$$p^{(II)} = P_0 \left\{ 1 - e^{-(\frac{r^2}{L_0^2}+\frac{z^2}{H_0^2})} \right\}. \tag{2.71}$$

Here, L_0 and H_0 are horizontal and vertical scales of the Gaussian pressure field, and P_0 the pressure scale. Corresponding velocity fields for the hot and cold monopoles are determined as

$$u_\theta^{(I)} = \frac{fr}{2}\left[-1 + \sqrt{1 - 2R_o e^{-(\frac{r^2}{L_0^2}+\frac{z^2}{H_0^2})}} \right] \tag{2.72}$$

$$u_\theta^{(II)} = \frac{fr}{2}\left[-1 + \sqrt{1 + 2R_o e^{-(\frac{r^2}{L_0^2}+\frac{z^2}{H_0^2})}} \right], \tag{2.73}$$

where the Rossby number is defined as $R_o = \frac{4U_0}{fL_0}$ with the velocity scale $U_0 = \frac{P_0}{\rho_0 f L_0}$. For the hot monopole, an additional constraint $R_o \leq \frac{1}{2}$ has to be made in order to have non–imaginary velocity field.

Amplitudes of eigenmodes can be determined from fields of horizontal divergence (HD), the scaled Laplacian of the pressure field ($\mathcal{L}P$), and the vertical component of relative vorticity (RV) using eqs. 2.1 and 2.41 as

$$\hat{a}^0(\underline{k}) = \frac{Kf^2}{N\alpha^2\sigma}\left\{ (\frac{\sigma^2}{f^2} - 1)\widehat{RV}(\underline{k}) + \widehat{\mathcal{L}P}(\underline{k}) \right\} \tag{2.74}$$

$$\hat{a}^\pm(\underline{k}) = \frac{Kf}{\sqrt{2}\sigma k_z \alpha}\left\{ \widehat{RV}(\underline{k}) - \widehat{\mathcal{L}P}(\underline{k}) \right\}. \tag{2.75}$$

Here the overhat $\hat{}$ denotes the wavenumber coefficient.

For the hot monopole, the relative vorticity $RV^{(I)}$ and $\mathcal{L}P^{(I)}$ are obtained from the prescribed pressure distribution

$$\mathcal{L}P^{(I)} = \frac{1}{\rho_0 f}(\partial_x\partial_x + \partial_y\partial_y)p^{(I)} = R_o f \cdot e^{-(\frac{r^2}{L_0^2}+\frac{z^2}{H_0^2})}(\frac{r^2}{L_0^2} - 1) \tag{2.76}$$

$$\begin{aligned} RV^{(I)} &= \frac{1}{r}\partial_r(ru_\theta)^{(I)} \\ &= R_o f \cdot e^{-(\frac{r^2}{L_0^2}+\frac{z^2}{H_0^2})} \left[\frac{-2}{1+\sqrt{1-2R_o e^{-(\frac{r^2}{L_0^2}+\frac{z^2}{H_0^2})}}} + \frac{r^2}{L_0^2} \frac{1}{\sqrt{1-2R_o e^{-(\frac{r^2}{L_0^2}+\frac{z^2}{H_0^2})}}} \right]. \end{aligned} \tag{2.77}$$

To the limit of a small Rossby number, $\mathcal{LP}^{(I)}$ and $RV^{(I)}$ are identical and the gravity mode does not exist in the system (eq. 2.75). Since the Rossby number is a measure of the nonlinearity of the system, the previous statement simply justifies the exactness of the linear eigenmode representation in a linear system.

Numerical simulations of hot monopoles were performed. First, pressure fields of hot monopoles with various horizontal and vertical scales, L_0 and H_0, are simulated. Corresponding velocity fields are calculated for various Rossby numbers. Accordingly, $\mathcal{L}P^{(I)}$ and $RV^{(I)}$ are determined, and amplitudes of the gravity and vortical modes are estimated. Finally, energy of the gravity and vortical modes are obtained by integrating their wavenumber energy spectra over the complete wavenumber space. The energy ratio between the gravity and vortical components is found depending on two global parameters only. They are the Rossby number and Burger number defined as $B = \frac{N^2 H_0^2}{f^2 L_0^2}$. Contours of constant energy ratios versus R_o and B are presented in Figure 3. The linear eigenmode representation clearly demonstrates that the vortical mode is the dominant component in the hot monopole. The energy ratio increases from 10^{-13} to 10^{-3} with increasing Rossby and Burger numbers.

A similar analysis can be made for the cold monopole. $\mathcal{L}P^{(II)}$ and $RV^{(II)}$ of the cold monopole are described as

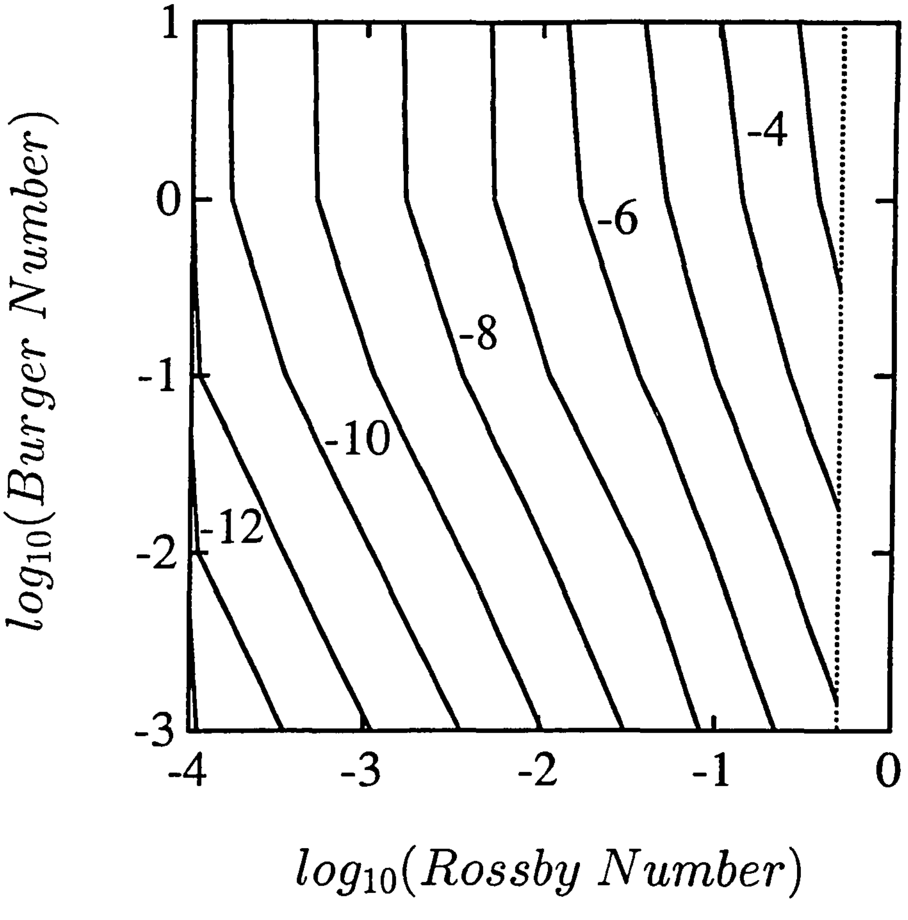

Figure 3: Energy ratio between the gravity and vortical modes for the hot monopole.

$$\mathcal{L}P^{(II)} = \frac{1}{\rho_0 f}(\partial_x\partial_x + \partial_y\partial_y)p^{(II)} = R_o f \cdot e^{-(\frac{r^2}{L_0^2}+\frac{z^2}{H_0^2})}(1 - \frac{r^2}{L_0^2}) \tag{2.78}$$

$$\begin{aligned} RV^{(II)} &= \frac{1}{r}\partial_r(ru_\theta)^{(II)} \\ &= R_o f \cdot e^{-(\frac{r^2}{L_0^2}+\frac{z^2}{H_0^2})} \left[\frac{2}{1+\sqrt{1+2R_o e^{-(\frac{r^2}{L_0^2}+\frac{z^2}{H_0^2})}}} - \frac{r^2}{L_0^2}\frac{1}{\sqrt{1+2R_o e^{-(\frac{r^2}{L_0^2}+\frac{z^2}{H_0^2})}}} \right]. \end{aligned} \tag{2.79}$$

Again, the gravity mode vanishes as the Rossby number approaches zero. The energy ratio between the gravity and vortical components is presented in Figure 4. The vortical mode is the dominant component at small Rossby numbers. The energy ratio increases from 10^{-9} to 10^{-2} with increasing Rossby and Burger numbers.

The monopole is a pure vortical motion. The nonvanishing gravity mode component is due to the nonlinearity of the system. The Rossby number is a measure of the nonlinearity. The energy of the gravity mode vanishes when Rossby numbers approach zero. Since the energy decomposition is virtually a linear operation, it is intrinsically infeasible to perform in a nonlinear system. Nonetheless, the linear eigenmode representation is able to justify that the vortical mode is the dominant component in the system.

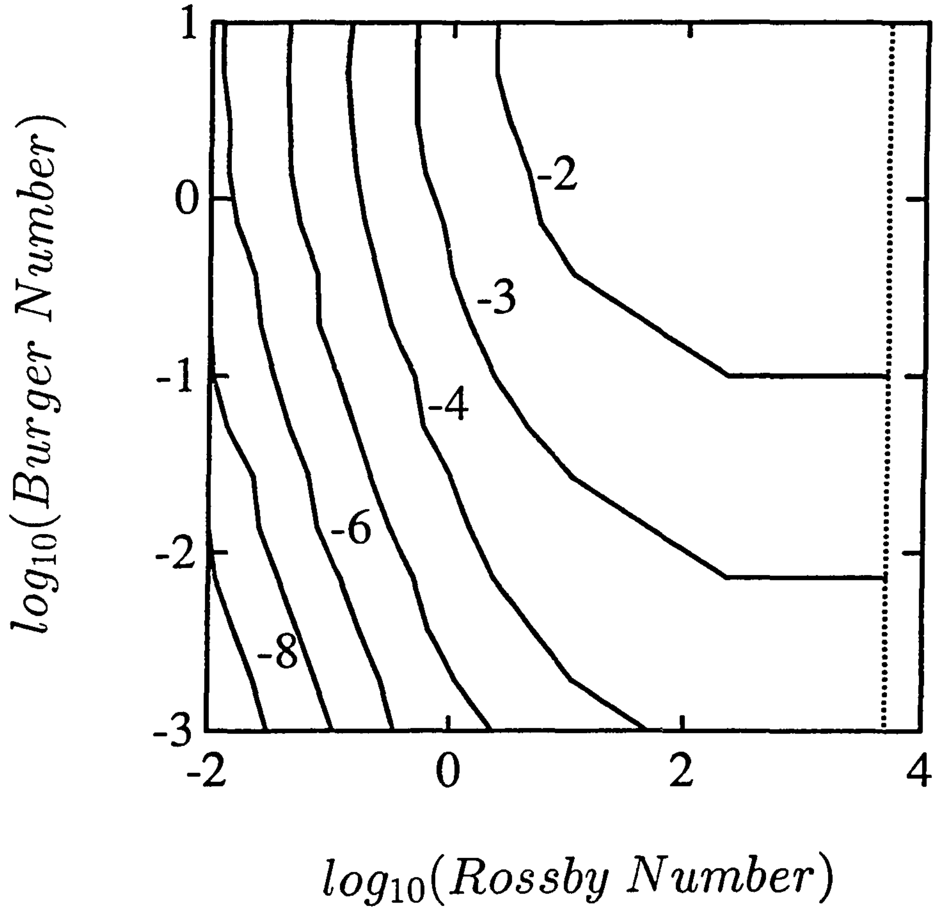

Figure 4: Energy ratio between the gravity and vortical modes for the cold monopole.

Chapter 3

Normal Mode Decomposition of IWEX

Theoretically, the system of small–scale motion supports both the gravity wave and vortical motion. This fact has been demonstrated from the linear eigenmode representation of the system. Therefore, one would expect that observed small-scale fluctuations in the ocean must contain both the gravity wave and vortical motion components. Indeed, small–scale fluctuations of temperature and velocity measured from the IWEX experiment can not be explained by the linear internal wave alone (Müller et al., 1978).

In this chapter, an attempt will be made to separate small–scale oceanic fluctuations into the gravity and vortical modes using the linear eigenmode representation. This separation scheme is referred to as the normal mode decomposition. It can be achieved conveniently using fields of horizontal divergence (HD), vertical component of relative vorticity (RV), and vortex stretching (VS). Estimating them requires oceanic measurements of horizontal velocity and temperature at a sufficient spatial resolution. There are very few oceanic measurements available for such calculations. Most often, oceanic measurements are taken in one–dimensional time or space domains. It is even difficult to obtain temporal variations of these field. The most suitable oceanic measurements to apply the normal mode decomposition to are from the IWEX experiments.

The estimation of horizontally averaged HD, RV, and VS has been attempted by Müller et al. (1988) using IWEX measurements. Frequency spectral estimates of HD and RV were interpreted as frequency–horizontal wavenumber spectra of HD and RV subjected to a lowpass horizontal wavenumber filter. Here, a rigorous analysis will be made to show that frequency spectral estimates of HD and RV were also contaminated by each other.

Area averaged VS was estimated indirectly from the time integration of HD (Müller et al., 1988). Since HD, RV, and VS are three independent prognostic variables in the system of small–scale motions, it is impossible to estimate them using horizontal velocity measurements alone. Indeed, it can be shown that their estimates of VS include the gravity mode component only. Here, VS will be estimated using temperature measurements instead.

The configuration and measurements of IWEX will be described in the next section. Methods of estimating HD, RV, VS, and IR (inverse Richardson number), their spectral analysis, and comparisons with the GM-76 spectrum model will be discussed in sections 3 and 4. The general concept of the normal mode decomposition of relative vorticity and horizontal kinetic energy spectra will be discussed in the last section.

3.1 Description of IWEX

The IWEX was conducted in late 1973 during a 42-day period. A trimooring array was designed on which 20 current meters (17 VACM and 3 EG&G 850) and temperature sensors were deployed in the main thermocline in the Sargasso Sea (27°44′ N, 69°51′ W). Horizontal velocity components, temperature, and temperature difference over a vertical distance of 1.74 m were measured. Horizontal spacing between sensors ranged from 1.4 m to 1600 m and vertical spacing from 2.1 m to 1447 m. Sampling interval was 225 s, except at the lowest level (2050 m depth) which was sampled every 900 s. The trimooring array was a nearly perfect tetrahedron (roughly 6 km on a side) with the apex on top of the main thermocline at 604 m depth and the deepest current meter and temperature sensor at a depth of 2050 m. A schematic diagram of IWEX is shown in Figure 5. The mooring was very stable during the entire experiment. Pressure records showed ±0.2 m displacement at the apex and about ±6 m at 3000 m. A detailed description of IWEX was given by Tarbell et al. (1976). The IWEX measurements provide an opportunity to estimate fields of spatial gradients in the time and space scales of small-scale motions. Measurements from 15 current meters and temperature sensors at five horizontal planes, where measurements are available at all three legs, are used. Characteristics of the five IWEX levels are described in the Table 1.

3.2 Estimates of HD and RV

Estimates of *HD* and *RV* have been made by Müller et al. (1988) using Stokes' and Gauss' theorem as

$$\overline{HD} = \frac{1}{\mathcal{A}} \int d\mathcal{A} (\partial_x u + \partial_y v) = \frac{1}{\mathcal{A}} \oint \underline{u} \cdot d\underline{n} \tag{3.1}$$

$$\overline{RV} = \frac{1}{\mathcal{A}} \int d\mathcal{A} (\partial_x v - \partial_y u) = \frac{1}{\mathcal{A}} \oint \underline{u} \cdot d\underline{t} \, , \tag{3.2}$$

where $\underline{t}$ and $\underline{n}$ are tangential and normal unit vectors along the circumference, and

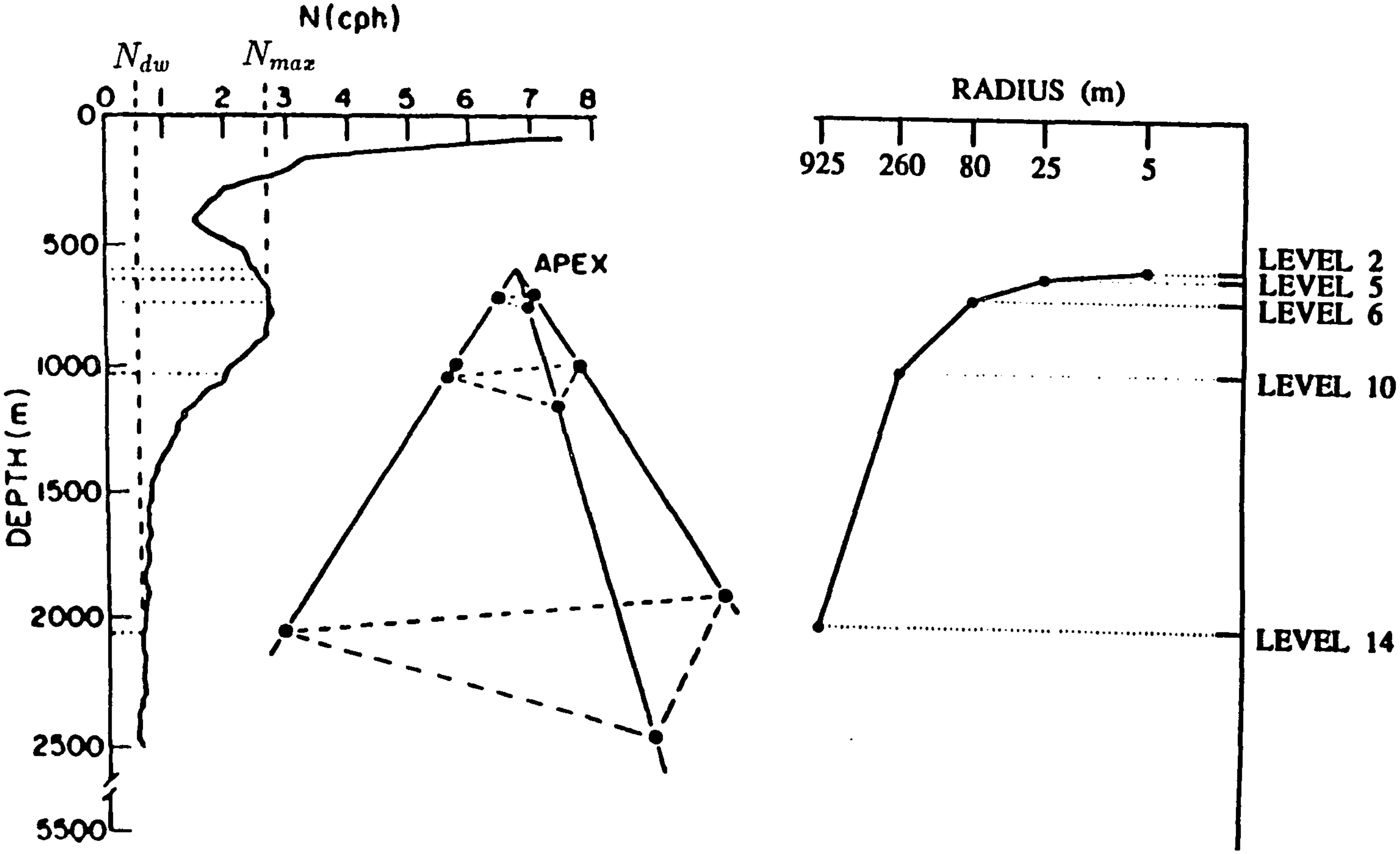

Figure 5: Schematic view of the geometry of the IWEX array and profiles of the Brunt–Väisälä frequency $N(z)$ and horizontal radius $R(z)$. Points indicate current meter positions. There are ten more current meters near the apex which are not shown. The levels that contain three current meters are indicated. The maximum Brunt–Väisälä frequency in the main thermocline is $N_{max} = 2.76$ cph. In the deep water column below 2050 m N is almost constant, $N_{dw} = 0.36$ cph.

Table 1: Characteristics of five IWEX levels with three current meters

Level	Depth (m)	Radius (m)	N (cph)	Number of points
2	606	4.9	2.54	1800
5	640	25.4	2.60	12000
6	731	80.3	2.76	12000
10	1023	260.0	2.05	4800
14	2050	925.0	0.66	3900

$\mathcal{A}$ is the area of the circle connecting three current meters. The overbar indicates that the quantity is estimated over an area $\mathcal{A}$. A schematic diagram of the configuration of current meters of IWEX at one horizontal plane is shown in Figure 6. Horizontal velocity measurements are first converted to their normal and tangential components, and the circle integration is approximated using three points on the circle. Specifically, $\overline{HD}$ and $\overline{RV}$ are estimated as

$$\overline{HD} = \sum_{i=A,B,C} u_i^n \frac{2}{3R} \tag{3.3}$$

$$\overline{RV} = \sum_{i=A,B,C} u_i^t \frac{2}{3R}. \tag{3.4}$$

Here, u^n and u^t are normal and tangential velocity components, R the radius of the circle, and A, B, C indices of three mooring legs.

An alternative approach can be made by obtaining estimates of means and gradients of horizontal velocity components using the linear regression fit of horizontal velocity measurements:

$$u_i = \overline{u} + \overline{\partial_x u}\,\Delta x_i + \overline{\partial_y u}\,\Delta y_i, \quad i = A, B, C \tag{3.5}$$

$$v_i = \overline{v} + \overline{\partial_x v}\,\Delta x_i + \overline{\partial_y v}\,\Delta y_i, \quad i = A, B, C. \tag{3.6}$$

Here, $\overline{u}$ and $\overline{v}$ are estimates of mean horizontal velocity components, and $\overline{\partial_x u}$, $\overline{\partial_y u}$, $\overline{\partial_x v}$, and $\overline{\partial_y v}$ are estimates of east and north gradients of horizontal velocity components. Δx and Δy are horizontal distances of current meters from the center of the circle. Six velocity measurements at each horizontal plane (two horizontal velocity components at three legs on the circle) are used to estimate the mean velocity and

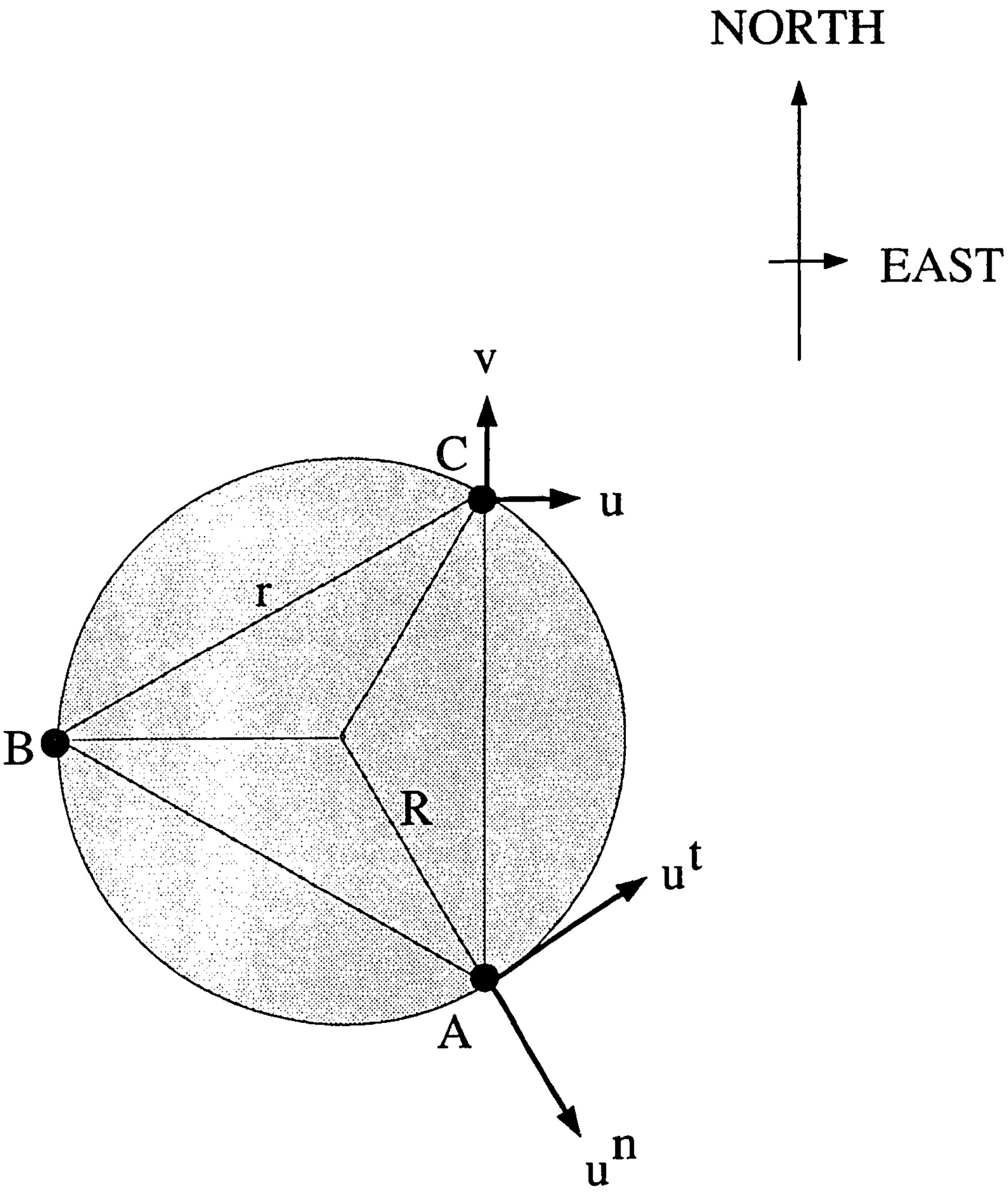

Figure 6: Schematic diagram of current meter configuration of IWEX at one horizontal level. R is the radius of the circles connecting three current meters, and r is the horizontal separation between current meters.

mean horizontal velocity gradients. Accordingly, $\overline{HD}$ and $\overline{RV}$ can be obtained from estimates of velocity gradients as

$$\overline{HD} = \frac{2}{3R}\left(\frac{u_A + u_C}{2} - u_B\right) + \frac{1}{\sqrt{3}R}(v_C - v_A) \tag{3.7}$$

$$\overline{RV} = \frac{2}{3R}\left(\frac{v_A + v_C}{2} - v_B\right) - \frac{1}{\sqrt{3}R}(u_C - u_A). \tag{3.8}$$

It can be shown that estimates of $\overline{HD}$ and $\overline{RV}$ using Stokes' and Gauss' theorems will arrive at the same result as above.

Estimated time series of $\overline{HD}$ and $\overline{RV}$ are stationary using the "run test" method (Bendat and Piersol, 1971). The run test for the standard deviation of $\overline{HD}$ is illustrated in Figure 7. To test the stationarity, the time series of $\overline{HD}$ is first divided into 11 segments with a length of 1024 ($= 2^{10}$) points. Standard deviations of 11 segments fluctuate around the median standard deviation. Since there are five runs about the median value in the sequence, the hypothesis of stationarity is accepted at the 95% level of significance. Similar analysis for $\overline{HD}$ at other levels and for $\overline{RV}$ have been made. They are all accepted as a stationary process.

3.3 Spectral Analysis of $\overline{HD}$ and $\overline{RV}$

In this section, spectral analysis of $\overline{HD}$ and $\overline{RV}$ will be discussed. Time series of $\overline{HD}$ and $\overline{RV}$ at each level are first divided into segments with a length of 1024 ($= 2^{10}$) data points. Successive segments are 50% overlapped. Each segment is subjected to a Hanning window and fast Fourier transformed. One-sided frequency spectra are obtained using estimated Fourier coefficients and are averaged over all segments. The averaged spectra of HD and RV at each level are furthermore averaged over

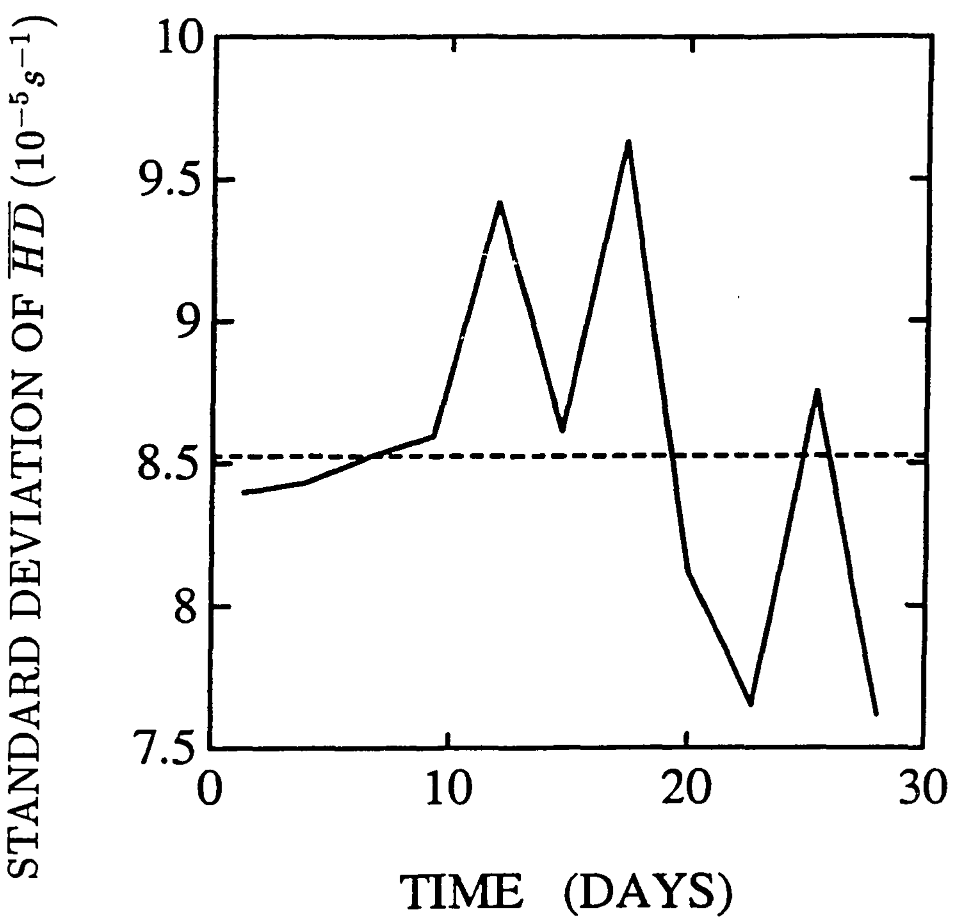

Figure 7: Run test for stationarity of $\overline{HD}$ at level 6. Time series of $\overline{HD}$ at level 6 is divided into 11 segments with a length of 2^{10} points. Sample standard deviation of each segment is computed as shown in the solid line. The dash line denotes the median value of sample standard deviations.

adjacent frequencies to yield estimates at 40 frequency bands spaced about equally on a logarithmic scale.

Measurement errors on estimates of $\overline{HD}$ and $\overline{RV}$ have been discussed by Müller et al. (1988). The systematic error is unlikely to be significant. Part of the observed variance may be due to incoherent current fluctuations with horizontal scales smaller than the smallest current meter separation (8.5 m at level 2). Horizontal velocity components at level 2 are decomposed into the coherent "signal" component and the incoherent "noise" component, with respect to a horizontal scale of 8.5 m. The "signal" component of horizontal kinetic energy is dominant in the whole frequency domain with a –2 spectral slope in the internal wave frequency band and a –3 slope beyond the buoyancy frequency (Figure 8). The "noise" component does not play a significant role in the velocity spectrum.

The contribution of frequency spectral estimates of $\overline{HD}$ and $\overline{RV}$ due to the incoherent "noise" component can be obtained using eqs. 3.7 and 3.8 as

$$\delta S_{\overline{HD}}(\omega) = \delta S_{\overline{RV}}(\omega) = \frac{4}{3R^2}\delta S_u(\omega), \tag{3.9}$$

where $\delta S_u(\omega)$ is the kinetic energy frequency spectrum of the incoherent noise component. At level 2, the frequency spectral estimate $S_{\overline{RV}}(\omega)$ is of the same order as the incoherent noise component in the internal wave frequency band (Figure 9). The frequency spectral estimate of $\overline{HD}$ at level 2 is also comparable to the noise component. At deeper levels, spectra $S_{\overline{HD}}$ and $S_{\overline{RV}}$ are much stronger than incoherent noise components (Figure 10). In further discussion, incoherent noise components $\frac{4}{3R^2}\delta S_u(\omega)$ are removed from $S_{\overline{HD}}$ and $S_{\overline{RV}}$ at levels 5, 6, 10, and 14. Spectral estimates of $\overline{HD}$ and $\overline{RV}$ at level 2 will not be used since they are strongly contaminated by the incoherent noise.

Frequency spectra $S_{\overline{HD}}$ and $S_{\overline{RV}}$ at levels 5, 6, 10 and 14 decrease systematically

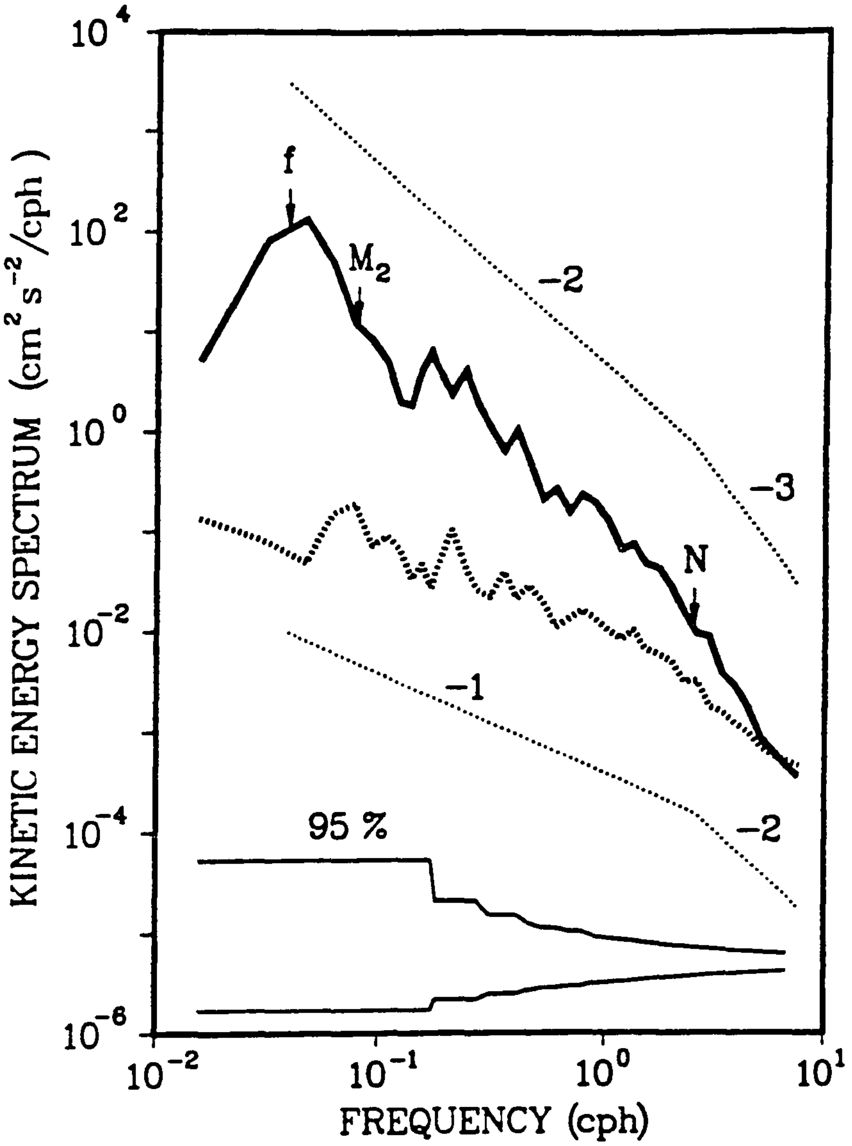

Figure 8: Signal (the solid line) and noise (the dotted line) components of the averaged kinetic energy spectrum at level 2. The "signal" represents the current fluctuations which are coherent among three current meters. The "noise" represents the incoherent component.

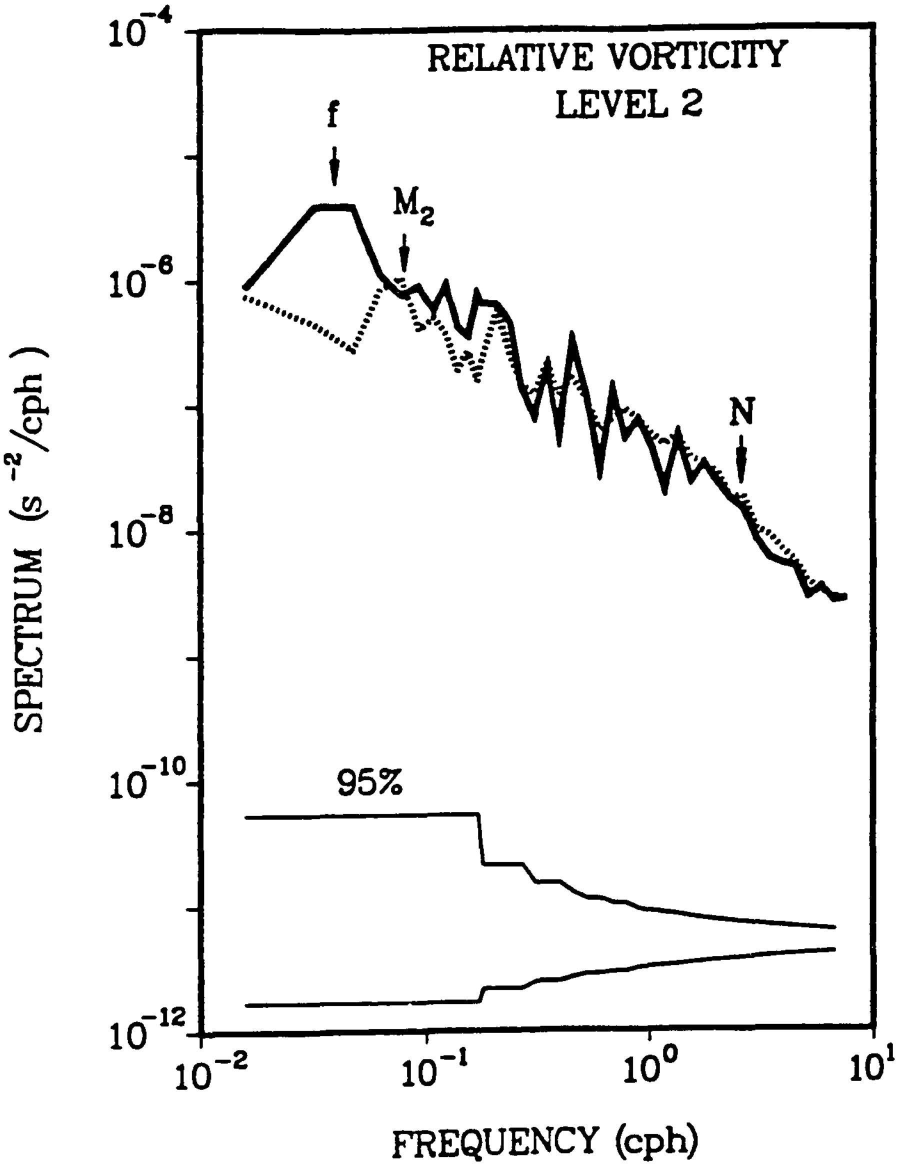

Figure 9: Estimated frequency spectrum of relative vorticity (the solid line) compared with the current noise component (the dotted line) at the level 2 of IWEX.

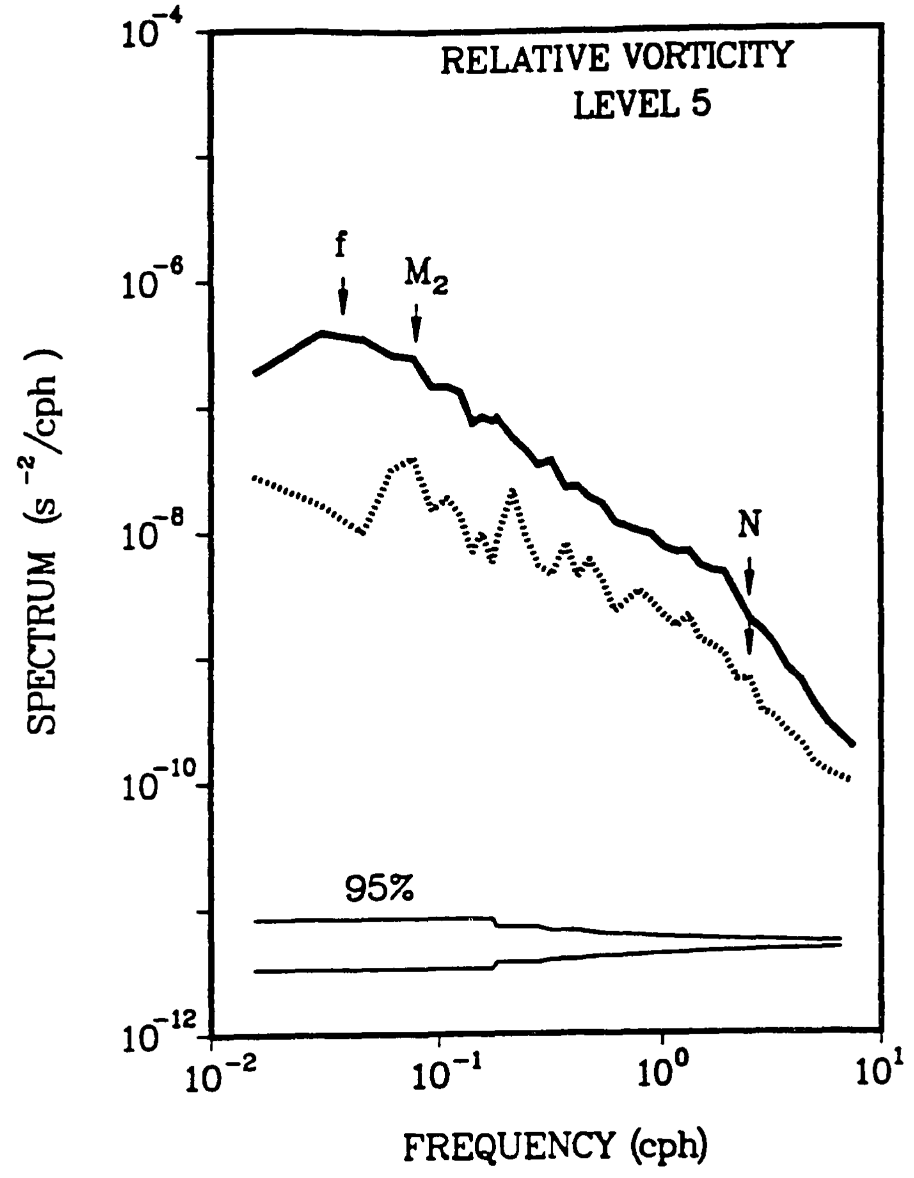

Figure 10: Estimated frequency spectrum of relative vorticity (the solid line) compared with the current noise component (the dotted line) at level 5 of IWEX.

with increasing depth (Figures 11 and 12). In other words, they decrease with the increase of averaged area. For most frequencies, the sum of spectra of $\overline{HD}$ and $\overline{RV}$ can be well represented by a power law of the radius of the circle, i.e.,

$$S_{\overline{HD}}(\omega; R) + S_{\overline{RV}}(\omega; R) \sim R^{-q(\omega)}, \tag{3.10}$$

where $q(\omega)$ is the slope. In the common internal wave frequency band of all four levels, the mean slope is about 1.6 (Figure 13). Beyond the internal wave frequency band, the slope is slightly steeper and the corresponding 95% confidence interval is relatively larger. Frequency spectral slopes of $S_{\overline{HD}}(\omega)$ and $S_{\overline{RV}}(\omega)$ are about $-2/3$ in the internal wave frequency band, and -2 beyond the Brunt–Väisälä frequency.

For linear internal waves, the consistency relation exist between frequency spectra of relative vorticity and horizontal divergence, i.e.,

$$\frac{S_{RV}^{(IW)}(\omega)}{S_{HD}^{(IW)}(\omega)} = \frac{f^2}{\omega^2}. \tag{3.11}$$

Here, the superscript (IW) denotes the linear internal wave. The consistency test of spectral estimates $S_{\overline{RV}}(\omega)$ and $S_{\overline{HD}}(\omega)$ at level 5 with the linear internal wave theory is displayed in Figure 14. Apparently, linear internal wave theory can not explain frequency spectral estimates of $\overline{HD}$ and $\overline{RV}$. In fact, these two spectral estimates are of the same order for all four levels.

The observed discrepancies in the consistency test could be either due to the failure of the linear internal wave theory to explain fluctuations of horizontal divergence and of relative vorticity or simply imply a need of further interpretation of frequency spectral estimates $S_{\overline{HD}}(\omega; R)$ and $S_{\overline{RV}}(\omega; R)$.

Indeed, frequency spectral estimates $S_{\overline{HD}}$ and $S_{\overline{RV}}$, based on three velocity measurements separated by a finite distance on a circle at each horizontal plane, do not

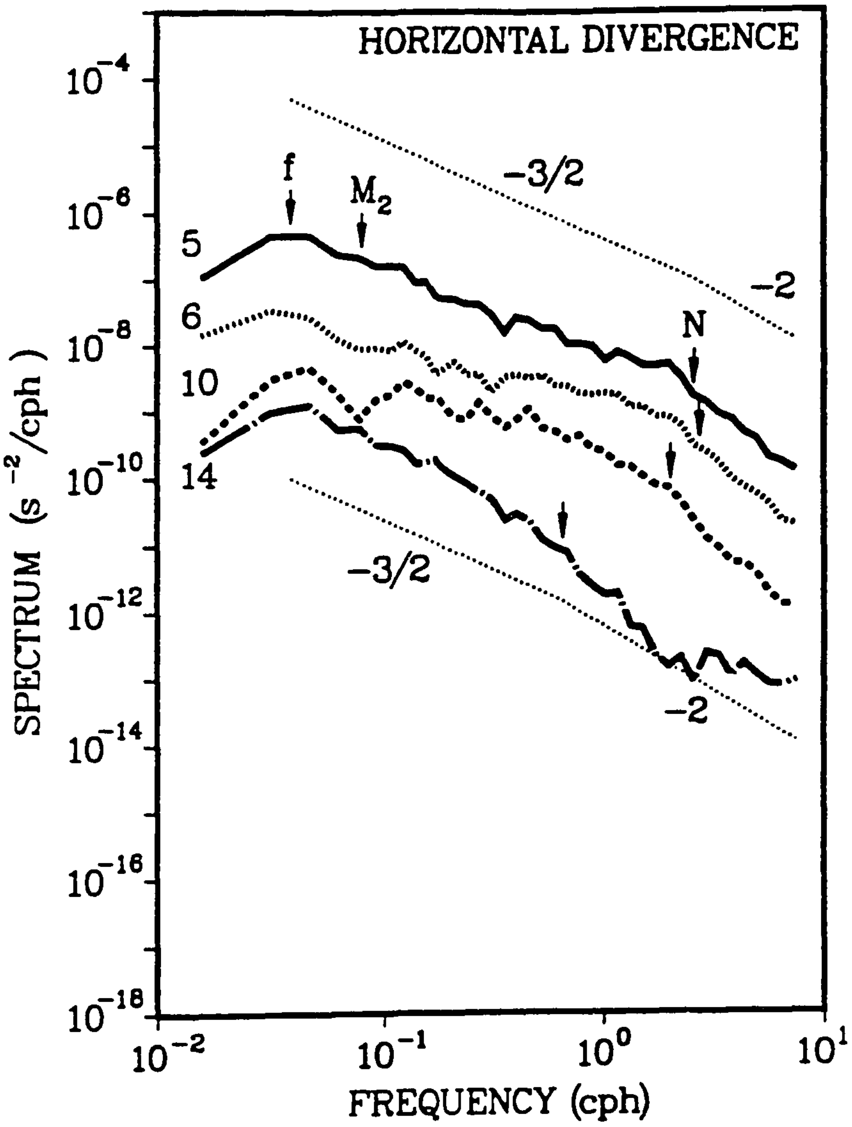

Figure 11: Frequency spectra of horizontal divergence at four levels. f, M_2, and N denote inertial, semidiurnal tidal, and Brunt–Väisälä frequencies.

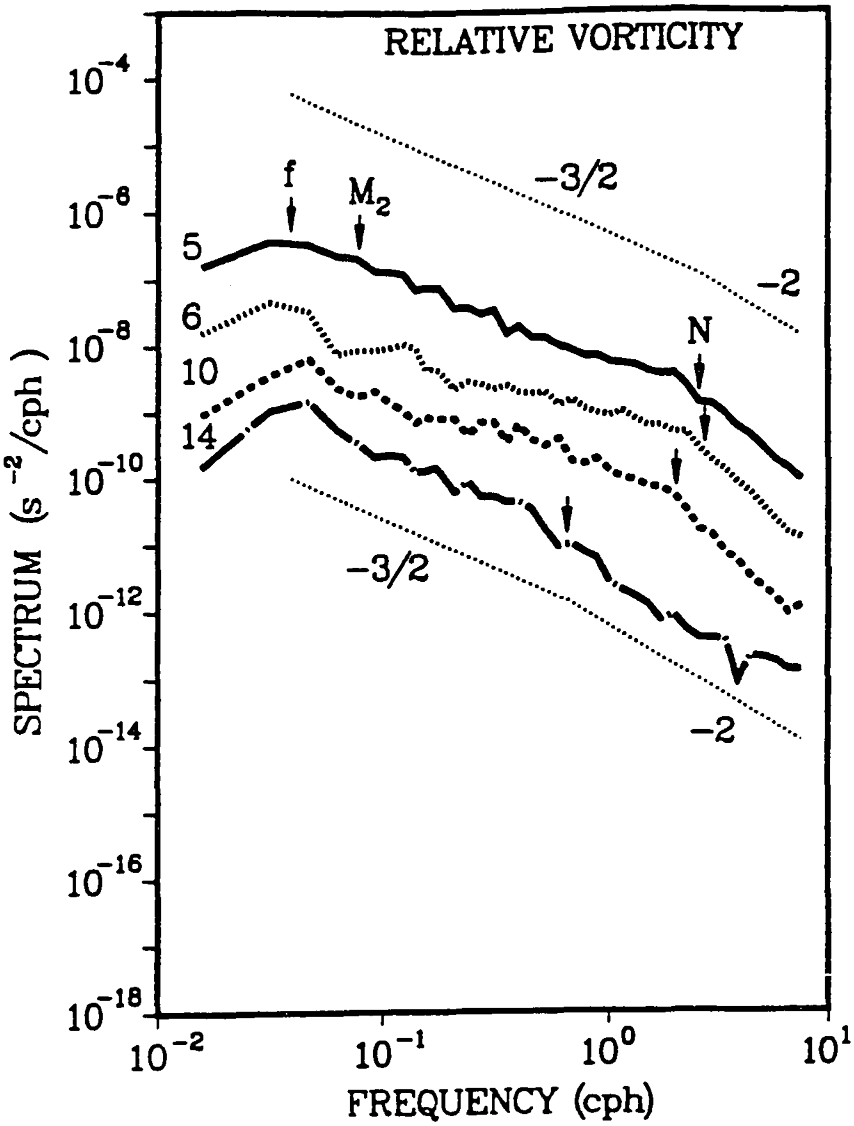

Figure 12: Frequency spectra of relative vorticity at four levels.

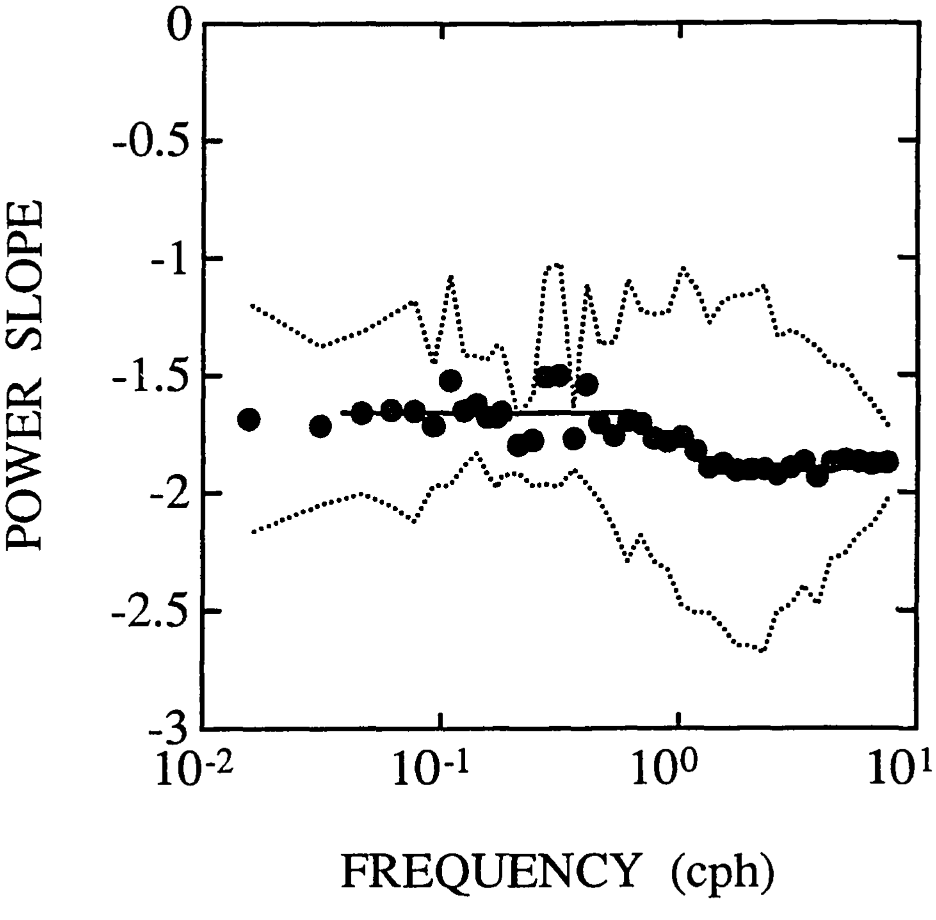

Figure 13: Sum of frequency spectral estimates $S_{\overline{HD}}$ and $S_{\overline{RV}}$ as power law of the radius of the circle. Solid circles denote the estimated powers at 40 frequency points. Dotted lines represent their 95% confidence intervals. The solid line in the internal wave frequency band shows the mean slope.

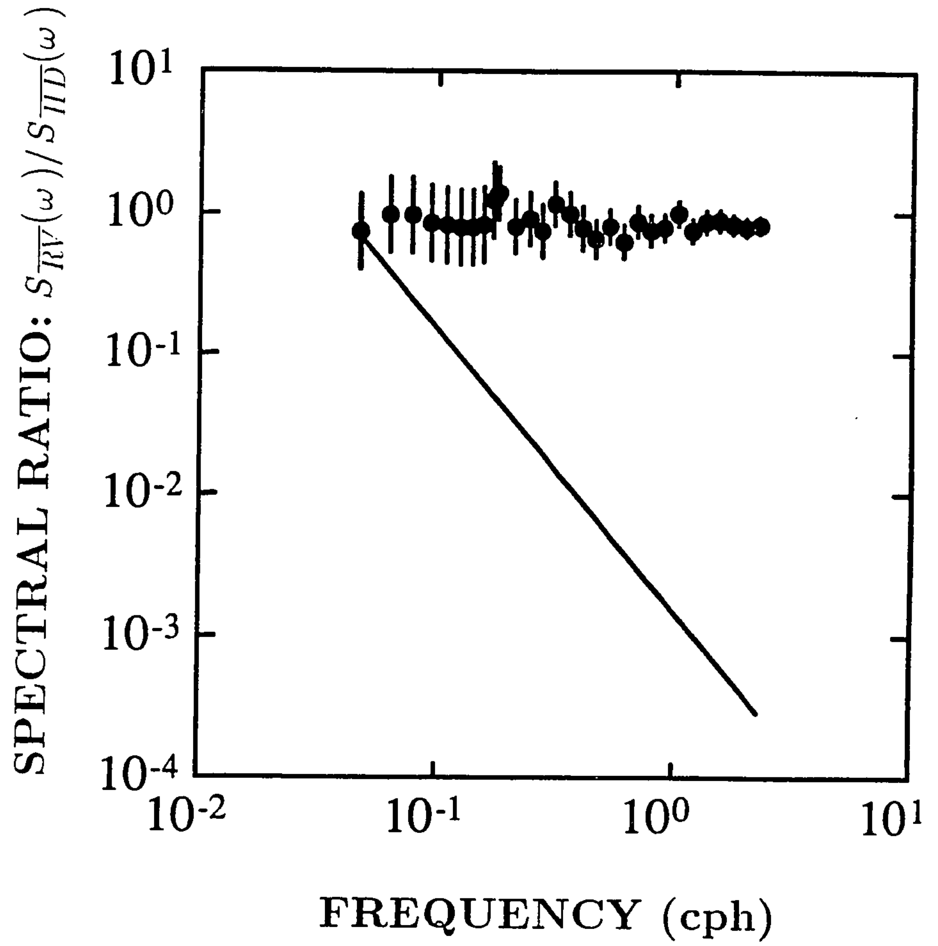

Figure 14: Consistency test of linear internal waves at level 5 of IWEX. Solid circles are estimated ratio of frequency spectra of $\overline{RV}$ and $\overline{HD}$. Vertical bars are 95% confidence intervals. The solid line represents the consistency relation of linear internal waves.

represent area averaged frequency spectra of horizontal divergence and relative vorticity exactly. Assuming a horizontally isotropic flow field, frequency spectral estimates $S_{\overline{HD}}$ and $S_{\overline{RV}}$ can be expressed as

$$S_{\overline{HD}}(\omega; R) = \int_0^{\infty} d\alpha \, \{S_{HD}(\alpha, \omega)F(\alpha R) + S_{RV}(\alpha, \omega)G(\alpha R)\} \tag{3.12}$$

$$S_{\overline{RV}}(\omega; R) = \int_0^{\infty} d\alpha \, \{S_{RV}(\alpha, \omega)F(\alpha R) + S_{HD}(\alpha, \omega)G(\alpha R)\} \, . \tag{3.13}$$

$S_{HD}(\alpha, \omega)$ and $S_{RV}(\alpha, \omega)$ are horizontal wavenumber–frequency spectra of HD and RV in a horizontally isotropic flow field. $F(\alpha R)$ is a lowpass array response function in the horizontal wavenumber domain with a slope of –2 beyond the rolling-off wavenumber ($\alpha R \approx 1$), and $G(\alpha R)$ is a bandpass array response function (Figure 15). Detailed derivations of these two array response functions for the IWEX current meter configuration are discussed in Appendix A. The lowpass array response function $F(\alpha R)$ represents the problem of the finite separation among current meters such that variations at scales smaller than the scale of the circle are attenuated. The bandpass array response function $G(\alpha R)$ represents the contamination problem due to the discrete velocity measurements on the circle such that estimated $\overline{RV}$ and $\overline{HD}$ are contaminated by each other. Hereafter, F is termed the attenuation array response function since it describes the attenuation of small–scale fluctuations, and G is termed the contamination array response function since it represents the potential contamination errors.

A more general discussion for an arbitrary number of current meters located evenly on a circle is described in Appendix B. Increasing the number of velocity sensors along the circle does not change the attenuation array response function significantly since it is a result of the finite size of the circle only. The contamination array response function is reduced and its peak moves to a higher horizontal wavenumber by increasing velocity measurements along the circle. In principle, the contamination problem can be eliminated using continuous velocity measurements along the circle since its peak will vanish and move to an infinite horizontal wavenumber. The attenuation array response function can also be eliminated to a limit of infinitesimal radius of the circle.

Specifically, the attenuation and contamination array response functions for the IWEX trimooring configuration have the forms

$$F(\alpha R) = \frac{2}{3\alpha^2 R^2}\left[1 - J_0(\sqrt{3}\,\alpha R\,) + 2J_2(\sqrt{3}\,\alpha R\,)\right] \tag{3.14}$$

$$G(\alpha R) = \frac{2}{3\alpha^2 R^2}\left[1 - J_0(\sqrt{3}\,\alpha R\,) - 2J_2(\sqrt{3}\,\alpha R\,)\right]. \tag{3.15}$$

Here, J_0 and J_2 are Bessel functions of the first kind of zeroth and second order, respectively. Obviously, the previously observed consistency discrepancy does not necessarily imply a failure of the linear internal wave theory. To test the linear internal wave theory, estimates of uncontaminated frequency spectra of horizontal divergence and relative vorticity are required. Note that with the effect of the attenuation problem alone, the linear internal wave theory will still predict a ratio between frequency spectra of HD and RV to be $\frac{f^2}{\omega^2}$.

3.3.1 Comparison with GM–76 Internal Wave Spectrum

Compiling observations from various sources and different locations in the time–space scales of oceanic internal waves, Garrett and Munk (1972) constructed an empirical energy spectrum (referred to as the GM–72 spectrum). This spectrum has

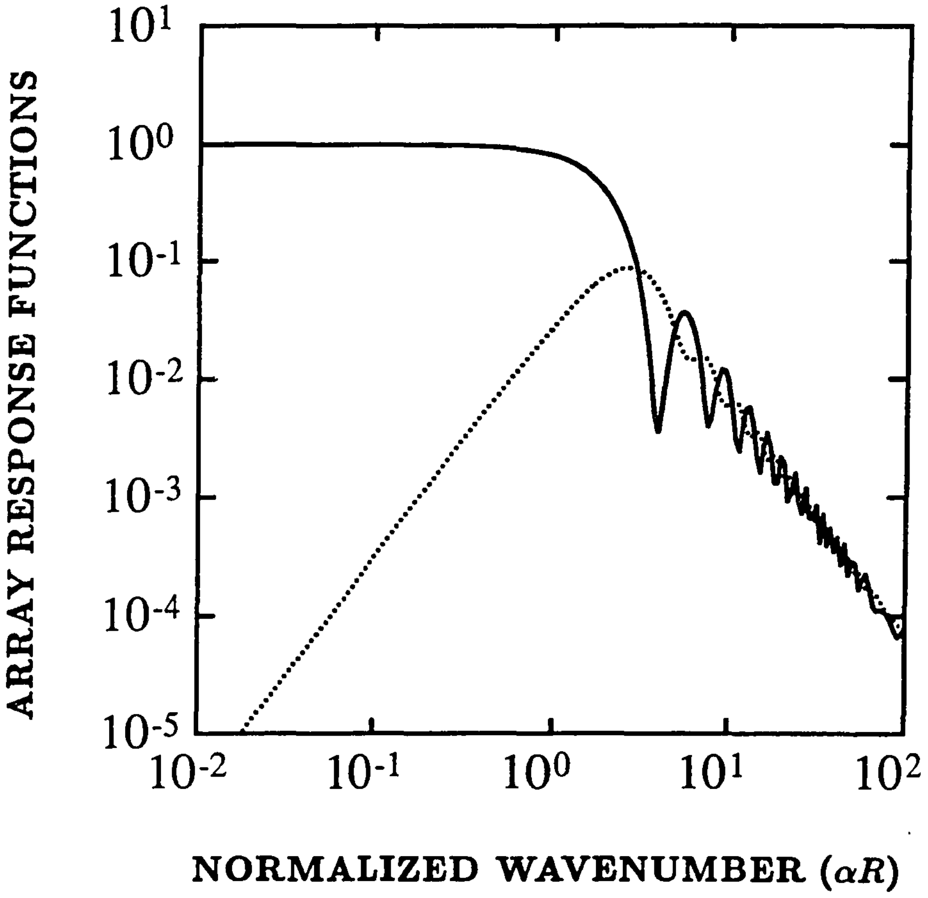

Figure 15: Array response functions for frequency spectra $S_{\overline{HD}}$ and $S_{\overline{RV}}$. The thick solid line represents the attenuation array response function F, and the thin solid line the contamination array response function G.

been considered as a representation of internal waves in the absence of local sources or sinks of energy.

Modifications of the GM–72 spectrum have been made as a result of improvements in oceanic instrumentation and advances in theoretical studies. In our discussion, the GM–76 spectrum (Cairns and Williams, 1976) will be used. It is briefly reviewed in Appendix C.

Using the GM-76 spectrum model and the polarization relation of internal waves, GM frequency spectra of $\overline{HD}$, $\overline{RV}$ are obtained at different levels of IWEX applying the wavenumber filter functions F and G. A vertical cutoff wavenumber of 0.1 cpm has been assigned as the upper boundary of the GM spectrum in the vertical wavenumber space.

Frequency spectra of $\overline{HD}$ at four levels are compared with the corresponding GM–76 spectra (Figures 16 – 19). Both spectral levels and slopes are consistent with the GM spectra at levels 6, 10 and 14. At level 5, the observed frequency spectrum of $\overline{HD}$ is stronger than the GM spectrum, especially near the inertial frequency (Figure 16). One possible reason for this disagreement is due to the prescribed vertical cutoff wavenumber in the GM spectrum. Figure 20 displays the variance preserving contours of HD spectrum of the GM model. Most of variance of horizontal divergence of the GM model is concentrated at high wavenumbers. At level 5, most of variance of HD near the inertial frequency is lost due to the vertical cutoff wavenumber effect. At deeper levels, the effect of vertical cutoff wavenumber does not play a significant role, whereas the attenuation array response function is effective. In fact, if we increase the vertical cutoff wavenumber used in the GM spectrum to 1 cpm, the energy level of the GM spectrum will be much closer to observed frequency spectrum.

Frequency spectra of $\overline{RV}$ at four levels are compared with the corresponding GM–76 spectra (Figures 21 – 24). At level 5, the observed spectrum is about one

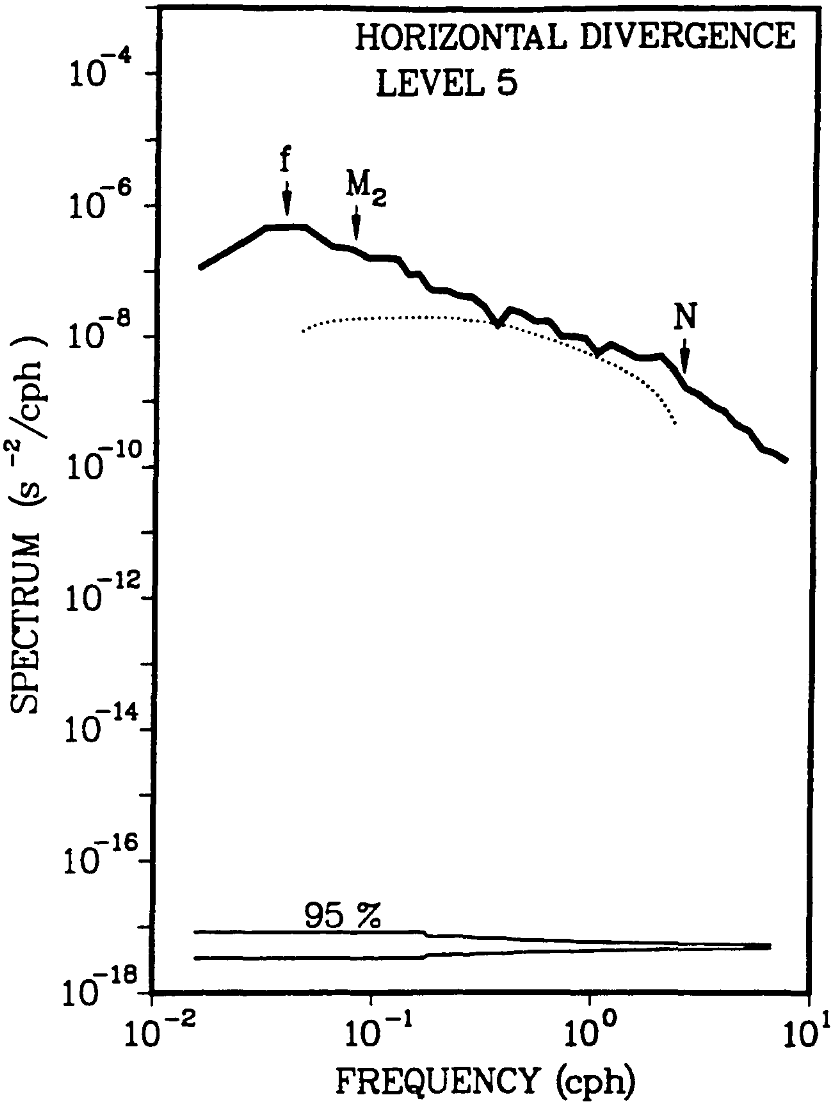

Figure 16: Frequency spectrum of estimated horizontal divergence (solid line) at level 5 compared with the GM spectrum (dotted line) applying the attenuation and contamination array response functions. The 95% confidence level is shown.

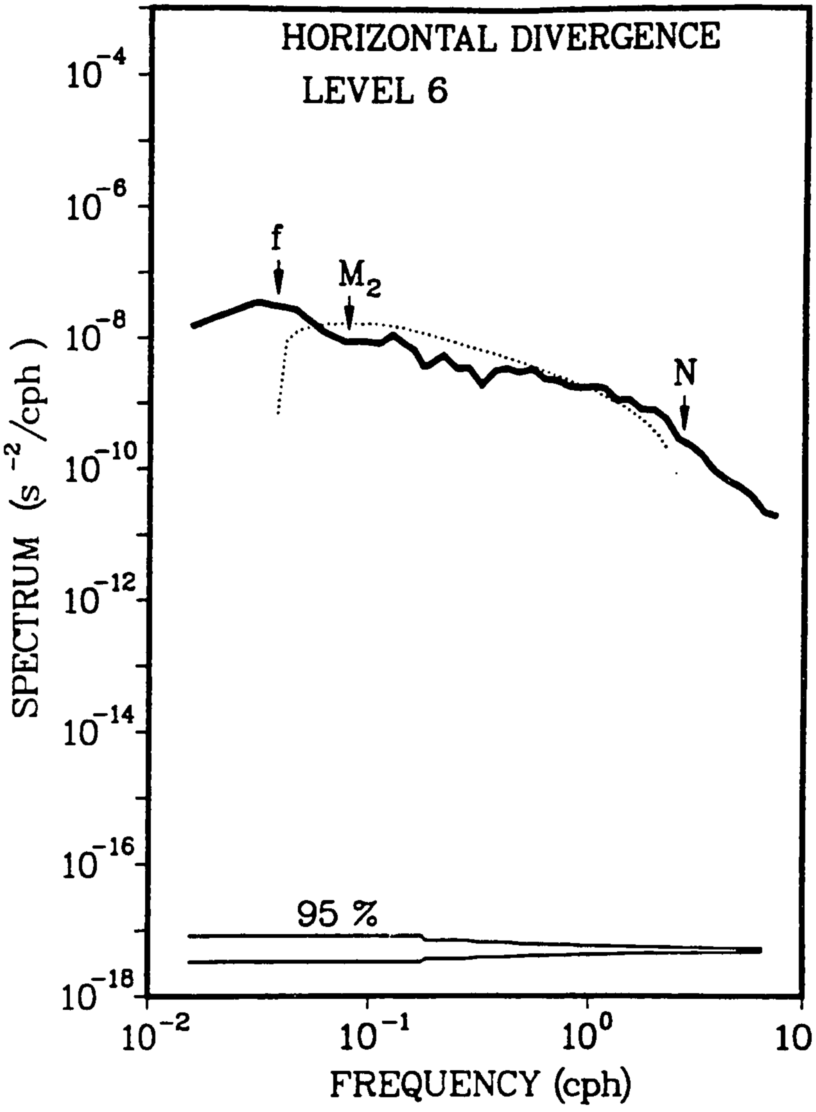

Figure 17: Frequency spectrum of estimated horizontal divergence (solid line) at level 6 compared with the GM spectrum (dotted line) applying the attenuation and contamination array response functions. The 95% confidence level is shown.

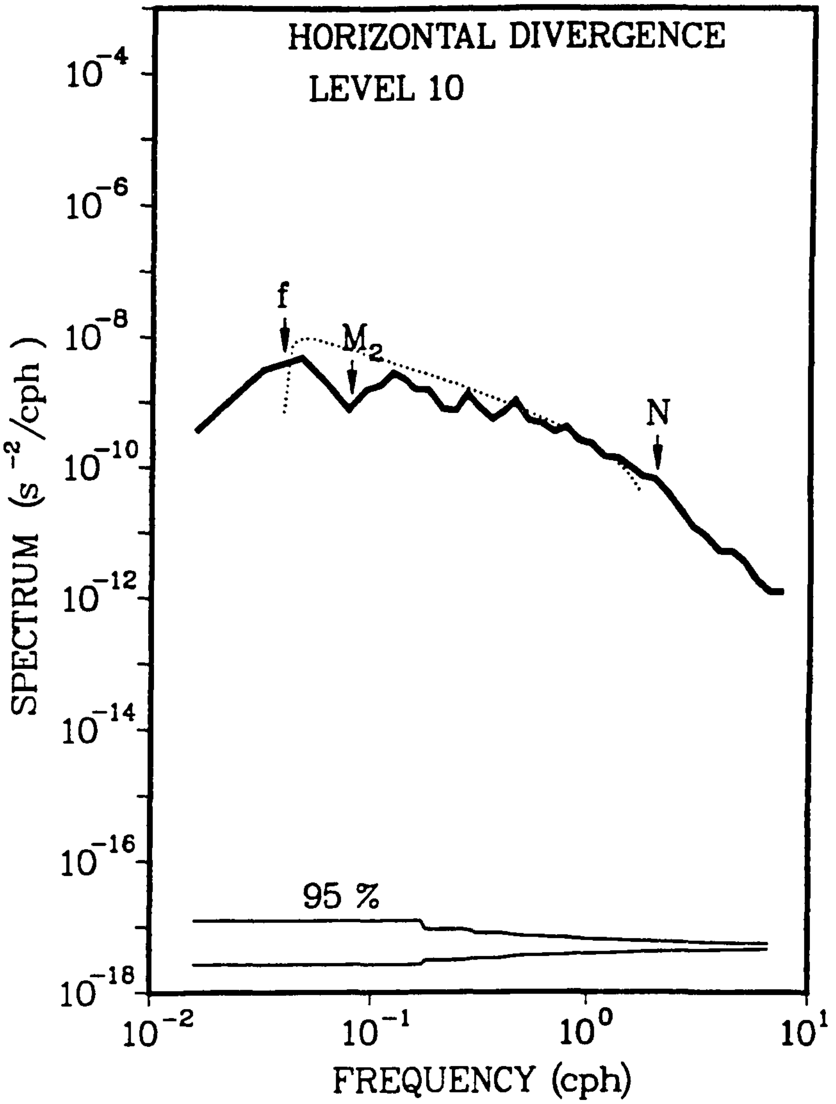

Figure 18: Frequency spectrum of estimated horizontal divergence (solid line) at level 10 compared with the GM spectrum (dotted line) applying the attenuation and contamination array response functions. The 95% confidence level is shown.

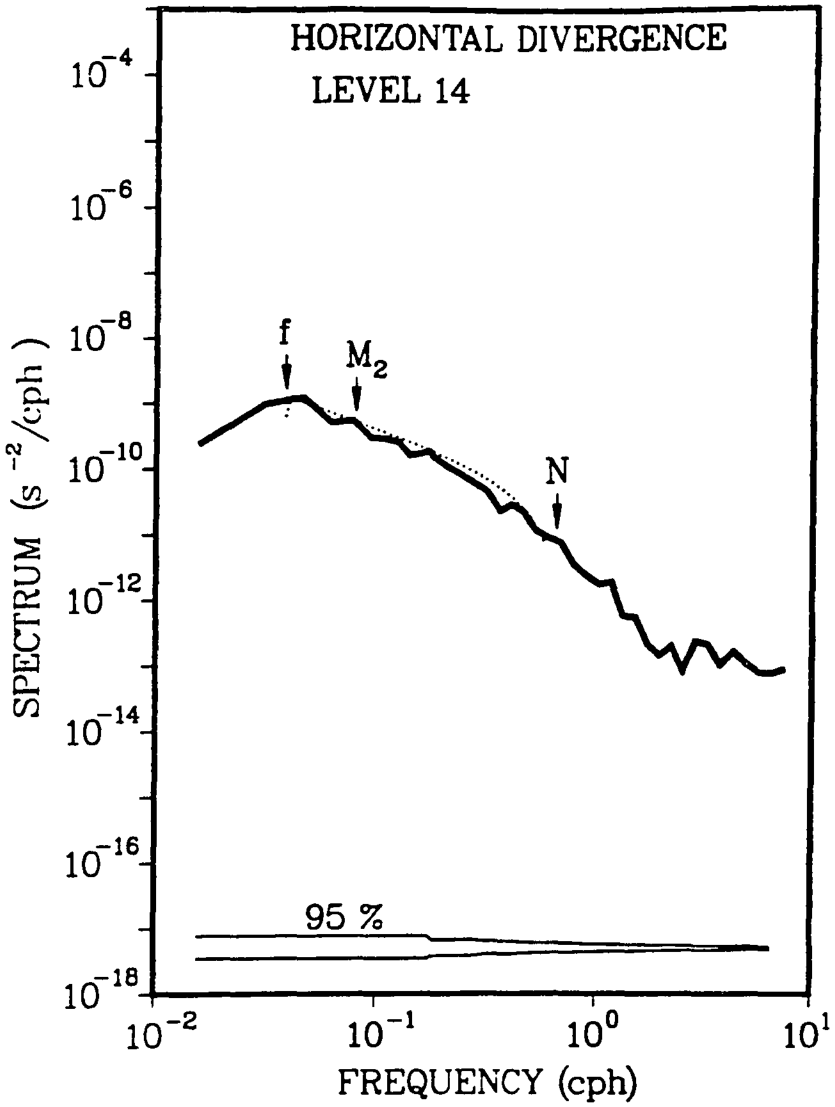

Figure 19: Frequency spectrum of estimated horizontal divergence (solid line) at level 14 compared with the GM spectrum (dotted line) applying the attenuation and contamination array response functions. The 95% confidence level is shown.

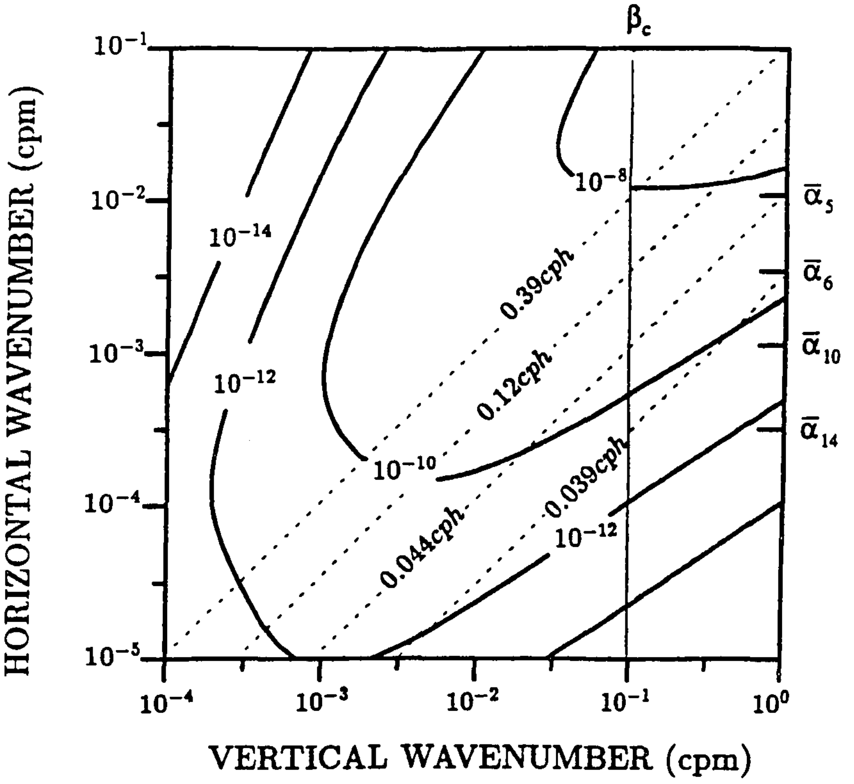

Figure 20: Variance preserving contour of horizontal divergence of GM–76 spectrum. $\beta_c = 10^{-1}$ cpm is the vertical cutoff wavenumber for the GM spectrum. $\overline{\alpha} = \int_0^\infty d\alpha F(\alpha R)$ represents the rolling-off wavenumber of the attenuation array response function. Dashed lines show constant frequencies of linear internal waves.

order greater than the GM–76 spectrum, and is about a factor of four greater than the GM–76 spectrum at level 6. At levels 10 and 14, observed spectral estimates of $\overline{RV}$ agree very well with the GM spectra. Discrepancies at levels 5 and 6 could be either due to the failure of the linear internal wave theory to explain small–scale fluctuations of HD and RV or to the inadequacy of the GM–76 spectrum at small horizontal scales. GM–76 spectrum model is not appropriate to make a conclusion. An exact justification requires either uncontaminated frequency spectra of horizontal divergence and relative vorticity or a more accurate wavenumber structure of the internal wave field.

3.3.2 Inverse Transformation of $S_{HD}(\alpha, \omega)$ and $S_{RV}(\alpha, \omega)$

Frequency spectral estimates $S_{\overline{HD}}(\omega; R)$ and $S_{\overline{RV}}(\omega; R)$ can be expressed as horizontal wavenumber integration of $S_{HD}(\alpha, \omega)$ and $S_{RV}(\alpha, \omega)$ applying the attenuation and contamination array response functions (eqs. 3.12 and 3.13). The inverse transformation of $S_{HD}(\alpha, \omega)$ and $S_{RV}(\alpha, \omega)$ is difficult to obtain since two integration kernels are involved. However, the sum and the difference of $S_{\overline{HD}}(\omega; R)$ and $S_{\overline{RV}}(\omega; R)$ can be expressed as the horizontal wavenumber integration of the sum and the difference of $S_{HD}(\alpha, \omega)$ and $S_{RV}(\alpha, \omega)$ applying one integration kernel only, i.e.,

$$S_{\overline{HD}}(\omega; R) + S_{\overline{RV}}(\omega; R) = \int_0^\infty d\alpha \left[S_{HD}(\alpha, \omega) + S_{RV}(\alpha, \omega)\right] F_+(\alpha R) \tag{3.16}$$

$$S_{\overline{HD}}(\omega; R) - S_{\overline{RV}}(\omega; R) = \int_0^\infty d\alpha \left[S_{HD}(\alpha, \omega) - S_{RV}(\alpha, \omega)\right] F_-(\alpha R) \tag{3.17}$$

$$F_+(\alpha R) = F(\alpha R) + G(\alpha R) = \frac{4}{3\alpha^2 R^2}\left[1 - J_0(\sqrt{3}\alpha R)\right] \tag{3.18}$$

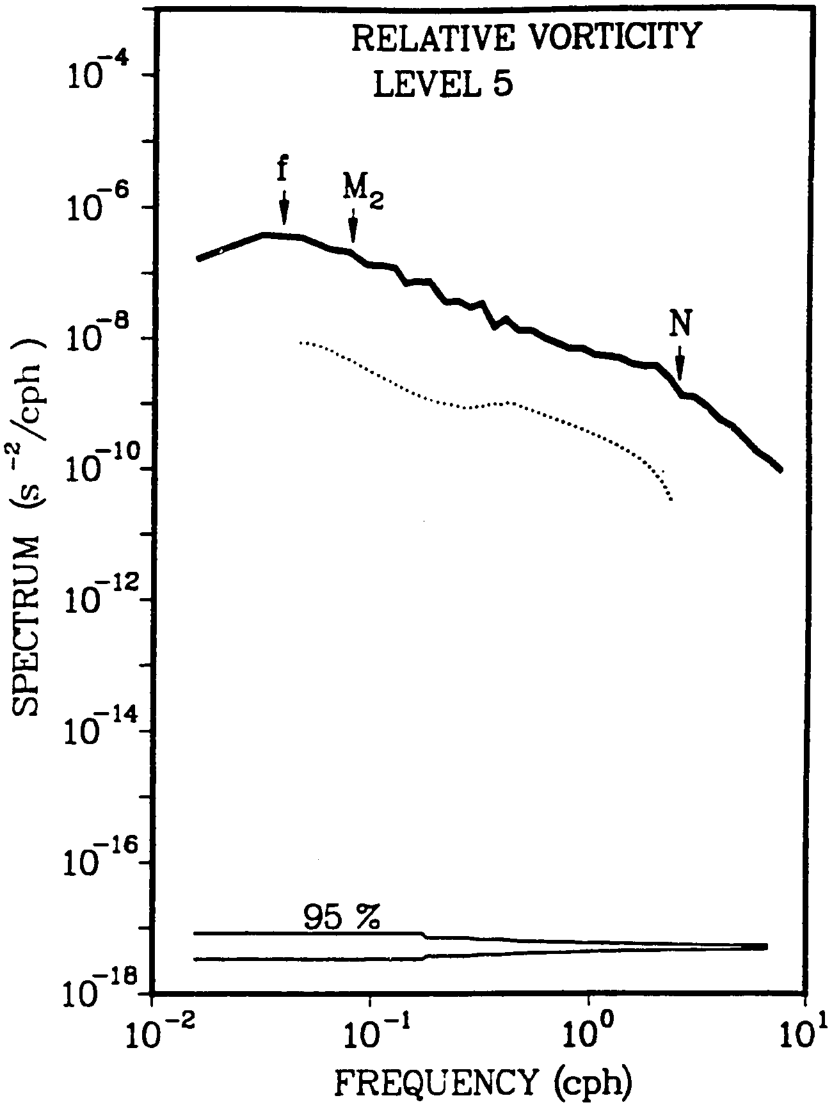

Figure 21: Frequency spectrum of estimated relative vorticity (solid line) at level 5 compared with the GM spectrum (dotted line) applying the attenuation and contamination array response functions. The 95% confidence level is shown.

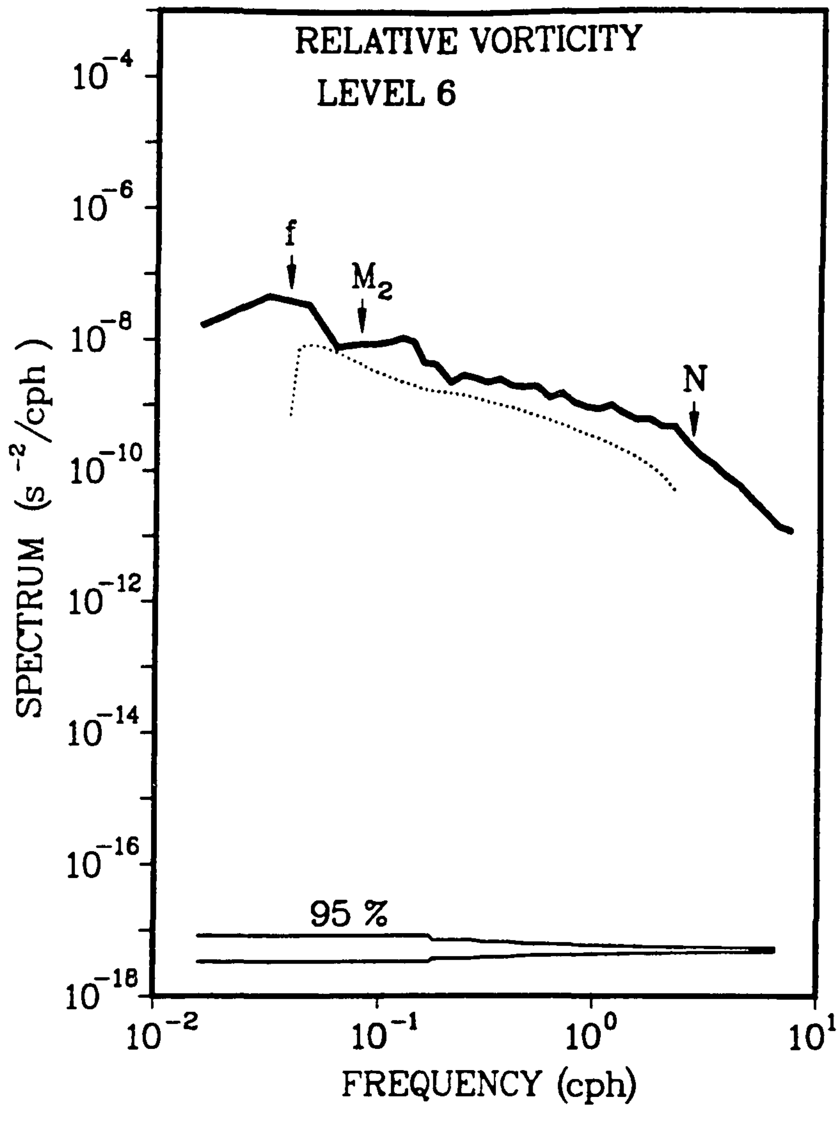

Figure 22: Frequency spectrum of estimated relative vorticity (solid line) at level 6 compared with the GM spectrum (dotted line) applying the attenuation and contamination array response functions. The 95% confidence level is shown.

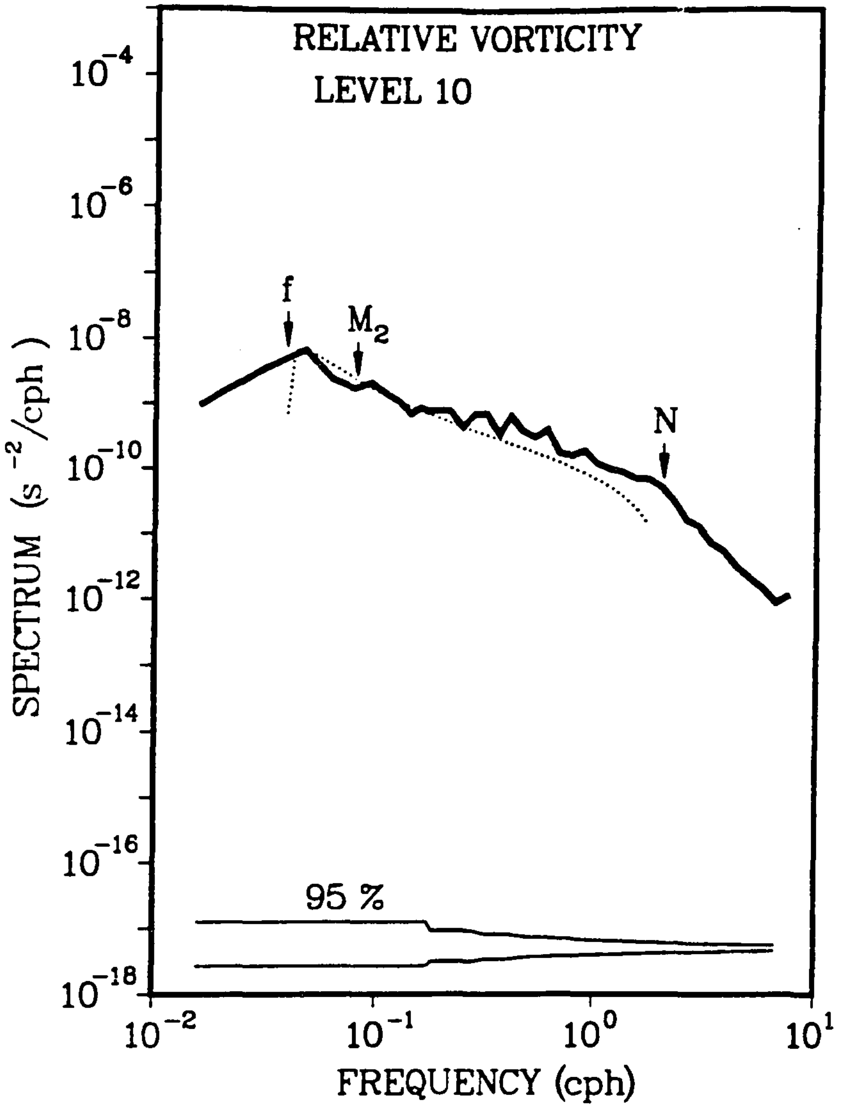

Figure 23: Frequency spectrum of estimated relative vorticity (solid line) at level 10 compared with the GM spectrum (dotted line) applying the attenuation and contamination array response functions. The 95% confidence level is shown.

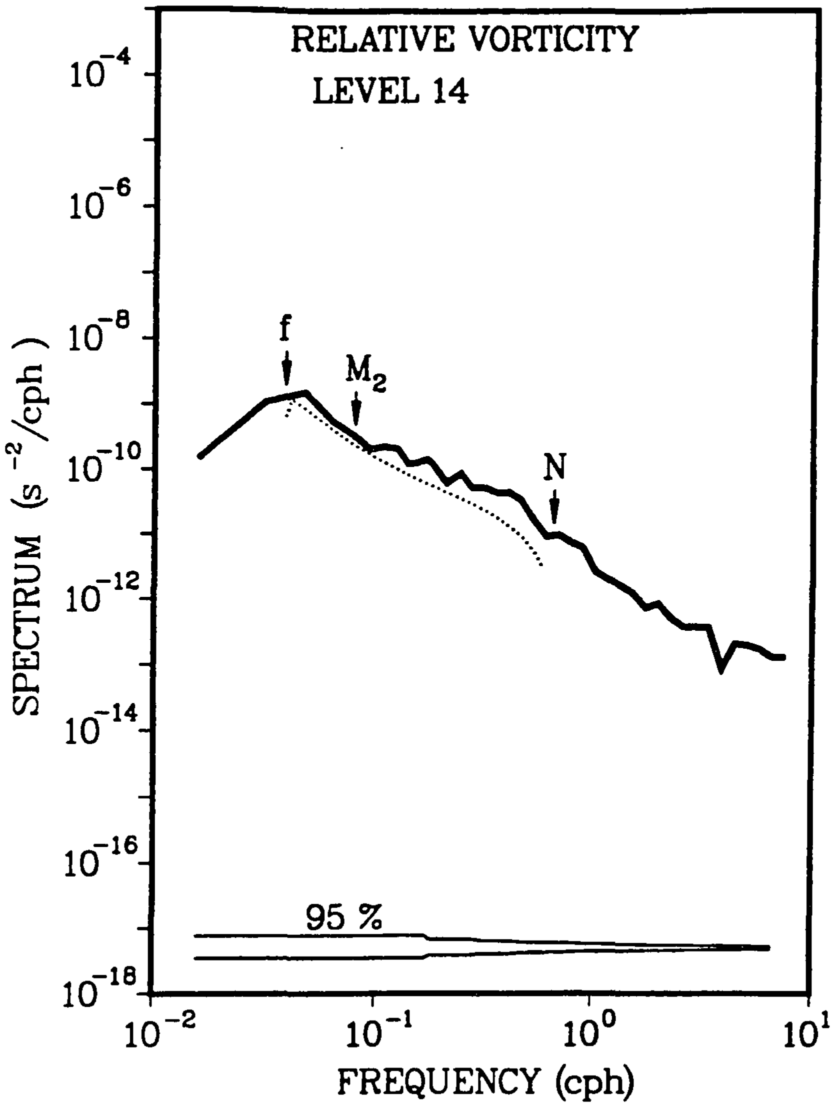

Figure 24: Frequency spectrum of estimated relative vorticity (solid line) at level 14 compared with the GM spectrum (dotted line) applying the attenuation and contamination array response functions. The 95% confidence level is shown.

$$F_{-}(\alpha R) = F(\alpha R) - G(\alpha R) = \frac{8}{3\alpha^2 R^2} J_2(\sqrt{3}\alpha R). \tag{3.19}$$

Here, $F_{+}(\alpha R)$ and $F_{-}(\alpha R)$ both behave as attenuation array response functions with slightly different shapes. The inverse transformation of $S_{HD}(\alpha,\omega) - S_{RV}(\alpha,\omega)$ can be easily obtained. Substituting $F_{-}(\alpha R)$ into eq. 3.17, it can be rewritten as

$$\left\{\frac{3R^2}{8}\left[S_{\overline{HD}}(\omega;R) - S_{\overline{RV}}(\omega;R)\right]\right\} = \int_0^\infty d\alpha \left\{\frac{S_{HD}(\alpha,\omega) - S_{RV}(\alpha,\omega)}{\alpha^3}\right\} \alpha J_2(\sqrt{3}\alpha R). \tag{3.20}$$

Therefore, the term in the bracket on the left–hand side of the equation is the Hankel transformation (of the second order) of the term in the bracket on the right–hand side. Applying the inverse of the Hankel transformation, the difference of wavenumber–frequency spectra of HD and RV can be found as

$$S_{HD}(\alpha,\omega) - S_{RV}(\alpha,\omega) = \int_0^\infty dR \left[S_{\overline{HD}}(\omega;R) - S_{\overline{RV}}(\omega;R)\right] \frac{9\alpha^3 R^3}{8} J_2(\sqrt{3}\alpha R). \tag{3.21}$$

Also, the inverse transformation of $S_{HD}(\alpha,\omega) + S_{RV}(\alpha,\omega)$ can be obtained using the inverse of the Hankel transformation as

$$\begin{aligned} S_{HD}(\alpha,\omega) + S_{RV}(\alpha,\omega) = {} & \left[S_u(\omega) + S_v(\omega)\right] \int_0^\infty dR \left\{3\alpha^3 R_0(\sqrt{3}\alpha R)\right\} \\ & - \int_0^\infty dR \frac{9\alpha^3 R^3}{4} J_0(\sqrt{3}\alpha R) \left\{S_{\overline{HD}}(\omega;R) + S_{\overline{RV}}(\omega;R)\right\} \end{aligned} \tag{3.22}$$

using eqs. 3.16 and 3.19, and the relation

$$S_u(\omega) + S_v(\omega) = \int_0^\infty d\alpha \frac{\left[S_{HD}(\alpha,\omega) + S_{RV}(\alpha,\omega)\right]}{\alpha^2}. \tag{3.23}$$

Here, $S_u(\omega)$ and $S_v(\omega)$ are horizontal velocity frequency spectra. Accordingly, the inverse transformation of $S_{HD}(\alpha,\omega)$ and $S_{RV}(\alpha,\omega)$ can be expressed as

$$\begin{aligned} S_{HD}(\alpha,\omega) = \; & \frac{S_u(\omega)+S_v(\omega)}{2} \int_0^\infty dR \left\{3\alpha^3 R J_0(\sqrt{3}\alpha R)\right\} \\ & + \int_0^\infty dR \frac{9\alpha^3 R^3}{16} \left[J_2(\sqrt{3}\alpha R) - 2J_0(\sqrt{3}\alpha R)\right] S_{\overline{HD}}(\omega; R) \qquad (3.24) \\ & - \int_0^\infty dR \frac{9\alpha^3 R^3}{16} \left[J_2(\sqrt{3}\alpha R) + 2J_0(\sqrt{3}\alpha R)\right] S_{\overline{RV}}(\omega; R) \end{aligned}$$

$$\begin{aligned} S_{RV}(\alpha,\omega) = \; & \frac{S_u(\omega)+S_v(\omega)}{2} \int_0^\infty dR \left\{3\alpha^3 R J_0(\sqrt{3}\alpha R)\right\} \\ & - \int_0^\infty dR \frac{9\alpha^3 R^3}{16} \left[J_2(\sqrt{3}\alpha R) + 2J_0(\sqrt{3}\alpha R)\right] S_{\overline{HD}}(\omega; R) \qquad (3.25) \\ & + \int_0^\infty dR \frac{9\alpha^3 R^3}{16} \left[J_2(\sqrt{3}\alpha R) - 2J_0(\sqrt{3}\alpha R)\right] S_{\overline{RV}}(\omega; R). \end{aligned}$$

The inverse transformation of $S_{HD}(\alpha,\omega)$ and $S_{RV}(\alpha,\omega)$ requires frequency spectral estimates $S_{\overline{HD}}(\omega; R)$ and $S_{\overline{RV}}(\omega; R)$ at continuous radii R. Using IWEX measurements, frequency spectral estimates $S_{\overline{HD}}(\omega; R)$ and $S_{\overline{RV}}(\omega; R)$ could be obtained at five different radii only. Since the convergence of the above inverse transformations is very sensitive to the radius dependence of frequency spectral estimates of $\overline{HD}$ and $\overline{RV}$, these finite points of information are not sufficient to carry out the inverse transformation.

3.3.3 Parameterized Wavenumber Spectrum

As shown in section 3.3.1, the observed frequency spectra of $\overline{HD}$ are well represented by the GM-76 spectrum model, whereas significant discrepancies occur between observed frequency spectra of $\overline{RV}$ and the GM spectrum at levels 5 and 6. We are not able to determine whether such discrepancies are due to the failure of the GM–76 model or due to observed fluctuations which are not internal waves alone. Here, we propose a wavenumber spectrum structure similar to the shape of GM–76 and attempt to determine wavenumber parameters from observed spectra.

Using equations 3.16 and 3.23, the sum of frequency spectral estimates of $\overline{HD}$ and $\overline{RV}$ can be written as

$$S_{\overline{HD}}(\omega, R) + S_{\overline{RV}}(\omega, R) = \int_0^\infty d\alpha \, [S_u(\alpha, \omega) + S_v(\alpha, \omega)] \, \frac{4}{3R^2} \left[1 - J_0(\sqrt{3}\alpha R)\right]. \quad (3.26)$$

A velocity wavenumber spectrum model is proposed such that

$$[S_u(\alpha, \omega) + S_v(\alpha, \omega)] = E_u(\omega) A(\frac{\alpha}{\alpha_*}) \alpha_*^{-1} \quad (3.27)$$

$$A(\frac{\alpha}{\alpha_*}) = (1 + \frac{\alpha}{\alpha_*})^{-p}. \quad (3.28)$$

Here, $E_u(\omega)$ is proportional to the horizontal kinetic frequency spectrum. α_* is the wavenumber bandwidth, and p the high wavenumber slope. Applying this wavenumber spectrum model, the sum of frequency spectral estimates $S_{\overline{HD}}(\omega; R)$ and $S_{\overline{RV}}(\omega; R)$ becomes

$$S_{\overline{HD}}(\omega; R) + S_{\overline{RV}}(\omega; R) = \frac{4E_u(\omega)}{3R^2} \int_0^\infty d\alpha \left[1 - J_0(\sqrt{3}\alpha R)\right] \frac{1}{\alpha_*(1 + \alpha/\alpha_*)^p}. \quad (3.29)$$

The asymptotic form of the above integration can be used to determine the high wavenumber slope. Following Gradshteyn and Ryzhik (1965, eq. 6563), the above integration can be approximated as

$$S_{\overline{HD}}(\omega; R) + S_{\overline{RV}}(\omega; R) \sim R^{-2} \left\{ (\alpha_* R)^{p-1} + O(\alpha_* R)^2 \right\}. \quad (3.30)$$

Furthermore, assuming $\alpha_* R \ll O(1)$ and $1 < p < 3$, the higher order terms in the above equation can be neglected. Note that the prescribed range of high wavenumber slope includes the wavenumber slope 2 of the GM model. Also, the assumption of $\alpha_* R \ll O(1)$ is valid using GM spectrum at shallower levels in the low frequency band (Figure 25). Since $S_{\overline{HD}}(\omega; R) + S_{\overline{RV}}(\omega; R)$ has an approximate $R^{-1.6}$ dependence in the internal wave frequency band (Figure 13), the high wavenumber slope p of the velocity wavenumber spectrum is approximately 1.4 which is slightly smaller than that of the GM model. The high wavenumber spectral slope can also be determined from velocity coherence spectra at different horizontal separations. A consistent result was found.

Accordingly, horizontal wavenumber–frequency spectra of HD and RV have a form of $\frac{\alpha^2}{\alpha_*(1 + \alpha/\alpha_*)^{1.4}}$ assuming they have the same wavenumber structure. Apparently, a horizontal cutoff wavenumber has to exist to assure a finite variance of HD and RV. In the GM spectrum, a horizontal cutoff wavenumber is defined using a vertical cutoff wavenumber of 0.1 cpm (Munk, 1981) and the dispersion relation of linear internal waves. However, the vertical cutoff wavenumber prescribed in the GM model is originated from previously observed vertical shear spectra (Gargett et al., 1981) and temperature vertical gradient spectra (Gregg, 1977) where a change of slope at 0.1 cpm was found. However, such a vertical cutoff wavenumber is purely phenomenological. Also, the GM spectrum model has assumed the separability between the vertical wavenumber spectrum and the frequency spectrum. Nonetheless, it has been recently found that vertical wavenumber–frequency spectra of vertical shear have a frequency dependence which is a function of vertical wavenumber (Sherman and Pinkel, 1990). A decreasing vertical cutoff wavenumber and a narrowing of the wavenumber bandwidth at higher frequencies were also found, which disagree with the GM spectrum model. Apparently, one should be very cautious in using the GM

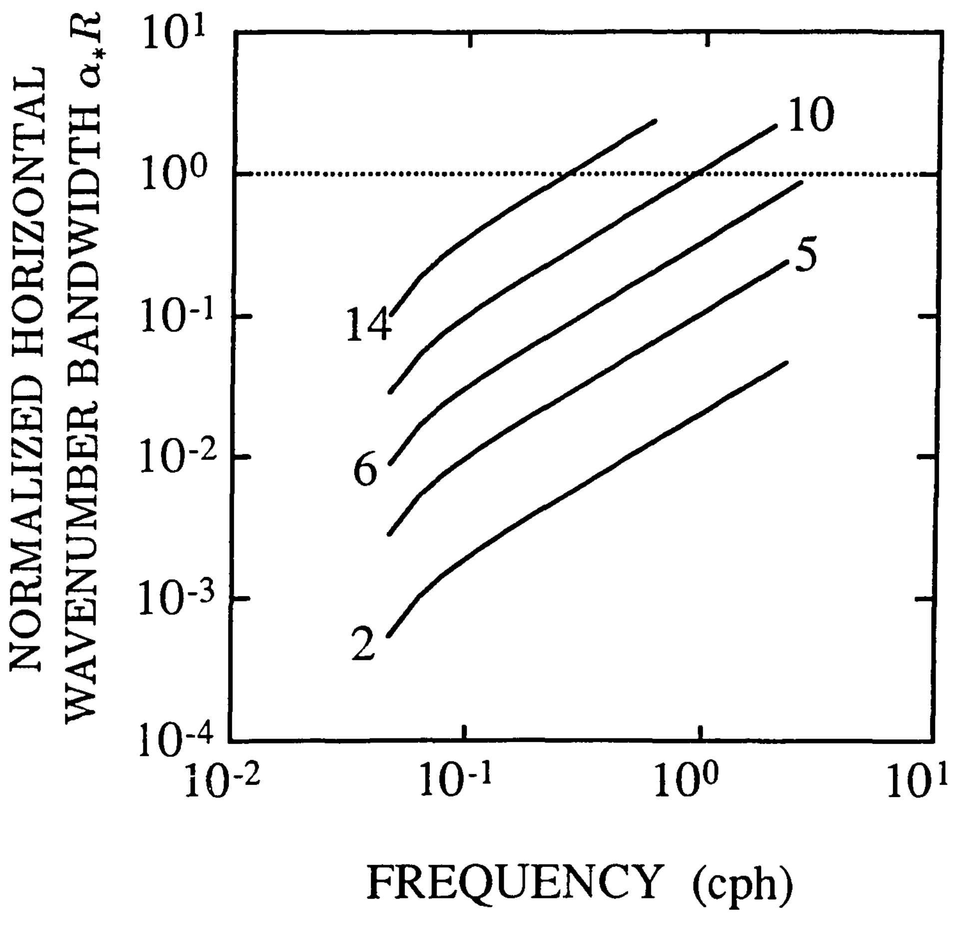

Figure 25: Normalized wavenumber bandwidth ($\alpha_* R$) versus frequency of GM-76 spectrum. The wavenumber bandwidth of the GM model is defined as $\alpha_* = \dfrac{\sqrt{\omega^2 - f^2}\pi j_*}{bN_0}$.

spectrum model. Particularly, GM spectra of HD, RV, VS, and IR are highly sensitive to the choice of cutoff wavenumber.

3.4 Spectral Analysis of VS and IR

Two principal linear components of perturbation potential vorticity are vortex stretching and relative vorticity. Since relative vorticity is negligibly small relative to vortex stretching at large scales, the conservation law of vortex stretching has been widely used for studying large-scale oceanic circulation. For small-scale oceanic motions, these two components can be equally important. An estimate of vortex stretching was attempted by Müller et al. (1988) using an estimated field of horizontal divergence. Since the vortical mode is horizontally nondivergent, only the gravity mode component of vortex stretching was obtained in their estimate. Note that in their calculation, the vortical mode contribution can exist through the nonlinear advection only.

Here, fluctuations of vortex stretching at small scales will be estimated using temperature measurements from IWEX. The vortex stretching is defined as $VS = f\partial_z\eta$. The vertical displacement, η, is obtained from temperature fluctuations normalized by a background temperature gradient given by

$$\eta = -\frac{T'}{\overline{\overline{\partial_z T}}}. \tag{3.31}$$

The background temperature gradient is estimated as the time average of temperature difference field over a vertical distance of 1.74 m taken in IWEX. The field of vortex stretching is estimated as

$$\widehat{VS} = f\frac{\overline{\eta}_{up} - \overline{\eta}_{low}}{H}. \tag{3.32}$$

Here, $\overline{\eta}_{up}$ and $\overline{\eta}_{low}$ are averaged vertical displacements at the upper and lower levels. H is the vertical distance between two successive levels. Vertical separation distances are shown in Table 2. Similarly, vertical shear of horizontal velocity can also be estimated by vertically differencing mean horizontal velocity between successive levels.

Spectral analysis is performed in the same manner for spectral estimates of $\overline{RV}$ and $\overline{HD}$. Spectra of horizontal velocity shear are used to obtain spectra of inverse Richardson number defined as

$$S_{\widehat{IR}}(\omega) = \frac{S_{\widehat{\partial_z u}}(\omega) + S_{\widehat{\partial_z v}}(\omega)}{N^2}. \tag{3.33}$$

Frequency spectra of $\widehat{VS}$ and $\widehat{IR}$ are displayed in Figures 26 and 27. They both show a spectral slope of -2 in the internal wave frequency band and drop with a slope of -3 to -4 beyond the Brunt–Väisälä frequency. Total variances of $\widehat{VS}$ and $\widehat{IR}$ are obtained by integrating over their frequency spectra (Table 2). The variance of $\widehat{VS}$ displays a monotonic decrease with increasing vertical separations. The corresponding *r.m.s.* vertical strain $(\partial_z \eta)$ ranges from 0.025 to 0.12. The variance of $\widehat{IR}$ also show a general decrease with increasing vertical separations. Corresponding Richardson numbers are much greater than the critical Richardson number for shear instability.

Similar to spectral estimates of $\overline{HD}$ and $\overline{RV}$, frequency spectra of $\widehat{VS}$ and $\widehat{IR}$ are described by their wavenumber-frequency spectra applying an array response function:

$$S_{\widehat{VS}}(\omega) = \int_{-\infty}^{\infty} d\beta \int_{0}^{\infty} d\alpha \left\{ S_{VS}(\omega, \alpha, \beta) \widehat{F}(\alpha, R_u, R_l, \beta H) \right\} \tag{3.34}$$

Table 2: Parameters and variance of estimated vortex stretching and inverse Richardson number

layer between levels	vertical separation (m)	mean buoyancy frequency (cph)	vertical cutoff wavenumber (cpm)	vortex stretching (s^{-2})	inverse Richardson number
2 and 5	34	2.57	$1.5 \cdot 10^{-2}$	$6.2 \cdot 10^{-11}$	$9.1 \cdot 10^{-2}$
5 and 6	91	2.71	$5.4 \cdot 10^{-3}$	$2.5 \cdot 10^{-11}$	$2.5 \cdot 10^{-2}$
6 and 10	292	2.41	$1.8 \cdot 10^{-3}$	$4.9 \cdot 10^{-12}$	$1.9 \cdot 10^{-3}$
10 and 14	1027	1.36	$4.8 \cdot 10^{-4}$	$2.9 \cdot 10^{-12}$	$2.0 \cdot 10^{-2}$

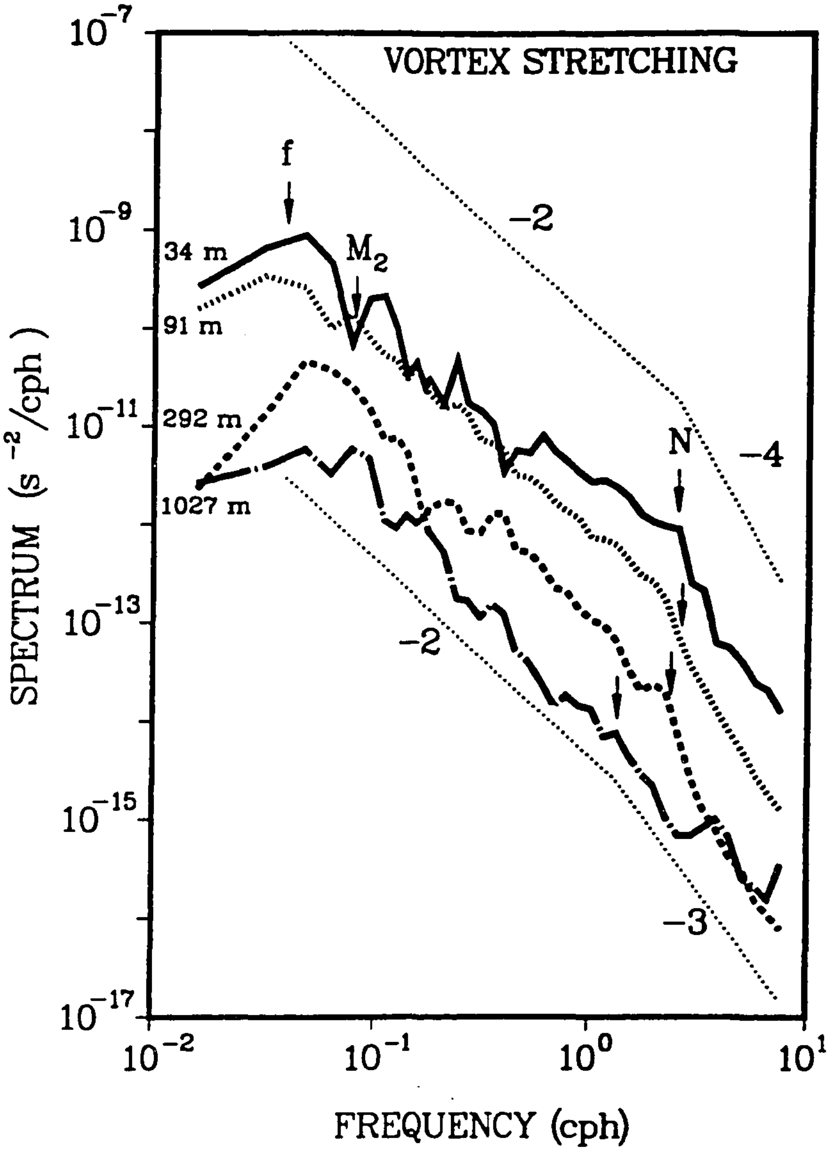

Figure 26: Frequency spectra of estimated vortex stretching obtained using measurements at two successive levels in IWEX separated vertically. Corresponding vertical separations between two successive levels are shown.

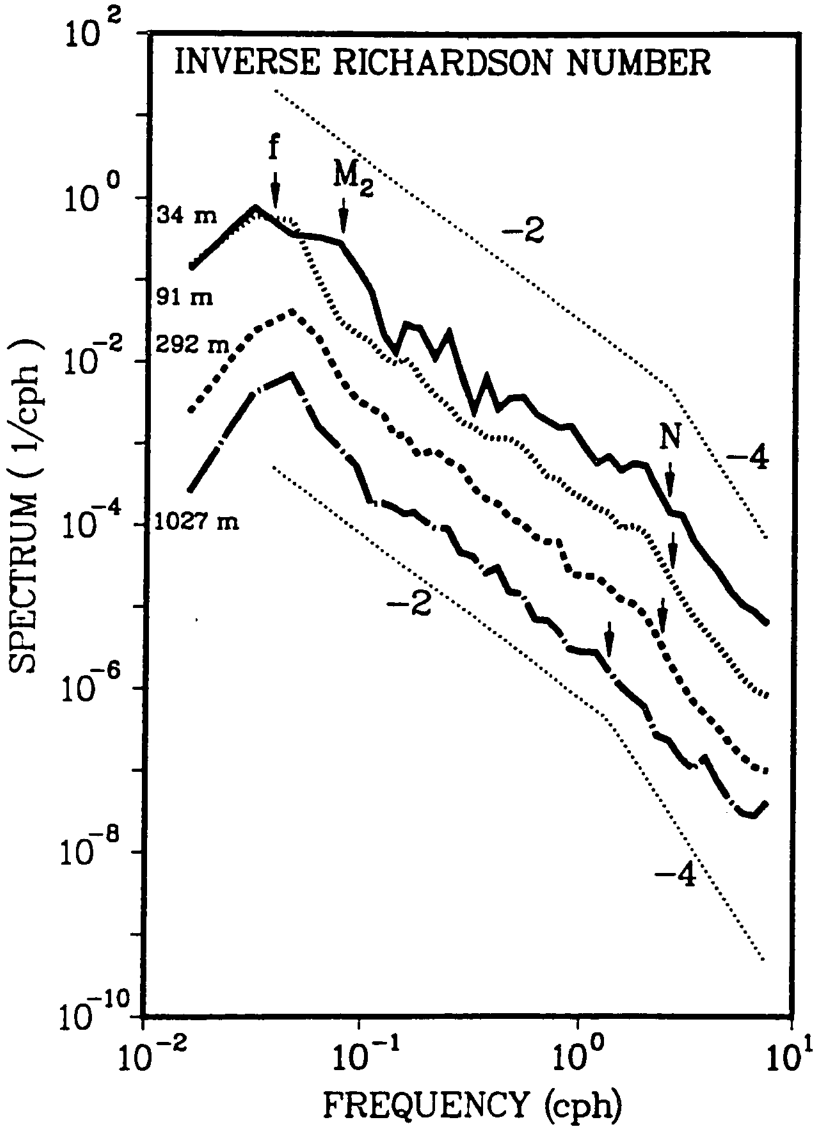

Figure 27: Frequency spectra of estimated inverse Richardson number obtained using measurements at two successive levels in IWEX separated vertically. Corresponding vertical separations between two successive levels are shown.

$$S_{\widehat{IR}}(\omega) = \int_{-\infty}^{\infty} d\beta \int_{0}^{\infty} d\alpha \left\{ S_{IR}(\omega,\alpha,\beta)\widehat{F}(\alpha,R_u,R_l,\beta H) \right\}, \tag{3.35}$$

with

$$\begin{aligned} \widehat{F}(\alpha,R_u,R_l,\beta H) = \; & \frac{2}{3(\beta H)^2} \left\{ \left[1 + J_o(\sqrt{3}\alpha R_u) + J_o(\sqrt{3}\alpha R_l) \right] \right. \\ & \left. -cos(\beta H) \left[J_o(\alpha \Delta R) + 2J_o(\alpha R') \right] \right\}. \end{aligned} \tag{3.36}$$

Here, $S_{VS}(\omega,\alpha,\beta)$ and $S_{IR}(\omega,\alpha,\beta)$ denote wavenumber-frequency spectra of vortex stretching and inverse Richardson number. R_u and R_l are radii of circles connecting three current meters at the upper and the lower levels, $\Delta R = \mid R_u - R_l \mid$ and $R' = \sqrt{R_u^2 + R_l^2 + R_u \cdot R_l}$. J_0 is the Bessel's function of the first kind of the zeroth order. The wavenumber array response function is very complicated since the horizontal wavenumber and the vertical wavenumber dependence are not separable due to the slanting of the IWEX mooring.

The array response function for frequency spectra of $\widehat{VS}$ and $\widehat{IR}$ using measurements at levels 5 and 6 is greater than one in the region where the vertical wavenumber is smaller than 10^{-3} cpm and the aspect ratio is greater than 3 (Figure 28). Small-scale oceanic motions rarely have such large vertical scales and small aspect ratio. In the regime of small aspect ratio or vertical wavenumber greater than 10^{-3} cpm, the horizontal wavenumber dependence of the array response function can be ignored, i.e.,

$$S_{\widehat{VS}}(\omega) \approx \int_{-\infty}^{\infty} d\beta \; S_{VS}(\omega,\beta)\widehat{F}(\beta H) \tag{3.37}$$

$$S_{\widehat{IR}}(\omega) \approx \int_{-\infty}^{\infty} d\beta \; S_{IR}(\omega,\beta)\widehat{F}(\beta H), \tag{3.38}$$

where $\widehat{F}(\beta H) = \left(\frac{sin(\beta H/2)}{\beta H/2} \right)^2$ is the simplified array response function (Figure 29).

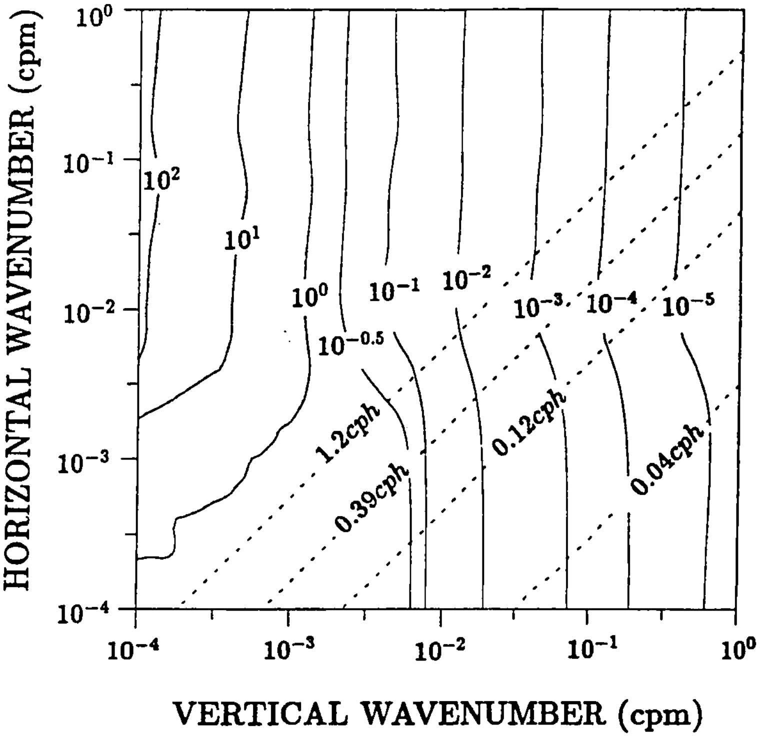

Figure 28: Array response function applied on spectra of vortex stretching and inverse Richardson number estimated from IWEX levels 5 and 6. Contours of the array response function are presented. Dashed lines denote constant constant frequencies of linear internal waves.

It has a -2 slope beyond the vertical wavenumber $\beta \sim 2/H$. For analytical convenience, it is approximated by a top-hat array response function with its cutoff wavenumber defined as

$$\hat{\beta} = \int_{-\infty}^{\infty} d\beta\, \hat{F}(\beta H) \approx \frac{3.12}{H}. \tag{3.39}$$

Vertical cutoff wavenumbers are described in Table 2. The smallest resolvable vertical scale is about 68 m. Therefore, estimated Richardson numbers suggest that the flow field at the IWEX site is stable with respect to the shear instability for vertical scales greater than 68 m.

Frequency spectra of $\widehat{VS}$ of the GM-76 model are estimated using the simplified array response function. Observed frequency spectral levels of $\widehat{VS}$ agree with GM spectra within 95% confidence level (Figures 30 - 33). In general, the GM-76 spectrum is slightly greater than observed spectra (except at the shallowest depth near the Brunt-Väisälä frequency). The spectral slope is very well explained by the GM model. Comparisons between observed frequency spectra of $\widehat{IR}$ and the GM-76 spectrum are displayed in Figures 34 - 37. Observed spectra are remarkably consistent with the corresponding GM spectra, in particular the -2 frequency spectral slope. Observed agreements imply that observed fluctuations of $\widehat{VS}$ and $\widehat{IR}$ are well explained by linear internal waves at vertical scales greater than the smallest resolvable scale (68 m).

The systematic decrease of spectral levels of $\widehat{VS}$ and $\widehat{IR}$ with the increasing vertical separation is presumably due to the effect of the array response function. Assuming a homogeneous physical environment, differences between frequency spectra estimated over different vertical separations can be converted to the vertical wavenumber information. Specifically, the vertical wavenumber-frequency spectrum can be approximated as

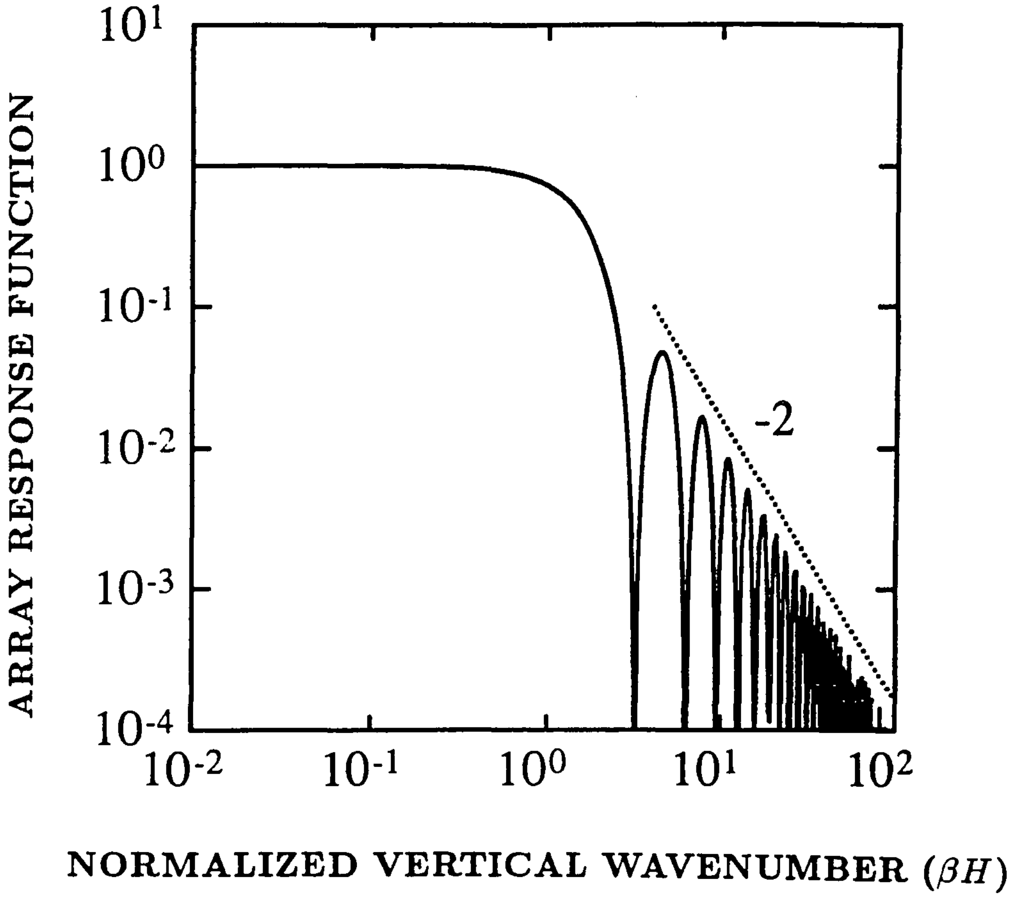

Figure 29: Simplified array response function for frequency spectral estimates of vortex stretching and inverse Richardson number. βH is the normalized vertical wavenumber.

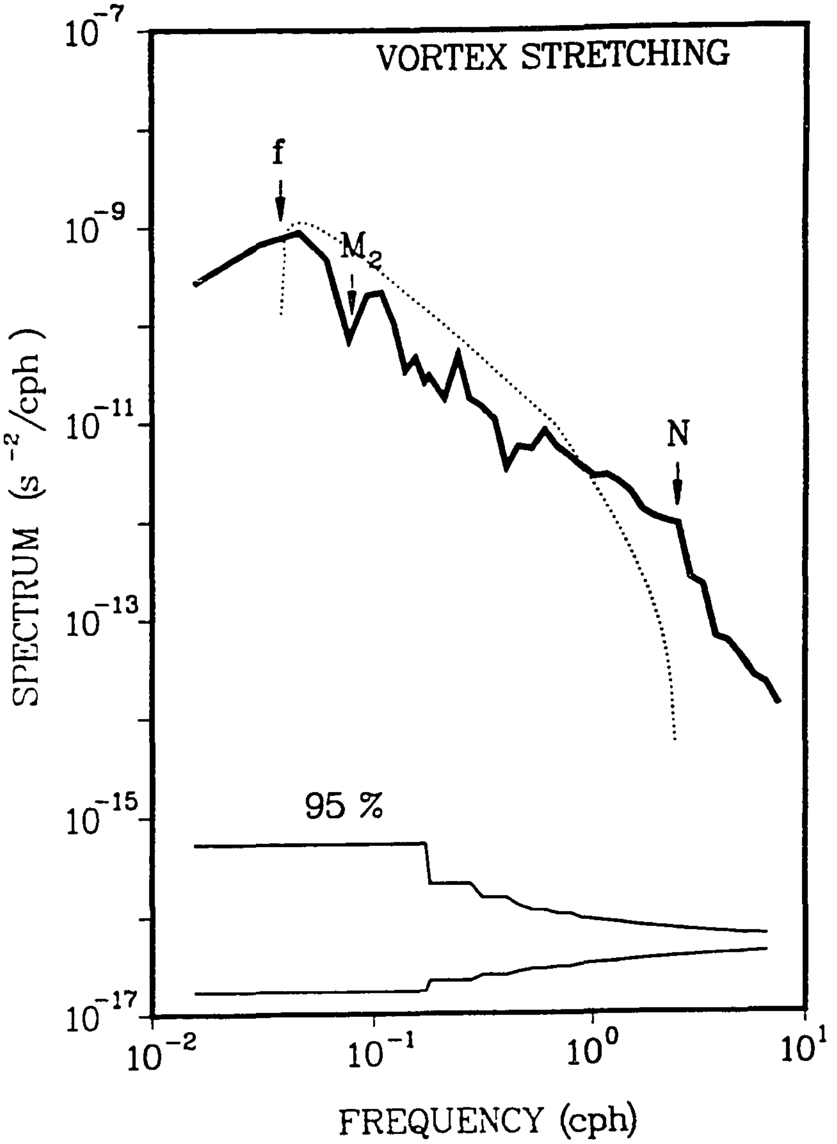

Figure 30: Frequency spectrum of vortex stretching (solid line) estimated between levels 2 and 5 compared with the GM spectrum (dotted line).

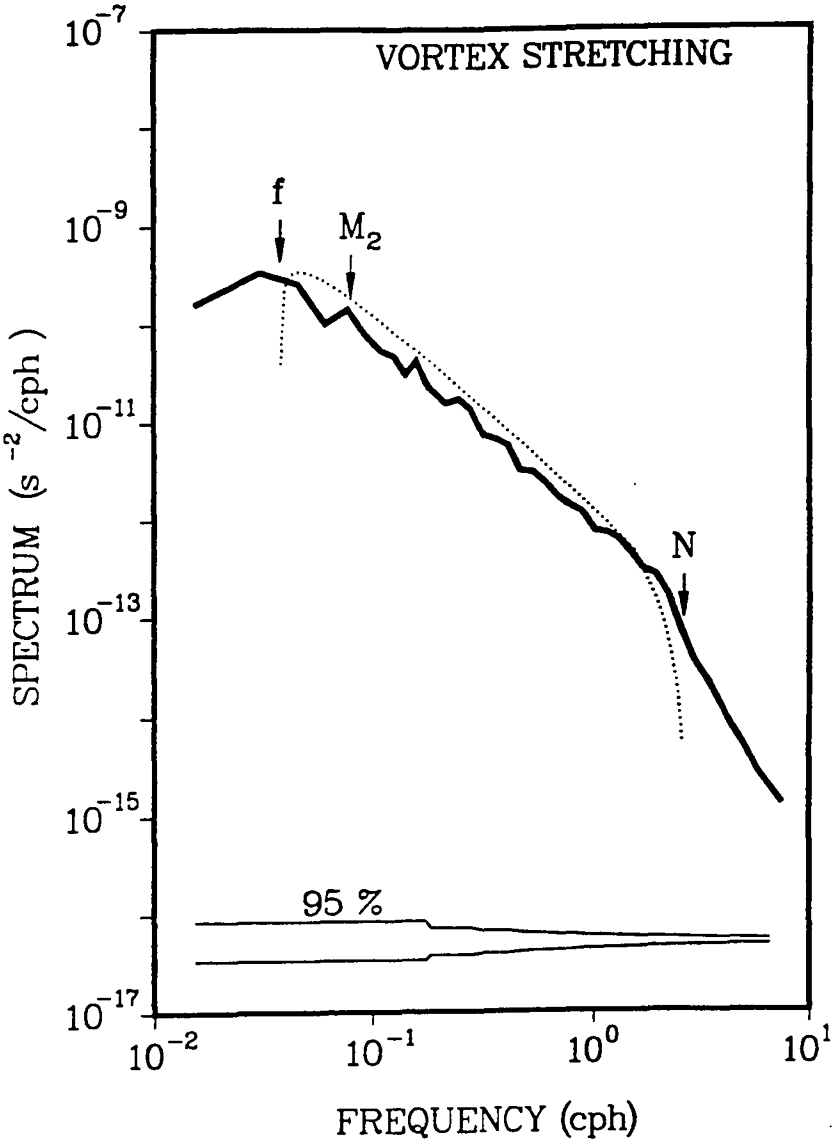

Figure 31: Frequency spectrum of vortex stretching (solid line) estimated between levels 5 and 6 compared with the GM spectrum (dotted line).

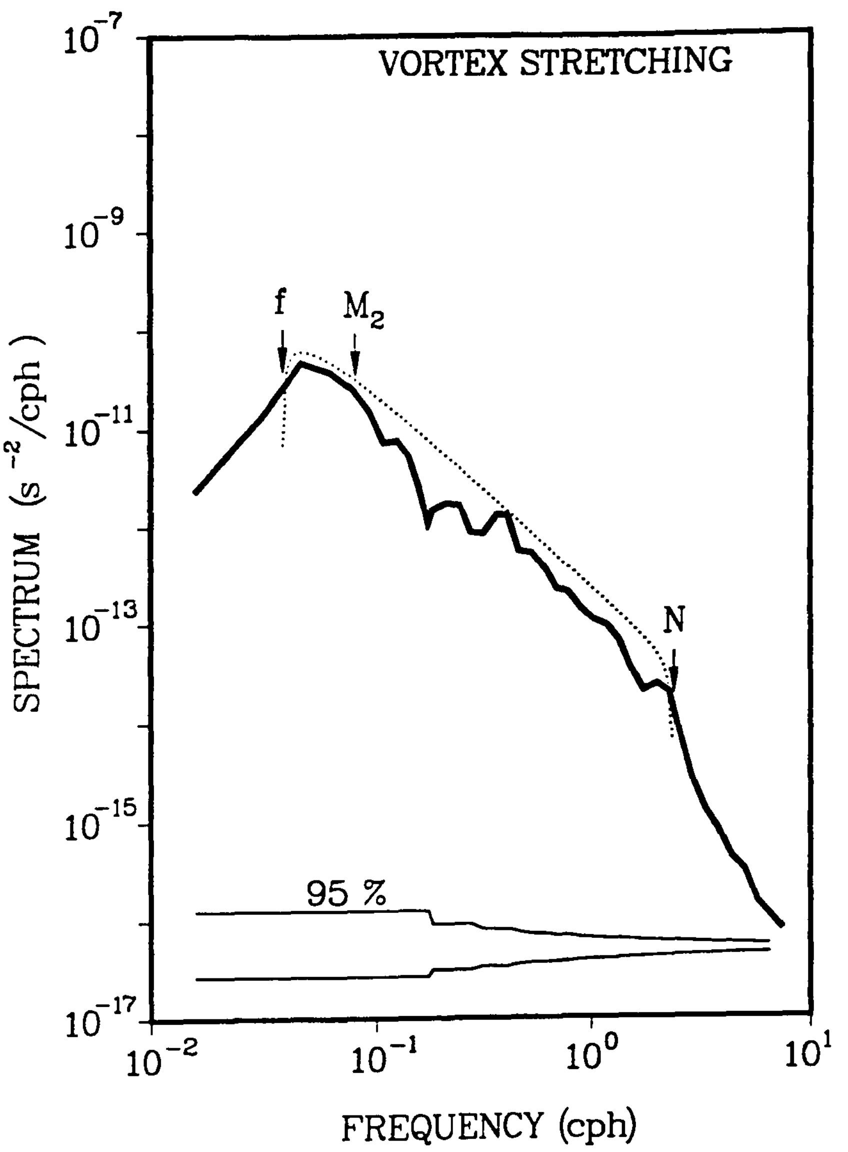

Figure 32: Frequency spectrum of vortex stretching (solid line) estimated between levels 6 and 10 compared with the GM spectrum (dotted line).

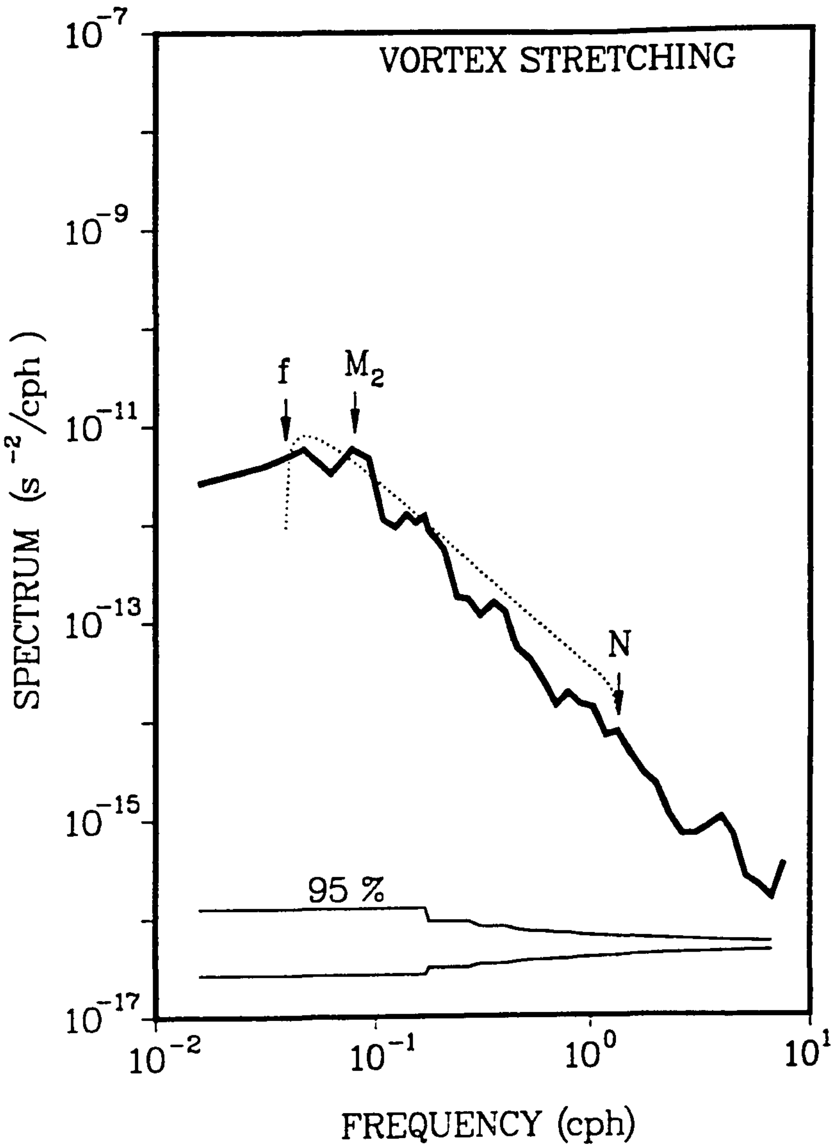

Figure 33: Frequency spectrum of vortex stretching (solid line) estimated between levels 10 and 14 compared with the GM spectrum (dotted line).

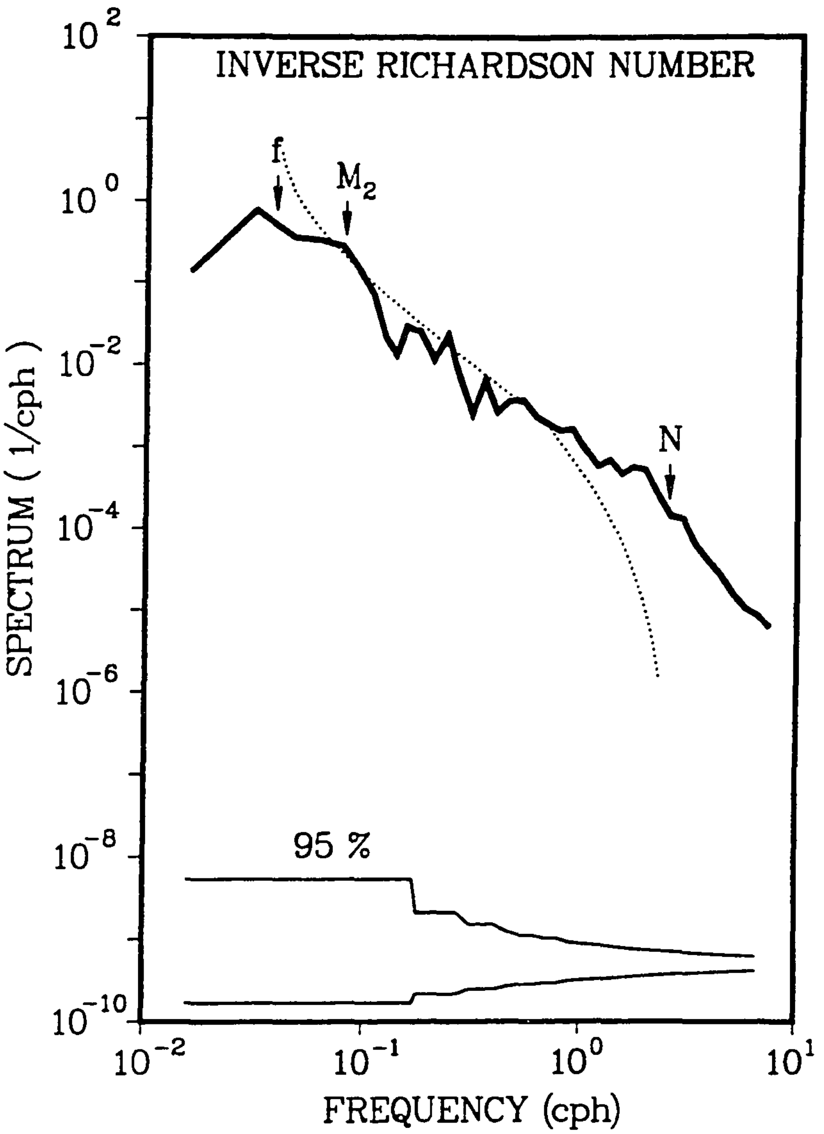

Figure 34: Frequency spectrum of inverse Richardson number (solid line) estimated between levels 2 and 5 compared with the GM spectrum (dotted line).

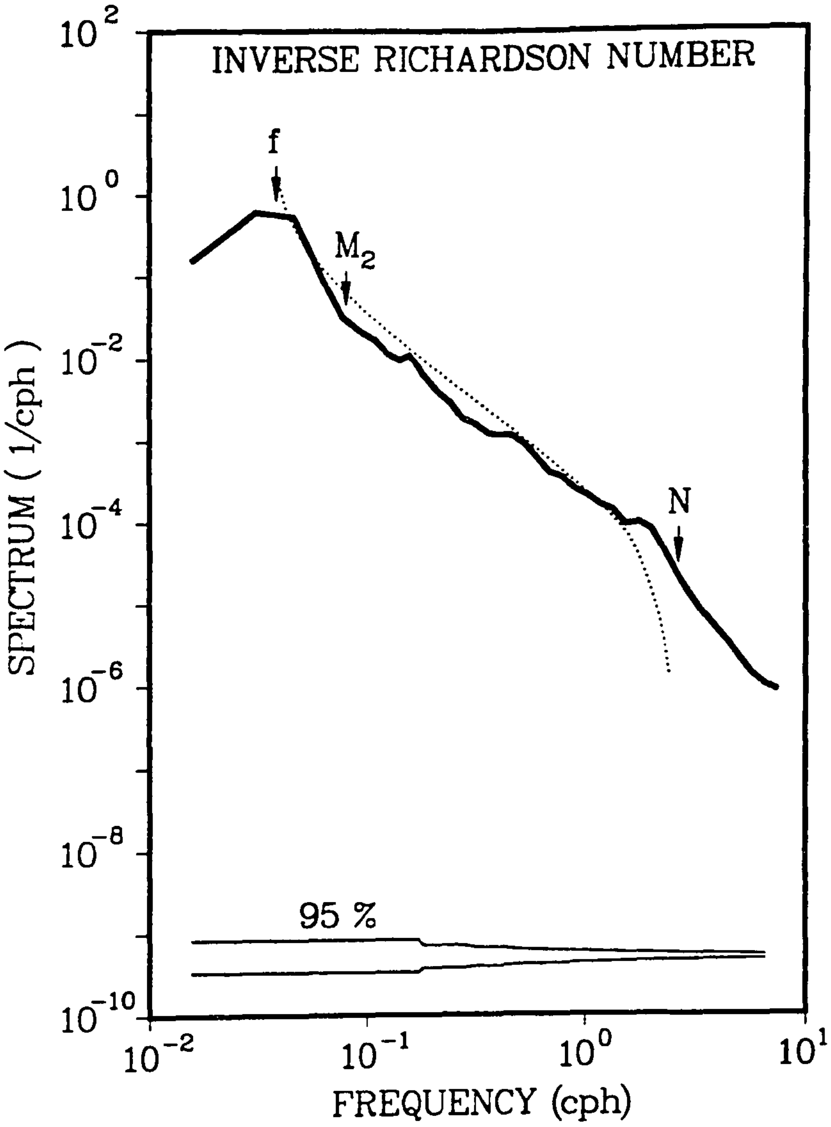

Figure 35: Frequency spectrum of inverse Richardson number (solid line) estimated between levels 5 and 6 compared with the GM spectrum (dotted line).

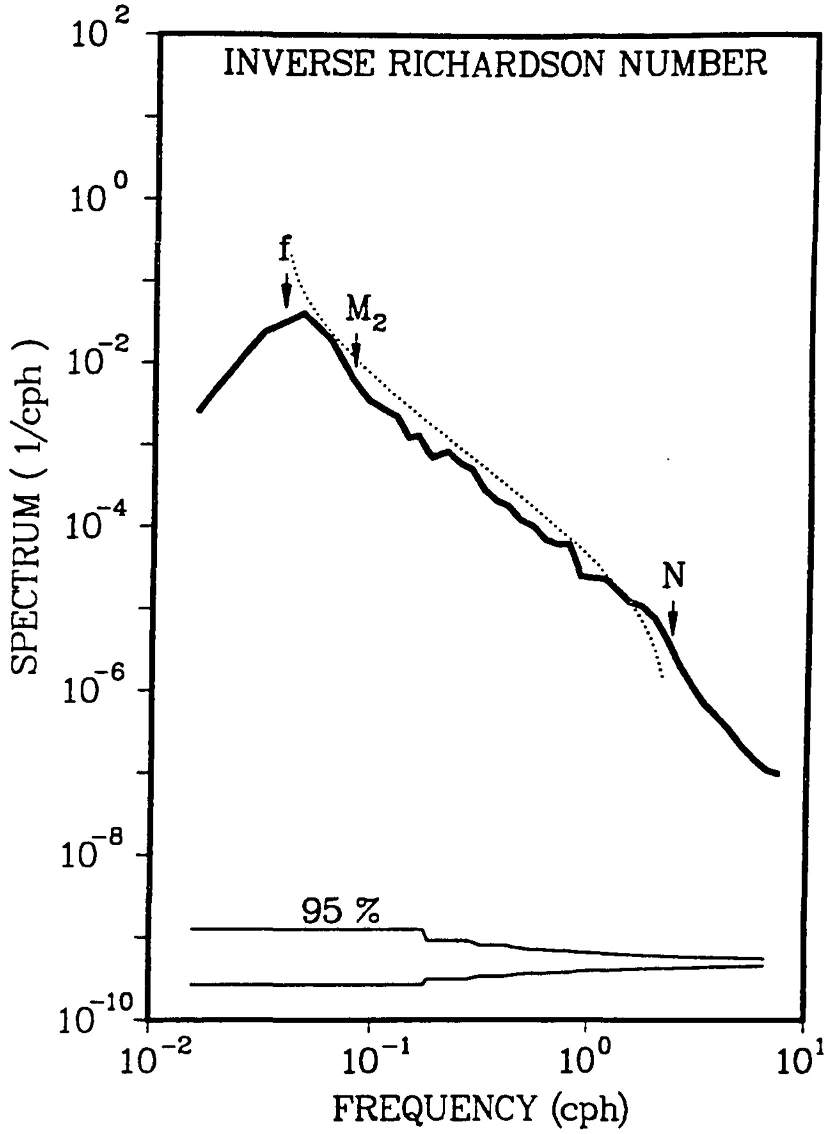

Figure 36: Frequency spectrum of inverse Richardson number (solid line) estimated between levels 6 and 10 compared with the GM spectrum (dotted line).

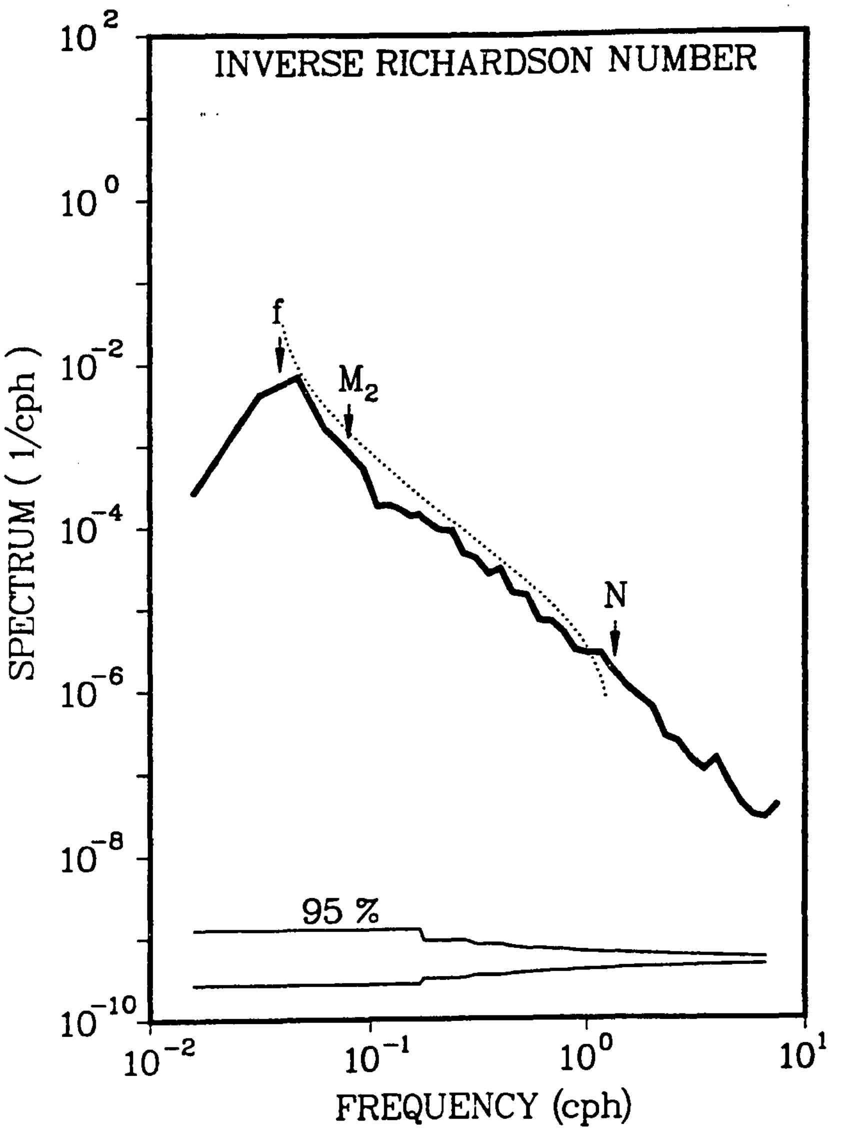

Figure 37: Frequency spectrum of inverse Richardson number (solid line) estimated between levels 10 and 14 compared with the GM spectrum (dotted line).

$$\widehat{S}(\beta_i,\omega) = \frac{S_i(\omega) - S_{i+1}(\omega)}{\widehat{\beta_i} - \widehat{\beta_{i+1}}}. \qquad (3.40)$$

Here, S_i denotes the frequency spectrum of $\widehat{VS}$ or $\widehat{IR}$ estimated between levels i and $i+1$, S_{i+1} denotes the frequency spectrum estimated from levels $i+1$ and $i+2$. The corresponding vertical cutoff wavenumbers are $\widehat{\beta}_i$ and $\widehat{\beta}_{i+1}$. In this analysis, three vertical wavenumbers can be resolved centering at $\beta_i = (\widehat{\beta}_i + \widehat{\beta}_{i+1})/2$. Vertical wavenumber–frequency spectra of $\widehat{VS}$ and $\widehat{IR}$ are displayed in Figures 38 and 39. Vertical wavenumber spectra of $\widehat{VS}$ and $\widehat{IR}$ (Figures 40 and 41) are obtained by integrating vertical wavenumber–frequency spectra over the frequency domain. The estimated vertical wavenumber spectrum of $\widehat{VS}$ agrees with Gregg's results (1977) to the order of magnitude with a multiplication of f^2 to his normalized temperature gradient spectrum. Since only three vertical wavenumbers are resolved, the wavenumber spectral slope is not well defined. Gargett et al. (1981) found the vertical wavenumber spectrum of current shear of $1 \sim 3 \times 10^{-4}$ s^{-2} and a zero slope for vertical wavenumbers smaller than 10^{-1} cpm. The corresponding inverse Richardson number spectrum is about 10 (cpm)$^{-1}$. This also agrees well with our estimates at vertical wavenumbers β_2 and β_5, whereas our spectral estimate is about one order smaller than their result at ($\sim 10^{-3}$ cpm). This might be due to the simplification of the array response function which is not suitable at vertical wavenumbers smaller than $O(10^{-3}$ cpm).

3.5 Proposed Normal Mode Decomposition Using HD and RV

The system of small–scale motions can be completely described by three prognostic variables HD, RV, and VS. The linear eigenmode representation has been

VORTEX STRETCHING SPECTRUM

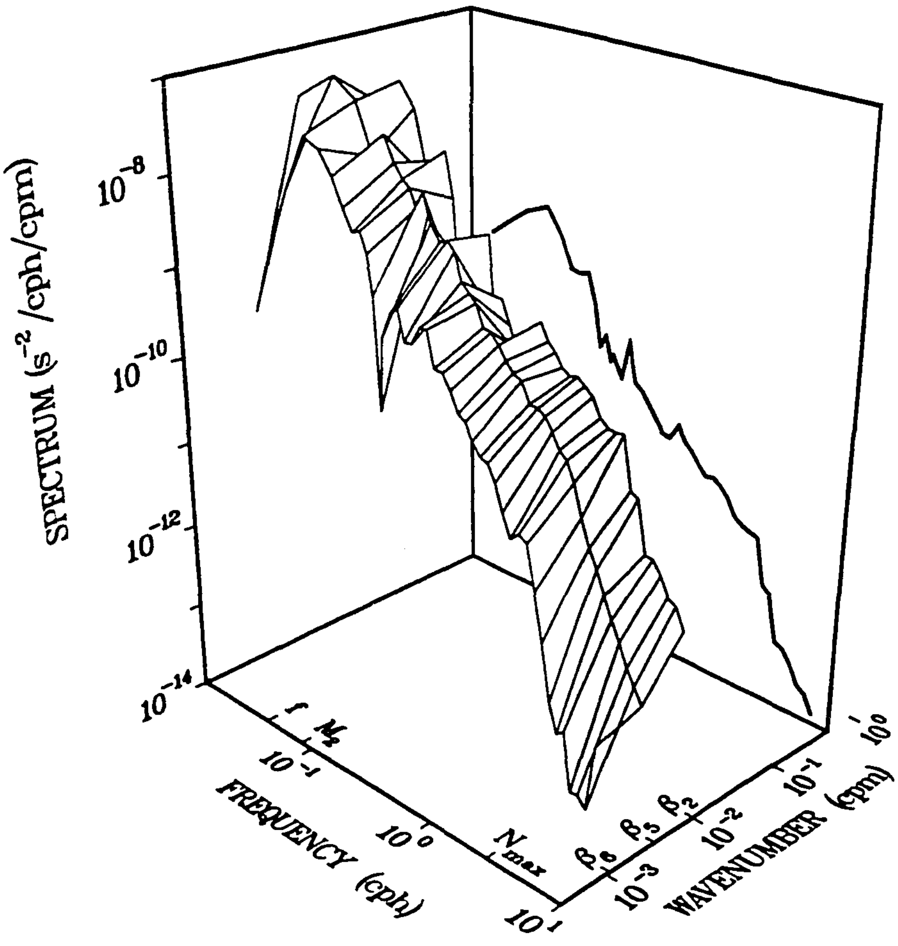

Figure 38: Vertical wavenumber–frequency spectrum of vortex stretching. Three vertical wavenumber bands are resolved centering at $\beta_i = (\widehat{\beta}_i + \widehat{\beta}_{i+1})/2$. $\widehat{\beta}$ is the vertical cutoff wavenumber.

INVERSE RICHARDSON NUMBER SPECTRUM

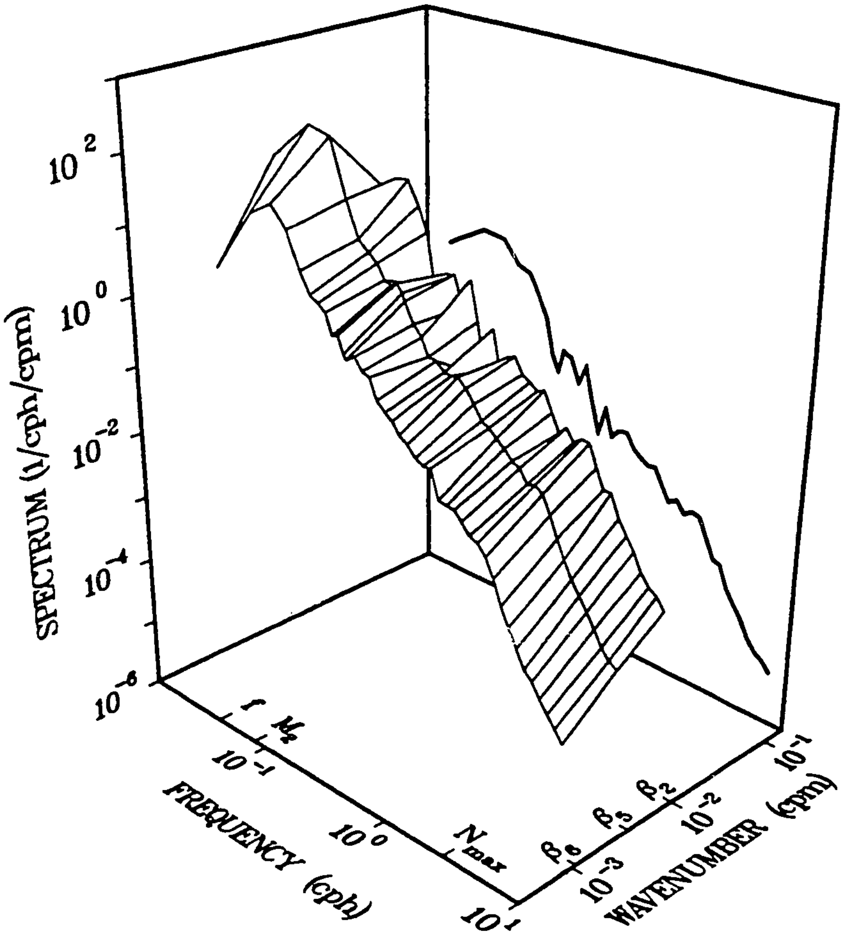

Figure 39: Vertical wavenumber-frequency spectrum of inverse Richardson number. Three vertical wavenumber bands are resolved centering at $\beta_i = (\widehat{\beta}_i + \widehat{\beta}_{i+1})/2$. $\widehat{\beta}$ is the vertical cutoff wavenumber.

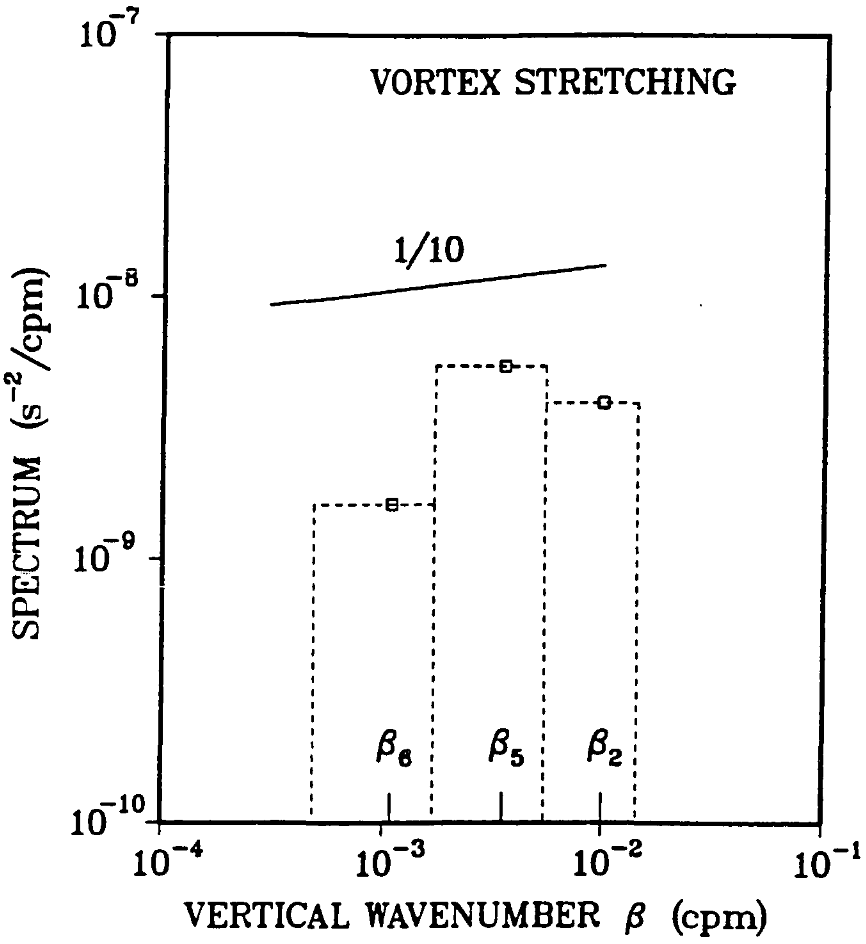

Figure 40: Vertical wavenumber spectrum of vortex stretching (square symbols). Normalized temperature gradient spectrum observed by Gregg (1977) is transformed to the vortex stretching spectrum (solid line) which has a 1/10 slope.

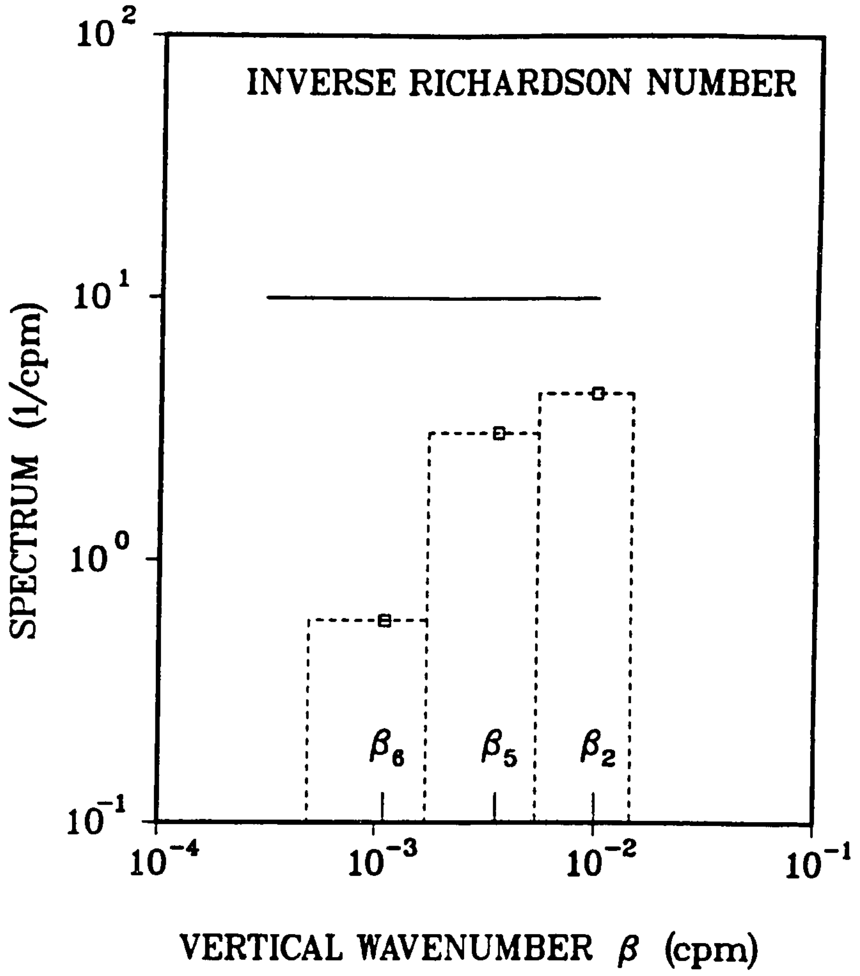

Figure 41: Vertical wavenumber spectrum of inverse Richardson number (square symbols). The current shear spectrum estimated by Gargett et al. (1981) is transformed to the inverse Richardson number spectrum (solid line) which has a zero slope.

discussed in section 2.1. Specifically, the gravity and vortical components of these variables are defined at each wave vector and instant in time (eqs. 2.33 and 2.34) as

$$\begin{pmatrix} HD_s^g(\underline{k},t) \\ RV_s^g(\underline{k},t) \\ VS_s^g(\underline{k},t) \end{pmatrix} = \begin{pmatrix} -i\frac{\omega_s}{f} \\ 1 \\ 1 \end{pmatrix} \frac{k_z \alpha f}{\sqrt{2}\sigma K} a_s^g(\underline{k},t) \tag{3.41}$$

$$\begin{pmatrix} HD^v(\underline{k},t) \\ RV^v(\underline{k},t) \\ VS^v(\underline{k},t) \end{pmatrix} = \begin{pmatrix} 0 \\ 1 \\ -\frac{f^2 k_z^2}{N^2 \alpha^2} \end{pmatrix} \frac{N\alpha^2}{\sigma K} a^v(\underline{k},t). \tag{3.42}$$

Superscripts g and v denote the gravity and vortical components. These relations clearly describe kinematic structures of the gravity and vortical modes:

- The vortical mode is horizontally nondivergent. Therefore, fluctuations of horizontal divergence result entirely from the gravity mode.

- The gravity mode does not carry linear perturbation potential vorticity, whereas the vortical mode carries the linear perturbation potential vorticity with a fixed ratio between the relative vorticity and vortex stretching.

- For the linear gravity mode, the ratio between frequency spectra of horizontal divergence and relative vorticity is ω^2/f^2, and their phase spectrum should be 90° out of phase.

These characteristics are very useful for the decomposition of relative vorticity and horizontal kinetic energy spectrum into gravity and vortical components.

Assuming measurements of uncontaminated HD and RV were obtained, observed RV can be decomposed into its gravity and vortical components as

$$\overline{RV}^g(t) = \overline{VS}^g(t) = f\overline{\partial_z\eta}^g(t) = -f\int_0^t dt'\overline{HD}(t') \tag{3.43}$$

$$\overline{RV}^v(t) = \overline{RV}(t) - \overline{RV}^g(t). \tag{3.44}$$

Here, a linear gravity mode is assumed. A bandpass filter should first be applied on observed HD to extract fluctuations in the internal wave frequency band. The gravity component of RV as well as VS can be obtained by the time integration of the bandpassed HD. Accordingly, the vortical component is the residual of the observed RV and the gravity component.

Horizontal wavenumber–frequency spectrum of horizontal kinetic energy $S_{HK}(\alpha,\omega)$ is related to spectra of relative vorticity and horizontal divergence as

$$S_{HK}(\alpha,\omega) = \frac{1}{2\alpha^2}\left[S_{RV}(\alpha,\omega) + S_{HD}(\alpha,\omega)\right]. \tag{3.45}$$

The gravity and vortical components of horizontal kinetic energy spectrum can be defined as:

$$S^g_{HK}(\alpha,\omega) = \frac{1}{2\alpha^2}\left[S^g_{RV}(\alpha,\omega) + S^g_{HD}(\alpha,\omega)\right] \tag{3.46}$$

$$S^v_{HK}(\alpha,\omega) = \frac{1}{2\alpha^2}S^v_{RV}(\alpha,\omega). \tag{3.47}$$

Here, $S^g_{HK}(\alpha,\omega)$ and $S^v_{HK}(\alpha,\omega)$ are horizontal wavenumber–frequency spectra of horizontal kinetic energy of gravity and vortical modes.

The normal mode decomposition of relative vorticity and horizontal kinetic energy requires uncontaminated estimates of RV and HD. Unfortunately, estimates of $\overline{RV}$ and $\overline{HD}$ are potentially contaminated with each other. The normal mode decomposition can not be achieved at this stage.

Chapter 4

Summary and Conclusion

The primary goal of this study was to understand small-scale oceanic motions which include both internal gravity waves and vortical motion. Traditionally, internal gravity waves are treated as the only motion at small scales. However, since internal waves do not carry perturbation potential vorticity, the vortical mode must be present to carry the perturbation potential vorticity at small scales. Coexistence of internal waves and vortical motion at small scales has been supported by oceanic observations, numerical models, and laboratory experiments. Discrepancies between oceanic measurements in the time scale of internal waves and linear internal wave theory have been found (Müller et al., 1978). Three-dimensional numerical studies (Riley et al., 1981) and laboratory experiments (Lin and Pao, 1979) also found the coexistence of internal waves and vortical motions.

The fundamental objective of this study was to decompose small-scale motions into gravity waves and vortical motion. The major distinction between these two types of motions is the perturbation potential vorticity which is, in general, a nonlinear quantity. Therefore, a linear decomposition is impossible to perform except in a linear system in which only the linear components of the perturbation potential vorticity exist.

Using eigenvectors of the linear equations of motion, the gravity and vortical modes are defined. The gravity mode propagates and does not carry linear perturbation potential vorticity. The vortical mode is stagnant and carries linear perturbation potential vorticity. The linear gravity mode has a ratio between the horizontal divergence spectrum and the relative vorticity spectrum as a function of frequency only. The vortical mode has a fixed ratio of the relative vorticity and vortex stretching spectra and is horizontally nondivergent.

In the linear system, the normal mode decomposition of the flow field into its gravity mode and vortical mode is unambiguous. An example of the geostrophic adjustment problem was illustrated. The initial surface disturbance field is decomposed into its gravity wave and the geostrophic flow components. The final state is steady geostrophic flow, while the gravity wave carries energy away from the disturbed field. To justify the application to a nonlinear model, the normal mode decomposition was employed on a nonlinear vortical motion with a monopole dynamic. At small Rossby and Burger numbers, the gravity mode component is negligible. Since the normal mode decomposition is based on the linear perturbation potential vorticity while the monopole has the nonlinear component of perturbation potential vorticity as well, a weak gravity mode was also obtained.

The normal mode decomposition can be conveniently performed using measurements of horizontal divergence, relative vorticity, and vortex stretching. Using velocity measurements from IWEX, fluctuations of area–averaged horizontal divergence, and relative vorticity at different depths were estimated using Stokes' and Gauss' theorems. There are two potential problems with the estimation of horizontal divergence and relative vorticity using discrete sampling of velocity measurements along a circle of finite size. First, due to the finite size of the circle, fluctuations at scales smaller than the scale of the circle are attenuated. Second, due to the discrete sampling of velocity measurements along the circle, there is contamination between the horizontal divergence and relative vorticity. Increasing the number of velocity sensors along the circle can reduce the effect of the contamination error, but the attenuation error will remain.

The GM–76 internal wave spectrum model was compared with frequency spectral estimates of horizontal divergence and relative vorticity. Frequency spectral estimates of horizontal divergence were well represented by the corresponding GM–76 spectra, whereas discrepancies were found in frequency spectral estimates of relative vorticity at levels 5 (640 m depth) and 6 (731 m depth). However, we cannot conclude whether observed discrepancies were due to the existence of small–scale vortical motion or the failure of the GM–76 spectrum model to predict the internal wave spectrum of horizontal divergence and relative vorticity at small scales. The GM spectrum of the horizontal divergence and relative vorticity is very sensitive to the choice of the horizontal cutoff wavenumber which is not well defined.

An inverse transformation was attempted to derive horizontal wavenumber–frequency spectra of horizontal divergence and relative vorticity. Unfortunately, it requires frequency spectral estimates of horizontal divergence and relative vorticity in continuous sizes of circles. The inverse transform is impossible using only few frequency spectral estimates from IWEX.

Fluctuations of vortex stretching and inverse Richardson number were estimated from IWEX. Both spectral levels and spectral slopes agree very well with the corresponding GM spectra. Vertical wavenumber spectra of vortex stretching and inverse Richardson number were obtained and are consistent with results from Gregg (1977) and Gargett et al. (1981).

A general scheme of the normal mode decomposition of the relative vorticity and the horizontal kinetic energy spectra using uncontaminated measurements of horizontal divergence and relative vorticity was proposed. Since we were not able to decontaminate estimates of horizontal divergence and relative vorticity, the normal mode decomposition cannot be performed.

It is clear that the normal mode decomposition can be made most conveniently using fields of horizontal divergence, relative vorticity, and vortex stretching. In the previous IWEX analysis by Müller et al. (1978), current finestructure with a vertical wavelength from about 1 m to 10 m were found from the vertical coherence spectrum. Later, Müller (1984) proposed that the current finestructure represents small–scale vortical motion. If small–scale vortical motion does exist only at small vertical scales, vertical wavenumber spectra of horizontal divergence, and relative vorticity will be needed to detect it.

Appendix A

Array Response Functions for Spectra of $\overline{HD}$ and $\overline{RV}$

Horizontal velocity measurements from a triad of current meters of IWEX are used to estimate fields of horizontal divergence (HD) and relative vorticity (RV). The configuration of the triad current meters is displayed in Figure 42. Time series of HD and RV were estimated using horizontal velocity components from three current meters on a horizontal plane. Because of discrete sampling in space (three current meters only) and the finite separation among current meters (ranging from 8.5 m to 1600 m), there are two potential errors in frequency spectral estimates of $\overline{HD}$ and $\overline{RV}$.

By applying Stokes' theorem and Gauss' theorem over the circle connecting three current meters on a horizontal plane, area–averaged horizontal divergence and relative vorticity are estimated as

$$\overline{HD}(t) = \frac{2}{3R} \sum_{k=A,B,C} \{u_k(t) cos\theta_k + v_k(t) sin\theta_k\} \tag{A.1}$$

$$\overline{RV}(t) = \frac{2}{3R} \sum_{k=A,B,C} \{v_k(t) cos\theta_k - u_k(t) sin\theta_k\}\,. \tag{A.2}$$

Here, $A, B,$and C denote three current meters, θ_k the counterclockwise orientation

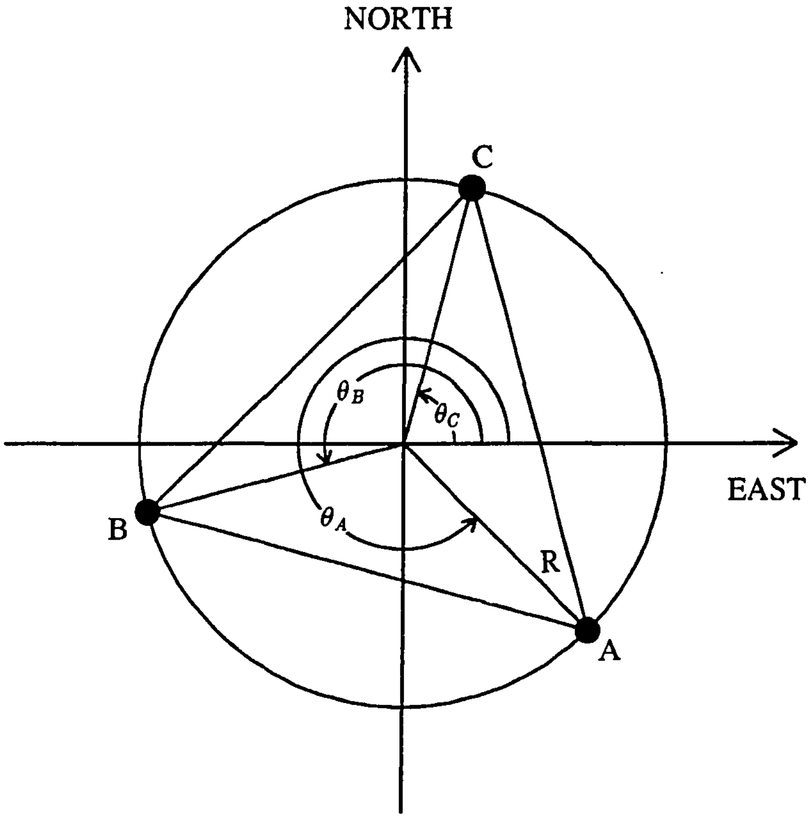

Figure 42: The mooring configuration of a triad of current meters on a horizontal plane.

of the current meter from the east direction, and R the radius of the circle. u and v are east and north velocity components. The overbar denotes the estimated field.

Assuming statistical homogeneity, frequency spectra of estimated $\overline{HD}$ and $\overline{RV}$ can be expressed as

$$
\begin{aligned}
S_{\overline{HD}}(\omega; R) = \; & \tfrac{4}{9R^2} \int_0^\infty d\alpha \int_0^{2\pi} \alpha d\phi \, \{S_u(\alpha, \phi, \omega) F_2(\alpha R, \theta_C, \phi) + S_v(\alpha, \phi, \omega) F_1(\alpha R, \theta_C, \phi) \\
& + S_{uv}(\alpha, \phi, \omega) F_3^*(\alpha R, \theta_C, \phi) + S_{vu}(\alpha, \phi, \omega) F_3(\alpha R, \theta_C, \phi)\}
\end{aligned}
\tag{A.3}
$$

$$
\begin{aligned}
S_{\overline{RV}}(\omega; R) = \; & \tfrac{4}{9R^2} \int_0^\infty d\alpha \int_0^{2\pi} \alpha d\phi \, \{S_u(\alpha, \phi, \omega) F_1(\alpha R, \theta_C, \phi) + S_v(\alpha, \phi, \omega) F_2(\alpha R, \theta_C, \phi) \\
& - S_{uv}(\alpha, \phi, \omega) F_3(\alpha R, \theta_C, \phi) - S_{vu}(\alpha, \phi, \omega) F_3^*(\alpha R, \theta_C, \phi)\} \, .
\end{aligned}
\tag{A.4}
$$

$S_u(\alpha, \phi, \omega)$ and $S_v(\alpha, \phi, \omega)$ are wavenumber–frequency spectra of horizontal velocity components. $S_{uv}(\alpha, \phi, \omega)$ and $S_{vu}(\alpha, \phi, \omega)$ are their cross-spectra. α is the horizontal wavenumber magnitude, ϕ the orientation of the wavenumber vector counterclockwise from the east. The superscript asterisk denotes the complex conjugate. F_1, F_2 and F_3 are three array response functions given by

$$
\begin{aligned}
F_1(\alpha R, \theta_C, \phi) = \; & \Big\{ \tfrac{3}{2} + 2sin(\theta_C - \tfrac{2}{3}\pi) sin(\theta_C + \tfrac{2}{3}\pi) cos[\sqrt{3}\, \alpha R \; cos(\phi - \theta_C + \tfrac{\pi}{2})] \\
& + 2sin(\theta_C - \tfrac{2}{3}\pi) sin(\theta_C) cos[\sqrt{3}\, \alpha R \; cos(\phi - \theta_C - \tfrac{7}{6}\pi)] \\
& + 2sin(\theta_C + \tfrac{2}{3}\pi) sin(\theta_C) cos[\sqrt{3}\, \alpha R \; cos(\phi - \theta_C - \tfrac{5}{6}\pi)] \Big\} \, ,
\end{aligned}
\tag{A.5}
$$

$$
\begin{aligned}
F_2(\alpha R, \theta_C, \phi) = \; & \Big\{ \tfrac{3}{2} + 2cos(\theta_C - \tfrac{2}{3}\pi) cos(\theta_C + \tfrac{2}{3}\pi) cos[\sqrt{3}\, \alpha R \; cos(\phi - \theta_C + \tfrac{\pi}{2})] \\
& + 2cos(\theta_C - \tfrac{2}{3}\pi) cos(\theta_C) cos[\sqrt{3}\, \alpha R \; cos(\phi - \theta_C - \tfrac{7}{6}\pi)] \\
& + 2cos(\theta_C + \tfrac{2}{3}\pi) cos(\theta_C) cos[\sqrt{3}\, \alpha R \; cos(\phi - \theta_C - \tfrac{5}{6}\pi)] \Big\} \, ,
\end{aligned}
\tag{A.6}
$$

and

$$\begin{aligned} F_3(\alpha R,\theta_C,\phi) = \; & sin(\theta_C - \tfrac{2}{3}\pi)cos(\theta_C + \tfrac{2}{3}\pi)\cdot exp\left\{i\sqrt{3}\,\alpha R\,cos(\phi - \theta_C + \tfrac{\pi}{2})\right\} \\ & + sin(\theta_C - \tfrac{2}{3}\pi)cos(\theta_C)\cdot exp\left\{i\sqrt{3}\,\alpha R\,cos(\phi - \theta_C - \tfrac{7}{6}\pi)\right\} \\ & + sin(\theta_C + \tfrac{2}{3}\pi)cos(\theta_C - \tfrac{2}{3}\pi)\cdot exp\left\{-i\sqrt{3}\,\alpha R\,cos(\phi - \theta_C + \tfrac{\pi}{2})\right\} \\ & + sin(\theta_C + \tfrac{2}{3}\pi)cos(\theta_C)\cdot exp\left\{i\sqrt{3}\,\alpha R\,cos(\phi - \theta_C - \tfrac{5}{6}\pi)\right\} \\ & + sin(\theta_C)cos(\theta_C - \tfrac{2}{3}\pi)\cdot exp\left\{-i\sqrt{3}\,\alpha R\,cos(\phi - \theta_C - \tfrac{7}{6}\pi)\right\} \\ & + sin(\theta_C)cos(\theta_C + \tfrac{2}{3}\pi)\cdot exp\left\{-i\sqrt{3}\,\alpha R\,cos(\phi - \theta_C - \tfrac{5}{6}\pi)\right\}. \end{aligned} \tag{A.7}$$

Since θ_C, θ_B, and θ_A are lagged by $\frac{2}{3\pi}$ successively, θ_C was chosen to be the only independent parameter that describes the orientation of the mooring. Apparently, these array response functions depend on the radius of the circle, the magnitude and direction of the horizontal wavenumber relative to the mooring array. Frequency spectral estimates of $\overline{HD}$ and $\overline{RV}$ are related to four independent wavenumber-frequency spectra $S_u(\alpha,\phi,\omega)$, $S_v(\alpha,\phi,\omega)$, and $S_{uv}(\alpha,\phi,\omega)$ (including the real and the imaginary components). In general, they cannot be represented completely in terms of $S_{HD}(\alpha,\phi,\omega)$ and $S_{RV}(\alpha,\phi,\omega)$ except in some limiting cases such as isotropic or unidirectional flow fields (Prater, 1989).

A.1 Isotropic Flow Field

Isotropy conditions of velocity wavenumber spectra were found by Batchelor (1953). The velocity cross-spectra can be expressed as

$$S_u(k_x, k_y) = A(\alpha)k_x^2 + B(\alpha) \tag{A.8}$$

$$S_v(k_x, k_y) = A(\alpha)k_y^2 + B(\alpha) \tag{A.9}$$

$$S_{uv}(k_x, k_y) = S_{vu}(k_x, k_y) = A(\alpha)k_x k_y, \tag{A.10}$$

where $A(\alpha)$ and $B(\alpha)$ are arbitrary even functions of α. Accordingly, frequency–wavenumber spectra of HD and RV can be described as

$$S_{HD}(\alpha, \phi, \omega) = \alpha^4 A(\alpha, \omega) + \alpha^2 B(\alpha, \omega) \tag{A.11}$$

$$S_{RV}(\alpha, \phi, \omega) = \alpha^2 B(\alpha, \omega). \tag{A.12}$$

Under the horizontal isotropy condition, frequency spectral estimates of $\overline{HD}$ and $\overline{RV}$ can be represented in terms of wavenumber-frequency spectra of HD and RV and two array response functions (Figure 15), i.e.,

$$S_{\overline{HD}}(\omega, R) = \int_0^\infty d\alpha \left\{S_{HD}(\alpha, \omega)F(\alpha R) + S_{RV}(\alpha, \omega)G(\alpha R)\right\} \tag{A.13}$$

$$S_{\overline{RV}}(\omega, R) = \int_0^\infty d\alpha \left\{S_{RV}(\alpha, \omega)F(\alpha R) + S_{HD}(\alpha, \omega)G(\alpha R)\right\} \tag{A.14}$$

$$F(\alpha R) = \frac{2}{3\alpha^2 R^2}\left[1 - J_0(\sqrt{3}\,\alpha R\,) + 2J_2(\sqrt{3}\,\alpha R\,)\right] \tag{A.15}$$

$$G(\alpha R) = \frac{2}{3\alpha^2 R^2}\left[1 - J_0(\sqrt{3}\,\alpha R\,) - 2J_2(\sqrt{3}\,\alpha R\,)\right]. \tag{A.16}$$

Here, J_0 and J_2 are Bessel functions of the first kind of zeroth and second order, respectively. $F(\alpha R)$ is an attenuation array response function with a cutoff wavenumber of approximately $\frac{1}{R}$ and a -2 spectral slope beyond the cutoff wavenumber. $G(\alpha R)$ is a contamination array response function with a +2 spectral slope in the low wavenumber region and a -2 slope in the high wavenumber region. It reaches a peak of 0.1 at the wavenumber $\alpha \approx \frac{5}{R}$. Beyond this wavenumber, F and G are of the same order.

A.2 Unidirectional Flow Field

For any arbitrary unidirectional flow field $v(x, y, t) = c\, u(x, y, t)$, frequency spectral estimates of $\overline{HD}$ and $\overline{RV}$ can be described as

$$\begin{aligned} S_{\overline{HD}}(\omega) = \ & \tfrac{4}{9R^2} \int_0^\infty d\alpha \int_0^{2\pi} \alpha d\phi \ S_u(\alpha, \phi, \omega) \\ & \cdot \{c^2 \cdot F_1(\alpha R, \theta_C, \phi) + F_2(\alpha R, \theta_C, \phi) + 2c \cdot \Re\left[F_3(\alpha R, \theta_C, \phi)\right]\} \end{aligned} \tag{A.17}$$

$$\begin{aligned} S_{\overline{RV}}(\omega) = \ & \tfrac{4}{9R^2} \int_0^\infty d\alpha \int_0^{2\pi} \alpha d\phi \ S_u(\alpha, \phi, \omega) \\ & \cdot \{F_1(\alpha R, \theta_C, \phi) + c^2 \cdot F_2(\alpha R, \theta_C, \phi) - 2c \cdot \Re\left[F_3(\alpha R, \theta_C, \phi)\right]\}\,. \end{aligned} \tag{A.18}$$

Here, $\Re[\ ]$ denotes the real component. Wavenumber-frequency spectra of horizontal divergence, and relative vorticity fields are related to the velocity spectrum by

$$S_{HD}(\alpha, \phi, \omega) = \alpha^2 (cos\phi + c \cdot sin\phi)^2 \cdot S_u(\alpha, \phi, \omega) \tag{A.19}$$

$$S_{RV}(\alpha, \phi, \omega) = \alpha^2 (c \cdot cos\phi - sin\phi)^2 \cdot S_u(\alpha, \phi, \omega). \tag{A.20}$$

Note that $S_{HD}(\alpha, \phi, \omega)$ and $S_{RV}(\alpha, \phi, \omega)$ are linearly related for any given wave vector.

To simplify our discussion, we consider a zonal flow field ($c = 0$) without meridional dependence, with nonvanishing horizontal divergence and zero relative vorticity. For this flow field, frequency spectral estimates of $\overline{HD}$ and $\overline{RV}$ can be expressed as

$$S_{\overline{HD}}(\omega) = \int_0^\infty d\alpha \left\{ S_{HD}(\alpha, \omega) F'(\alpha R, \theta_C) \right\} \tag{A.21}$$

$$S_{\overline{RV}}(\omega) = \int_0^\infty d\alpha \left\{ S_{HD}(\alpha, \omega) G'(\alpha R, \theta_C) \right\} \tag{A.22}$$

$$F'(\alpha R, \theta_C) = \left\{ \frac{4}{9\alpha^2 R^2} F_2(\alpha R, \theta_C, \phi = 0) \right\} \tag{A.23}$$

$$G'(\alpha R, \theta_C) = \left\{ \frac{4}{9\alpha^2 R^2} F_1(\alpha R, \theta_C, \phi = 0) \right\}. \tag{A.24}$$

Here, $F'(\alpha R, \theta_C)$ is the attenuation array response function which describes the effect due to the finite separation among current meters and $G'(\alpha R, \theta_C)$ is the contamination array response function that describes the contamination resulting from the presence of HD. Although the flow field does not contain relative vorticity, the estimated spectrum of $\overline{RV}$ does not vanish due to the contamination from the HD field. Both F' and G' depend on the radius of the circle, the wavenumber magnitude ($\alpha = | k_x |$), and the orientation of the mooring relative to the wavenumber. These two array response functions are displayed in Figure 43 as functions of αR with the orientation of mooring ranging from $\theta_C = 0$ to $\theta_C = \frac{\pi}{3}$. F' is largest at $\theta_C = 0$. It decreases with increasing θ_C reaching its smallest at $\theta_C = \pi/6$, and increases again until $\theta_C = \pi/3$ where it reaches its largest value. The contamination array response function G' vanishes at $\theta_C = 0$ and increases with θ_C until $\theta_C = 6/\pi$ where it reaches a peak. For higher θ_C, G' decreases again and vanishes at $\theta_C = 3/\pi$. Accordingly, there is no contamination error in the spectral estimate of $\overline{RV}$ if the mooring array is set up for $\theta_C = \frac{n\pi}{3}$ with any integer n. In this case, current meters C and A are aligned on the y–direction. Therefore, the estimate of the relative vorticity vanishes.

A.3 Simulations of Unidirectional Flow Past a Triad of Current Meters

Simulations of flow past a triad of current meters have been discussed by Prater (1989). A velocity time series is generated using a first order autoregressive model, AR(1), i.e.,

$$u(t) = a \cdot u(t - \Delta t) + \varepsilon(t), \tag{A.25}$$

where Δt is the time interval of 60 s, and the coefficient a of the autoregressive model is chosen to be 0.999. ε is a Gaussian distributed random variable with a variance of 0.0469 $\mathrm{cm}^2/\mathrm{s}^2$. These parameters are chosen to duplicate the velocity frequency spectrum observed from IWEX measurements.

The simulated time series of zonal velocity is advected past a triad of current meters by a zonal mean current U_0 at about 0.1 cm/s. Frequency spectra of $\overline{HD}$ and $\overline{RV}$ can be obtained replacing $S_{\overline{HD}}(\alpha,\omega)$ in eqs. A.21 and A.22 with $k_x^2 S_u(\omega)\ \delta(\omega - U_0 k_x)$. They are displayed in Figures 44 and 45 for radii of circles connecting three current meters in the configuration of IWEX (4.9 m, 25.4 m, 80.3 m, 260 m, and 925 m). Frequency spectra of $\overline{HD}$ and $\overline{RV}$ are very similar except in the low frequency band of the smallest two separations where $S_{\overline{HD}}(\omega)$ is greater than $S_{\overline{RV}}(\omega)$.

In this simulation scheme, for each frequency the wavenumber–frequency velocity

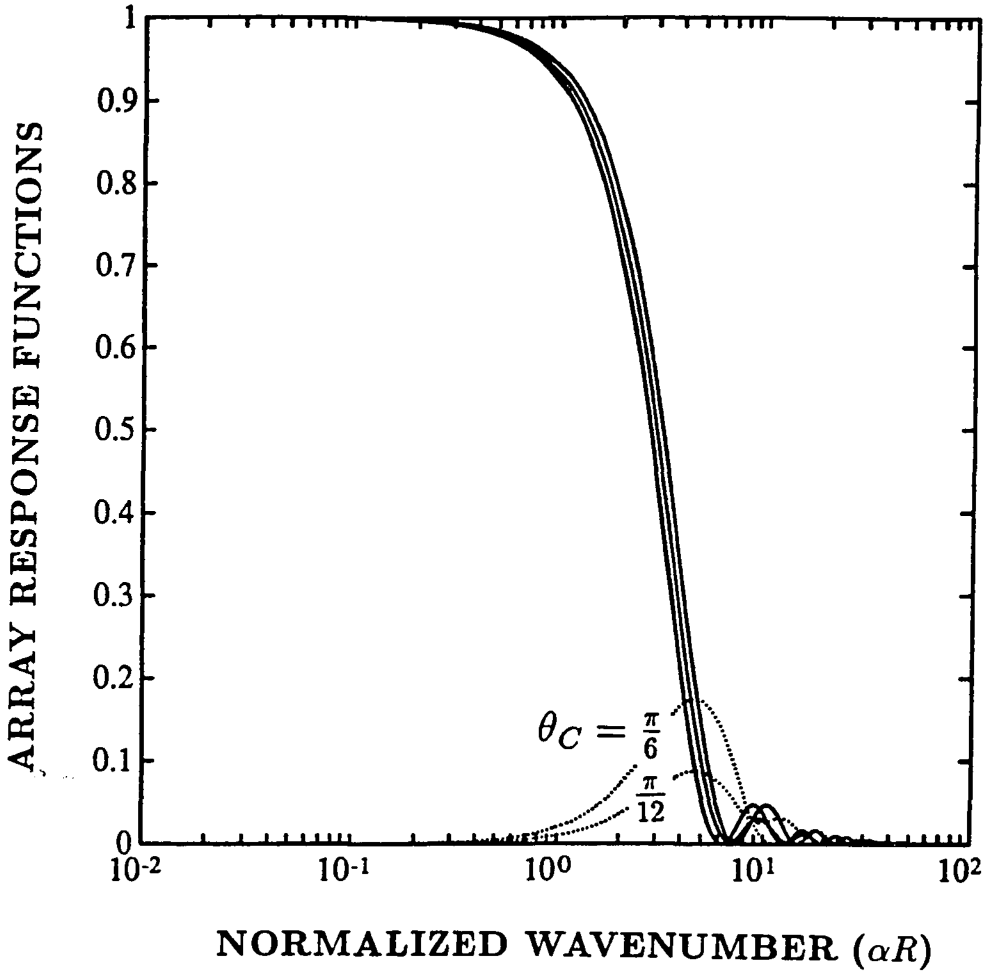

Figure 43: Array response functions applied to frequency spectra of $\overline{HD}$ and $\overline{RV}$ assuming a meridionally independent zonal velocity field. The flow field contains the horizontal divergence, but not the relative vorticity. The solid and dotted lines are the attenuation and contamination array response functions for different orientations of the mooring array.

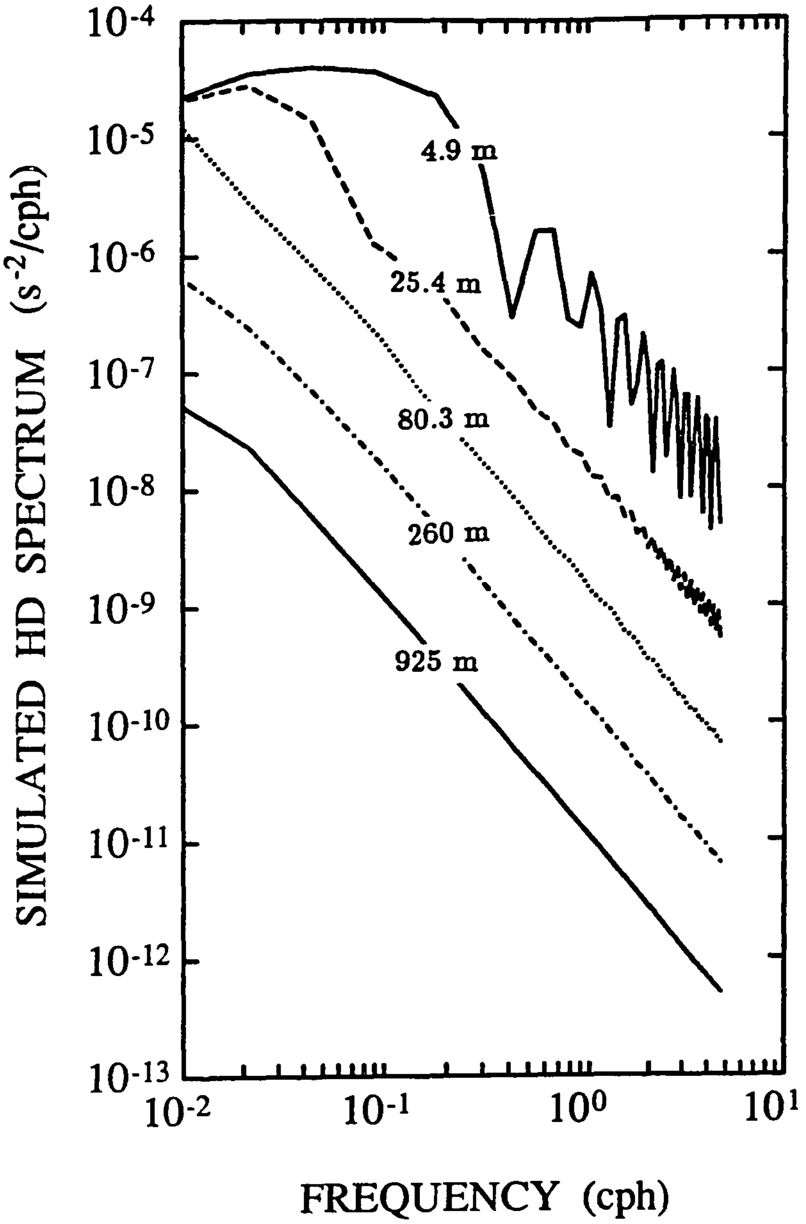

Figure 44: Estimated frequency spectra of $\overline{HD}$ assuming a mean advection velocity of 0.1 cm s^{-1} passing triads of current meters with the orientation $\theta_C = \pi/6$ and radii of 4.9 m, 25.4 m, 80.3 m, 260 m, and 925 m as in IWEX.

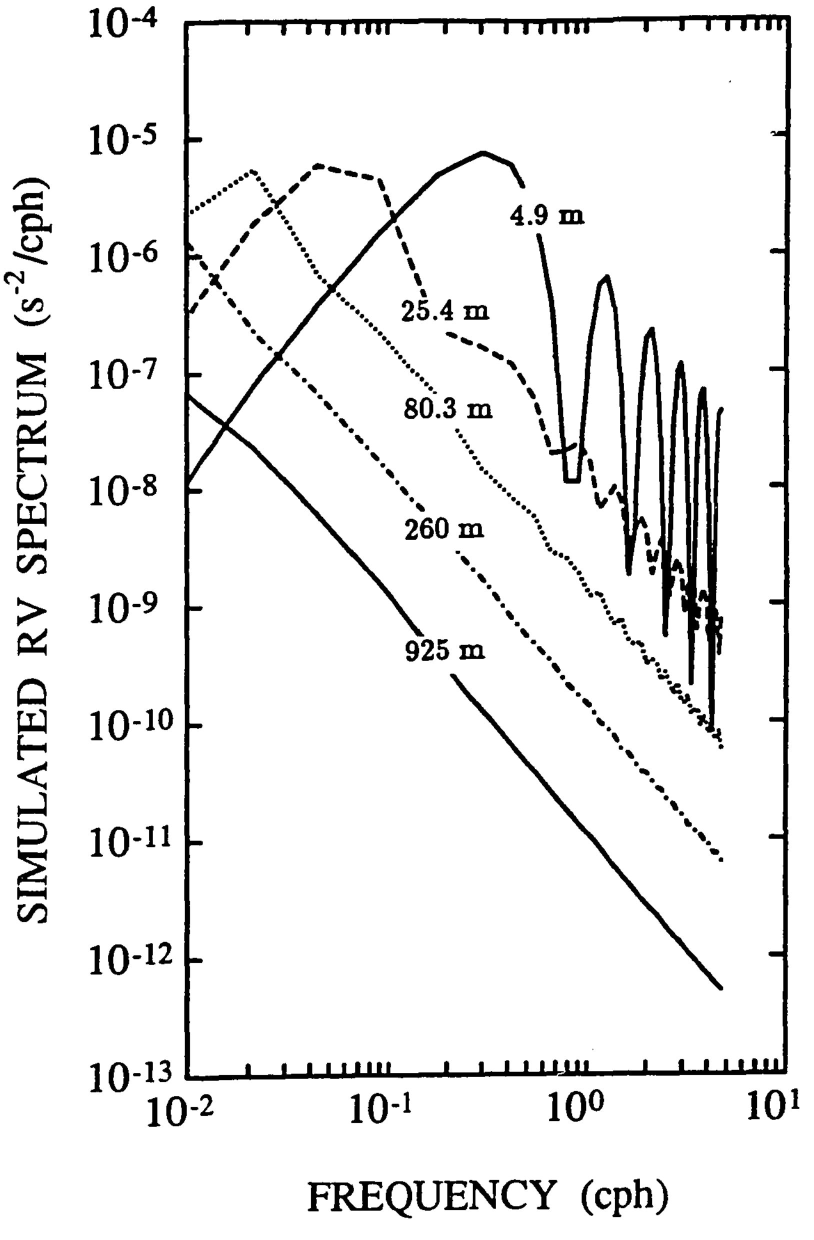

Figure 45: Same as Figure 44 for estimated frequency spectra of $\overline{RV}$.

spectrum exists at one specific wavenumber only, i.e., $\alpha = k_x = \frac{\omega}{U_0}$. Given $U_0 = 0.1$ cm/s, the horizontal wavenumber increases from 0.0677 m^{-1} at the inertial frequency f (= 0.03878 cph) to 4.5 m^{-1} at the buoyancy frequency N ($\approx$ 2.6 cph). The attenuation and contamination array response functions for different radii of the circle connecting three current meters are presented in Figure 46. The wavenumber band corresponding to the internal frequency range is also shown. Clearly, these two array response functions are of the same order for radii of 80.3 m and 925 m in this wavenumber band. However, for the 4.9 m radius, the attenuation array response function is greater than that of the contamination array response function in the low wavenumber region (low frequency) of the band and they are of the same order beyond the wavenumber of 0.5 m^{-1} (corresponding to the frequency about 0.3 cph). $S_{\overline{HD}}(\omega)$ and $S_{\overline{RV}}(\omega)$ are of the same order beyond the frequency of 0.3 cph for the 4.9 m radius. This explains the similarity between simulated frequency spectra of $\overline{HD}$ and $\overline{RV}$ for larger separations and the detected rolling off frequencies at smaller separations. This example clearly demonstrates the concept of array response functions applied to frequency spectral estimates of $\overline{HD}$ and $\overline{RV}$.

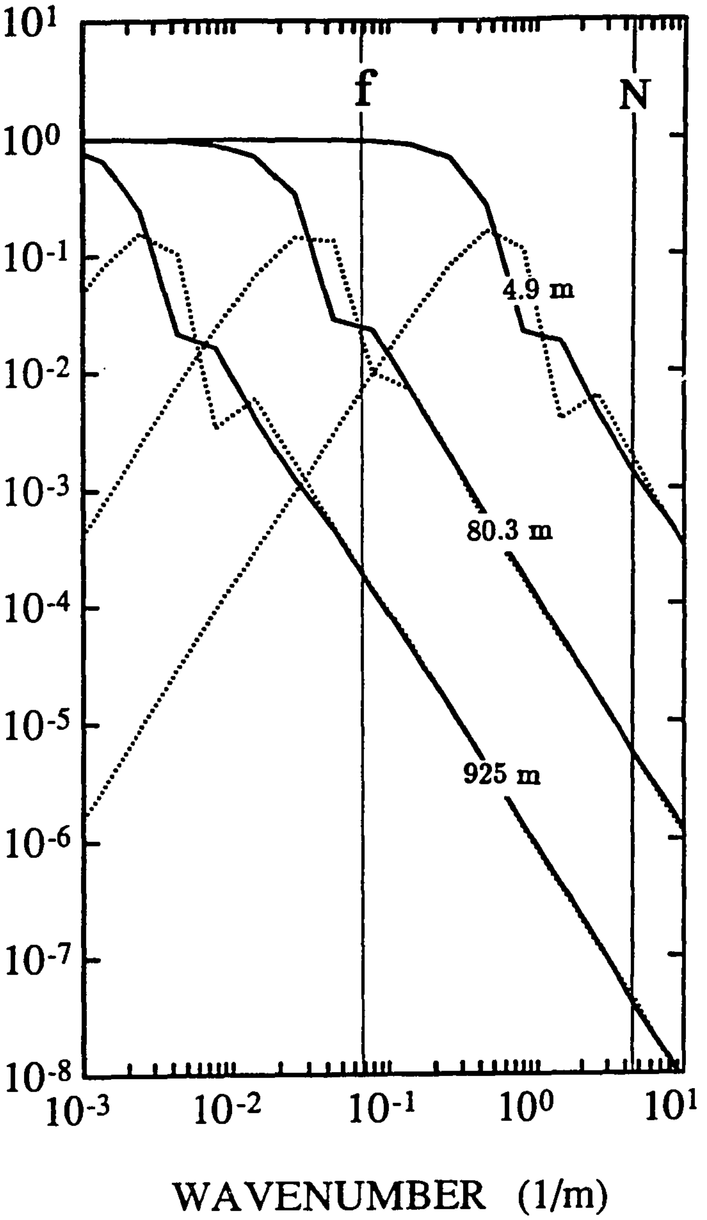

Figure 46: Array response functions for radii of 4.9 m, 80.3 m, and 925 m. Thick solid lines and dotted lines represent the attenuation and contamination array response functions. Two thin solid lines show the wavenumber band corresponding to the internal wave frequency range.

Appendix B

General Representation of Array Response Functions

Here, we will derive array response functions for frequency spectral estimates of $\overline{HD}$ and $\overline{RV}$ assuming arbitrary number of current sensors spaced evenly on a circle at a horizontal plane. It is intended to improve experimental design for the estimation of area–averaged HD and RV.

Using the isotropic condition for velocity spectra (Batchelor, 1953), velocity frequency cross-spectra at a given horizontal space lag $\underline{r}$ can be expressed as

$$\begin{aligned} P_{uu}(\omega; r, \theta) = & \int_0^\infty d\alpha \left\{ [J_0(\alpha r) - cos(2\theta) J_2(\alpha r)] \frac{S_{HD}(\alpha, \omega)}{2\alpha^2} \right. \\ & \left. + [J_0(\alpha r) + cos(2\theta) J_2(\alpha r)] \frac{S_{RV}(\alpha, \omega)}{2\alpha^2} \right\} \end{aligned} \tag{B.1}$$

$$\begin{aligned} P_{vv}(\omega; r, \theta) = & \int_0^\infty d\alpha \left\{ [J_0(\alpha r) + cos(2\theta) J_2(\alpha r)] \frac{S_{HD}(\alpha, \omega)}{2\alpha^2} \right. \\ & \left. + [J_0(\alpha r) - cos(2\theta) J_2(\alpha r)] \frac{S_{RV}(\alpha, \omega)}{2\alpha^2} \right\} \end{aligned} \tag{B.2}$$

$$P_{uv}(\omega;r,\theta) = P_{vu}(\omega;r,\theta) = -\int_0^{\infty} d\alpha J_2(\alpha r) sin(2\theta) \frac{S_{HD}(\alpha,\omega) - S_{RV}(\alpha,\omega)}{2\alpha^2}. \quad \text{(B.3)}$$

Here, r is the horizontal separation distance between two current sensors and θ is their angle counterclockwise from the east. $P_{uu}(\omega;r,\theta)$, $P_{vv}(\omega;r,\theta)$ and $P_{uv}(\omega;r,\theta)$ are velocity frequency cross-spectra with a space lag $\underline{r}$.

Assuming there are N current meters located evenly on a horizontal circle, area averaged horizontal divergence $\overline{HD}$ and relative vorticity $\overline{RV}$ can be estimated using the Stokes' and Gauss' theorems. In the following, the estimation of $\overline{HD}$ will be illustrated and the estimation of $\overline{RV}$ is essentially the same. $\overline{HD}$ is estimated as the approximate circle integration of the radial velocity components at all current sensors as

$$\overline{HD} = \frac{1}{\pi R^2} \sum_{n=1}^{\mathrm{N}} u_r^{(n)} \frac{2\pi R}{N}, \quad \text{(B.4)}$$

where R is the radius of the circle where current measurements are sampled, and $u_r^{(n)}$ is the radial velocity component of the n^{th} measurements. The radial velocity component is estimated as

$$u_r^{(n)} = u_r(R,\theta_n) = u(R,\theta_n)cos(\theta_n) + v(R,\theta_n)sin(\theta_n) \quad \text{(B.5)}$$

$$\theta_n = \theta_0 + \frac{2n\pi}{N}. \quad \text{(B.6)}$$

Here, θ_0 is the angle of a reference current sensor. θ_n is the differential angle counterclockwise from the reference current sensor.

Accordingly, estimates of $\overline{HD}$ can be expressed in terms of Fourier transforms of velocity measurements at each instant of time

$$\overline{HD} = \frac{2}{NR}\sum_{n=1}^{N}\int_0^{\infty} d^2\underline{k}\left[u(\underline{k})e^{i\underline{k}\cdot\underline{R}_n}cos(\theta_n) + v(\underline{k})e^{i\underline{k}\cdot\underline{R}_n}sin(\theta_n)\right]. \qquad \text{(B.7)}$$

Assuming statistically homogeneous and stationary conditions, frequency spectral estimates $S_{\overline{HD}}(\omega;R,N)$ derived from N current sensors on a circle of the radius of R can be expressed as

$$\begin{aligned} S_{\overline{HD}}(\omega;R,N) = \; & \frac{4}{N^2R^2}\sum_{n=1}^{N}\sum_{n'=1}^{N}\int_0^{\infty} d\underline{k}^2\,\{P_{uu}(\underline{k},\omega)cos(\theta_n)cos(\theta_{n'}) \\ & + P_{vv}(\underline{k},\omega)sin(\theta_n)sin(\theta_{n'}) \\ & + P_{uv}(\underline{k},\omega)cos(\theta_n)sin(\theta_{n'}) \\ & + P_{vu}(\underline{k},\omega)sin(\theta_n)cos(\theta_{n'})\}\, e^{i\underline{k}\cdot(\underline{R}_n-\underline{R}_{n'})}. \end{aligned} \qquad \text{(B.8)}$$

Using representations of velocity cross spectra of an isotropic flow field in eqs. B.1, B.2, and B.3, $S_{\overline{HD}}(\omega;R,N)$ can be expressed in terms of wavenumber–frequency spectra $S_{HD}(\alpha,\omega)$ and $S_{RV}(\alpha,\omega)$ as

$$S_{\overline{HD}}(\omega;R,N) = \int_0^{\infty} d\alpha\,\{S_{HD}(\alpha,\omega)F(\alpha R,N) + S_{RV}(\alpha,\omega)G(\alpha R,N)\} \qquad \text{(B.9)}$$

$$\begin{aligned} F(\alpha R,N) = \; & \frac{2}{N^2\alpha^2R^2}\sum_{n=1}^{N}\sum_{n'=1}^{N} \\ & \left[cos(\theta_n-\theta_{n'})J_0(2\alpha R sin(\frac{\theta_n-\theta_{n'}}{2})) + J_2\left(2\alpha R sin(\frac{\theta_n-\theta_{n'}}{2})\right)\right] \end{aligned} \qquad \text{(B.10)}$$

$$G(\alpha R,N) = \frac{2}{N^2\alpha^2R^2}\sum_{n=1}^{N}\sum_{n'=1}^{N}$$

$$\left[cos(\theta_n - \theta_{n'})J_0(2\alpha Rsin(\frac{\theta_n - \theta_{n'}}{2})) - J_2\left(2\alpha Rsin(\frac{\theta_n - \theta_{n'}}{2})\right)\right]. \tag{2.11}$$

$F(\alpha R, N)$ and $G(\alpha R, N)$ are the attenuation and contamination array response functions. These two functions for six and nine current sensors on the circle are displayed in Figures 47 and 48. The attenuation array response function does not change significantly with the increasing number of the current sensors since it is only sensitive to the size of the circle. However, the amplitude of the contamination array response function reduces by a factor of five with the increasing number of current sensors and the center of the band moves to higher wavenumber. Therefore, the contamination error can be reduced simply by increasing the number of current sensors on the horizontal circle. In the case of IWEX, the total number of instruments equals three and the above relation reduces to what we have derived in the Appendix A.

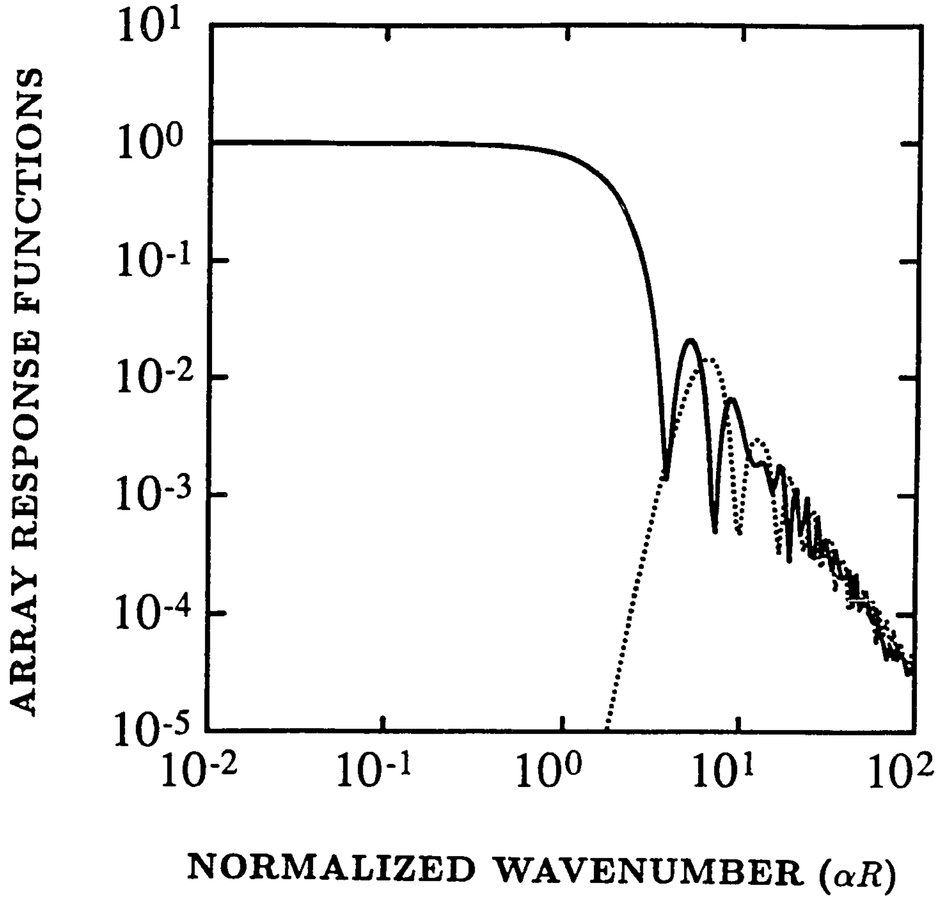

Figure 47: Array response functions for frequency spectral estimates of $\overline{HD}$. $\overline{HD}$ is estimated from six current measurements located evenly on a horizontal circle. The solid and dotted lines show the attenuation and contamination array response functions.

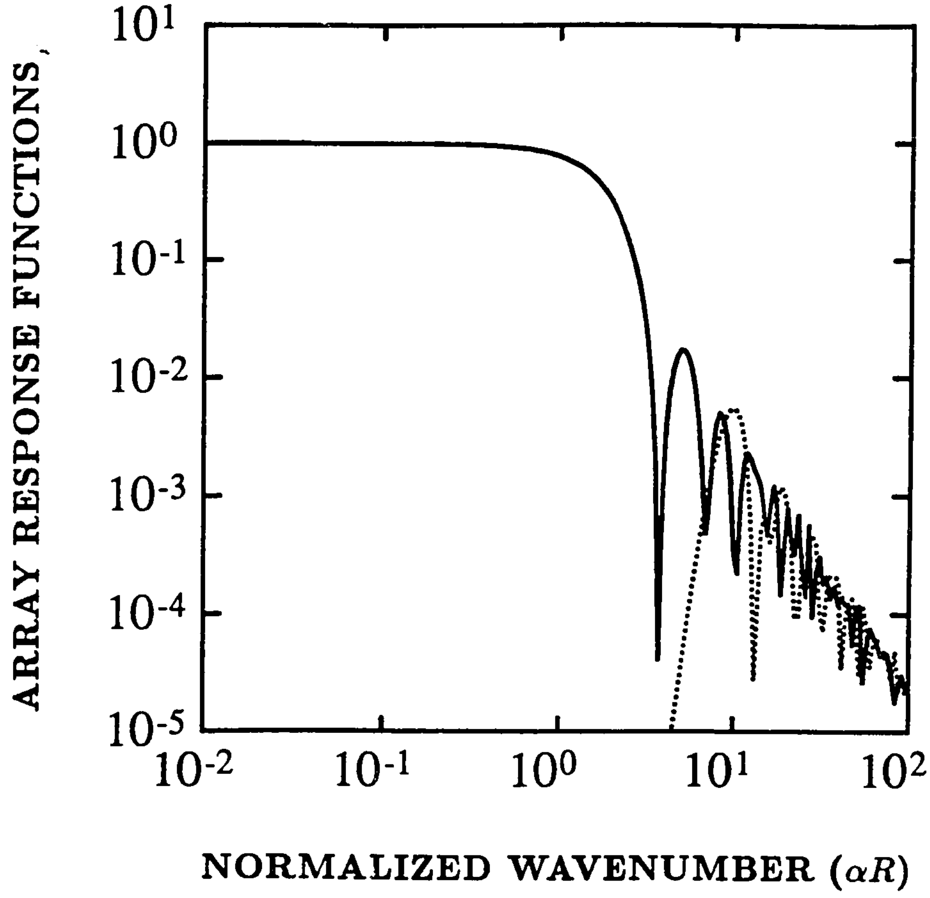

Figure 48: Array response functions for frequency spectral estimates of $\overline{HD}$. $\overline{HD}$ is estimated from nine current measurements located evenly on a horizontal circle. The solid and dotted lines show the attenuation and contamination array response functions.

Appendix C

GM–76 Spectrum

The Garrett and Munk (1972, 1975) internal wave model spectra have been changed and improved during the course of time. The version that is used in this paper is generally referred to as the GM–76 spectrum (Cairns and Williams, 1976). For this spectrum the distribution of total internal wave energy in frequency–horizontal wavenumber space is given by

$$E(\omega, \alpha) = b^2 N N_0 E_0 B(\omega) \frac{A(\alpha/\alpha_*)}{\alpha_*}, \tag{C.1}$$

with

$$B(\omega) = \frac{2}{\pi} \frac{f}{\omega} (\omega^2 - f^2)^{-1/2} \tag{C.2}$$

$$A(\lambda) = \frac{2}{\pi} (1 + \lambda^2)^{-1} \tag{C.3}$$

$$\alpha_*(\omega) = (\omega^2 - f^2)^{1/2} N^{-1} \beta_* \tag{C.4}$$

$$\beta_* = \frac{\pi}{b} \frac{N}{N_0} j_*. \tag{C.5}$$

The parameters are chosen to be $b = 1.3 \times 10^3$ m, $N_0 = 5.2 \times 10^{-3}$ s^{-1}, $E_0 = 6 \times 10^{-5}$ and $j_* = 3$. The spectrum also includes a high wavenumber cutoff

$$\alpha_c(\omega) = (\omega^2 - f^2)^{1/2}(N^2 - \omega^2)^{-1/2}\beta_c, \tag{C.6}$$

with $\beta_c = 2\pi/10$ m^{-1} = 0.1 cpm.

References

Batchelor, G. K., 1953: The theory of homogeneous turbulence, Cambridge University Press, 197 pp.

Bendat, J. S., and A. G. Piersol, 1971: Random data: Analysis and measurement procedures, Wiley, New York, 407 pp.

Briscoe, M. G., 1975: Preliminary results from the trimoored internal wave experiment (IWEX), *J. Geophys. Res.*, 80, 27, 3872–3884.

Cahn, A., 1945: An investigation for the free oscillations of a simple current system, *J. Meteor.,* 2, 113–119.

Cairns, J. L., and G. D. Williams, 1976: Internal wave observations from a midwater float, Part II, *J. Geophys. Res.,* 81, 1943–1950.

Gage, K. S., 1979: Evidence for a $k^{-5/3}$ law inertial range in mesoscale two–dimensional turbulence, *J. Atmos. Sci.*, 36, 1950–1954.

Gargett, A. E., P. J. Hendricks, T. B. Sanford, T. R. Osborn, and A. J. Williams, III, 1981: A composite spectrum of vertical shear in the upper ocean, *J. Phys. Oceanogr.,* 11, 1258–1271.

Garrett, C. J. R., and W. H. Munk, 1972: Space-time scales of internal waves: A progress report, *Geophys. Fluid Dyn.*, 2, 225–264.

Garrett, C. J. R., and W. H. Munk, 1975: Space-time scales of internal waves: A progress report, *J. Geophys. Res.*, 80, 291–297.

Gill, A. E., 1976: Adjustment under gravity in a rotating channel, *J. Fluid Mech.,* 77, 603–621.

Gill, A. E., 1982: Atmosphere–Ocean Dynamics, International Geophysics Series, Academic Press, New York, 662 pp.

Gradshteyn, I. S., and I. M. Ryzhik, 1965: Table of integrals, series, and products, Academic Press, New York and London.

Gregg, M. C., 1977: A comparison of finestructure spectra from the main thermocline, *J. Phys. Oceanogr.,* 7, 33–40.

Hasselmann, K., 1970: Wave–driven inertial oscillation, *Geophys. Fluid Dyn.*, 1, 463–502.

Lilly, D. K., 1983: Stratified turbulence and the mesoscale variability of the atmosphere, *J. Atmos. Sci.,* 40, 749–761.

Lin, J. T., and Y. H. Pao, 1979: Wakes in stratified fluids, *Ann. Rev. of Fluid Mech.,* 11, 317–338.

Middleton, J. F., 1987: Energetics of linear geostrophic adjustment, *J. Phys. Oceanogr.*, 17, 735–740.

McWilliams, J. C., 1985: Submesoscale, coherent vortices in the ocean, *Rev. of Geophys.*. 23, 165–182.

Müller, P., D. J. Olbers, and J. Willebrand, 1978: The IWEX spectrum, *J. Geophys. Res.*, 83, 479–500.

Müller, P., 1984: Small scale vortical motions. Internal Gravity Waves and Small-Scale Turbulence, *Proc., 'Aha Huliko'a Hawaiian Winter Workshop*, Hawaii Institute of Geophys., Spec. Pub., P. Müller and R. Pujalet, Eds.

Müller, P., R. C. Lien, and R. Williams, 1988: Estimates of potential vorticity at small scales in the ocean, *J. Phys. Oceanogr.*, 18, 401–416.

Munk, W. H., 1981: Internal waves and small scale processes, Evolution of Physical Oceanography, B. A. Warren, and C. Wunsch, Eds., The MIT Press, 264–291.

Olbers, D. J., 1990: Internal gravity waves, To appear in Landolt/Bornstein, V/13 Oceanography.

Prater, M. D., 1989: Simulations of flow past a triad of current meters, Unpublished manuscript.

Riley, J. J., R. W. Metcalfe, and M. A. Weissman, 1981: Direct numerical simulations of homogeneous turbulence in density–stratified fluids, In: B. J. West (Editor), Nonlinear Properties of internal Waves, *Amer. Institute of Phys.*, 76, 79–112.

Rossby, C.-G., 1937: On the mutual adjustment of pressure and velocity distributions in certain simple current systems, I, *J. Mar. Res.,* 1, 15–18.

Rossby, C.-G., 1938: On the mutual adjustment of pressure and velocity distributions in certain simple current systems, II, *J. Mar. Res.,* 1, 239–263.

Sherman J., and R. Pinkel, 1990: Estimates of the vertical wavenumber–frequency spectra of vertical shear and strain, *J. Phys. Oceanogr.* (in press).

Staquet, C., and J. J. Riley, 1989a: On the velocity field associated with potential vorticity, *Dyn. Atmos. Oceans*, 14, 93–123.

Staquet, C., and J. J. Riley, 1989b: A numerical study of a stable–stratified mixing layer, *Turbulent Shear Flows*, 6, Springer–Verlag, 381–397.

Tarbell, S. M., M. G. Briscoe, and D. Chausse, 1976: A compilation of moored current data and associated oceanographic observations, 1973 Internal Wave Experiment (IWEX), Tech. Rep., 75–68, Vol. IX, Woods Hole Oceanogr. Inst., Woods Hole, Mass.

Van Zandt, T. E., 1982: A universal spectrum of buoyancy waves in the atmosphere, *Geophys. Res. Lett.*, 9, 575–578.